HZDR-079

Wissenschaftlich-Technische Berichte
HZDR-079 2017 · ISSN 2191-8708

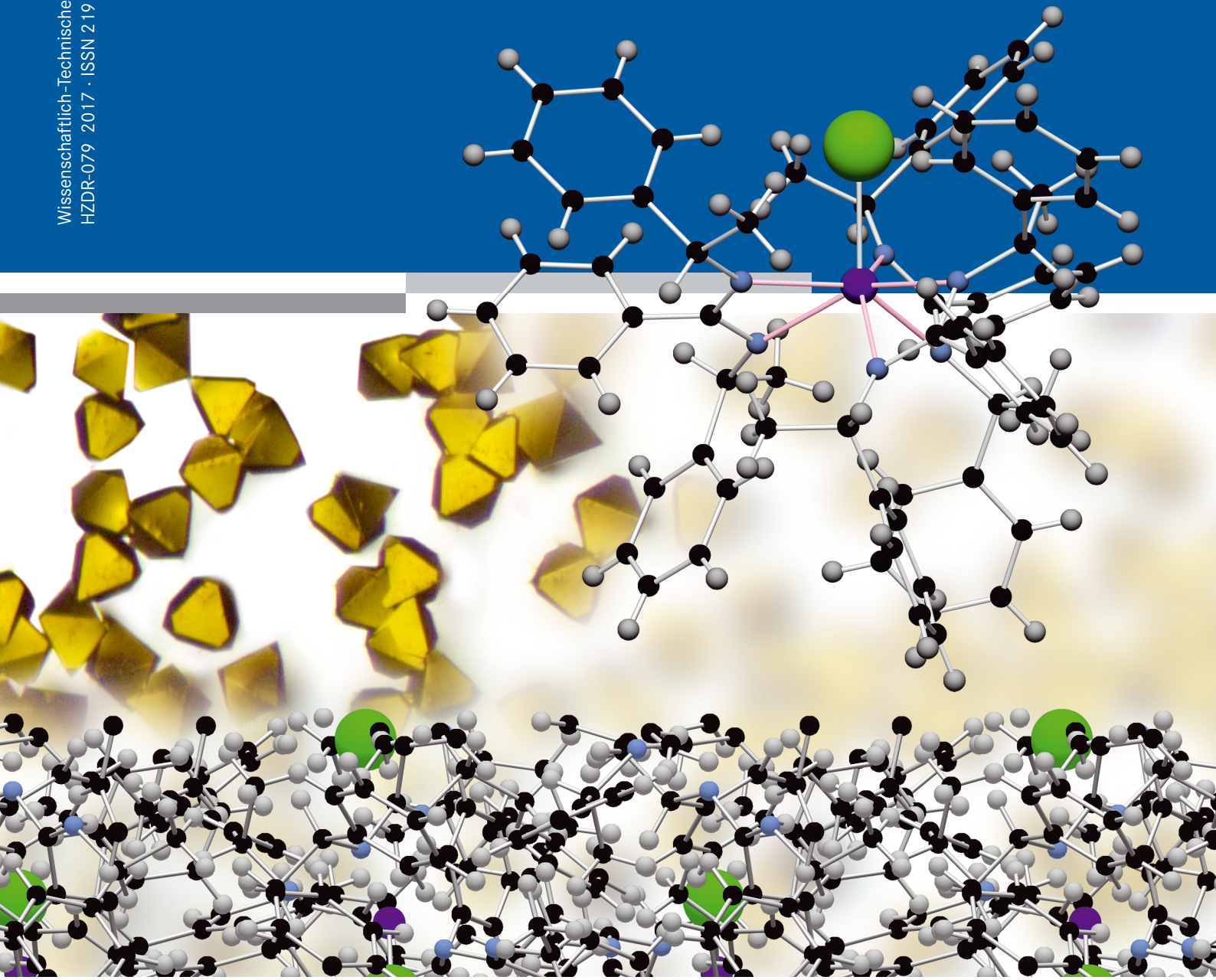

ANNUAL REPORT 2016

INSTITUTE OF RESOURCE ECOLOGY

HZDR

HELMHOLTZ
ZENTRUM DRESDEN
ROSSENDORF

Wissenschaftlich-Technische Berichte
HZDR-079

Annual Report 2016

Institute of Resource Ecology

HZDR
HELMHOLTZ ZENTRUM DRESDEN ROSSENDORF

Impressum

Print edition: ISSN 2191-8708
Electronic edition: ISSN 2191-8716

https://www.hzdr.de/publications/Publ-25236
urn:nbn:de:bsz:d120-qucosa-219706

Published by Helmholtz-Zentrum Dresden–Rossendorf e.V.

Contact

Helmholtz-Zentrum Dresden–Rossendorf e.V.
Institute of Resource Ecology

Postal Address	*Address for visitors*
P.O. Box 51 01 19 D-01314 Dresden Germany	Bautzner Landstraße 400 D-01328 Dresden Germany

Phone: +49 (0) 351 260 3210
Fax: +49 (0) 351 260 3553
e-mail: contact.resourceecology@hzdr.de
http://www.hzdr.de/fwo

This report is also available at http://www.hzdr.de/fwo

Cover picture

Molecular structure of a chiral benzamidine complex of tetravalent uranium (structure image at the upper right) and their crystal structure (structure at the bottom). Detailed information can be found in the relevant contribution by S. Schöne, *et al.* (→ pp. 18). An optical micrograph of single crystals of typical metal-organic complex of uranium is shown in the background.

(Graphical material provided by A. Ikeda-Ohno)

Preface

The Institute of Resource Ecology (IRE) is one of the eight institutes of the Helmholtz-Zentrum Dresden – Rossendorf (HZDR). The research activities are mainly integrated into the program "Nuclear Waste Management, Safety and Radiation Research (NUSAFE)" of the Helmholtz Association (HGF) and focused on the topics "Safety of Nuclear Waste Disposal" and "Safety Research for Nuclear Reactors".

Additionally, various activities have been started investigating chemical and environmental aspects of processing and recycling of strategic metals, namely rare earth elements. These activities are located in the HGF program "Energy Efficiency, Materials and Resources (EMR)". Both programs, and therefore all work which is done at IRE, belong to the research sector "Energy" of the HGF.

The research objectives are the protection of humans and the environment from hazards caused by pollutants resulting from technical processes that produce energy and raw materials. Treating technology and ecology as a unity is the major scientific challenge in assuring the safety of technical processes and gaining their public acceptance. We investigate the ecological risks exerted by radioactive and non-radioactive metals in the context of nuclear waste disposal, the production of energy in nuclear power plants and in processes along the value chain of metalliferous raw materials. A common goal is to generate better understanding about the dominating processes essential for metal mobilization and immobilization on the molecular level by using advanced spectroscopic methods. This in turn enables us to assess the macroscopic phenomena, including models, codes and data for predictive calculations, which determine the transport and distribution of contaminants in the environment.

The extraordinary broadness of research topics and activities is illustrated below by some selected highlights:

In 2016, the upgrade program for the Rossendorf Beamline at the ESRF in Grenoble successfully started with high-resolution XANES and emission spectroscopy experiments on a prototype single crystal spectrometer (→ pp. 27 & 30). This upgrade will proceed for another 4 years until 2020, when a 5-crystal spectrometer, a 2D detector, and a new 6-circle diffractometer will be available in a new hutch fully equipped and licensed as alpha laboratory. The experimental capabilities of the beamline will then include high-resolution X-ray absorption and emission spectroscopy, resonant inelastic x-ray scattering in addition to EXAFS, and a variety of surface, powder and single crystal diffraction techniques (CTR, RAXR).

A new method accounting for spectral history effects was developed and implemented in the in-house reactor dynamics code DYN3D. Detailed nuclide content can be calculated for each region of the reactor core and used in combination with a spectral index correction to determine the actual fuel properties. The new method demonstrates excellent results in various depletion scenarios and for different fuel types (uranium, mixed oxide, thorium). For the first time, DYN3D can correctly account for outage times of the reactor.

In 2016, with the reconstruction of major parts of the controlled area of the research site Leipzig still ongoing, the production of short lived radionuclides and their subsequent use in tracer studies was continued. Particularly, the results of the uptake of radiolabeled [^{139}Ce]CeO_2 nano particles into plants (→ p. 56), as detected by autoradiography of sunflower leafs, are to be emphasized.

Rock salt is still in discussion to be used as a potential host rock for a nuclear waste repository. *Hbt. noricense* DSM 15987 can be seen as a reference strain for halophilic microorganisms in rock salt due to its worldwide occurrence. By a combination of microscopic (SEM) and spectroscopic (EXAFS and TRLFS) methods it was shown for the first time that Haloarchaea are able to form uranium phosphate minerals with a very low solubility (→ p. 51).

Molecular mechanisms of metal transport across biological membranes underlay the transit of heavy metals from the geo- to the biosphere. We have designed nanoparticles of a bacterial heavy metal transporter within a nanosized membrane. Such particles hold not only great promise for their planned use in XFEL-based structure determination. They also allowed measuring for the first time the dipole strength and mobility at a metal-binding site in the interior of a membrane protein (→ p. 43). The data reveal details of the entry mechanism of ions with extended hydration shells, such as heavy metals and actinides, into membrane proteins and eventually into the cell.

Since the commencement of the f-element division in June 2014, the local experimental capability for synthetic chemistry of actinides has been developed steadily. The infrastructure required for the synthesis and characterization of new actinide compounds was completed in 2016, which already resulted in the successful synthesis of several new actinide complexes (→ pp. 17 & 18). Our research activities in the relevant field will accelerate in the next few years.

The surface processes of the ternary sorption system U(VI)/phosphate/SiO_2 were comprehensively investigated by a combined approach applying classical batch sorption experiments, *in situ* optical spectroscopy, and surface complexation modeling. This provided a consistent description of the relevant surface processes by considering a formation of binary U(VI) surface complexes and a precipitate of a U(VI) phosphate. Ternary surface complexes might become significant only in a very low concentration range (< ppm). This study represents a further progress in the fundamental understanding of molecular processes at mineral interfaces and the resultant contributions to techniques applied for safety assessment (→ p. 25).

Beside these highlights, we obtained many more new scientific results in the past year, which are presented in this annual report. This is also documented by 74 original papers published in peer-reviewed international scientific journals. In the year 2016 more than 130 scientists, technicians, and students working on their Ph.D., diploma, master, or bachelor thesis, were employed at the Institute of Resource Ecology. Thereof, 32 Ph.D. students worked at the institute in 2016. Support of young scientists is an important tool to ensure the competence and further scientific excellence in future times. Moreover, the number of female scientists in a

leadership position was enlarged at the Institute of Resource Ecology by assigning three young colleagues as co- division heads. As a result, four out of eight divisions are now managed by female scientists.

Furthermore, the institute had the honor to host the 10th International Biometals Conference in Dresden in July 2016. More than 100 scientists from 22 countries and 5 continents discussed about the coordination chemistry of radionuclides, the metal acquisition and metal transport by microbes as well as their defense strategies.

I would like to thank the visitors, German and international ones, for their interest in our research and for their participation in the institute seminars. We would also like to thank our scientific collaborators and the visiting scientists for coming to Dresden – Rossendorf in 2016 to share their knowledge and experience with us. We will continue to strongly encourage the collaborations and visits by scientists in the future. Special thanks are due to the executive board of the HZDR, the Ministry of Science and Arts of the Free State Saxony (SMWK), the Federal Ministry of Education and Research (BMBF), the Federal Ministry of Economics and Energy (BMWi), the Deutsche Forschungsgemeinschaft (DFG), the European Commission, and other organizations for their support.

Prof. Dr. Thorsten Stumpf
Director of the
Institute of Resource Ecology

Contents

SCIENTIFIC CONTRIBUTIONS

PART I: THE CHEMISTRY OF LONG-LIVED RADIONUCLIDES

PART II: LONG-LIVED RADIONUCLIDES & TRANSPORT PHENOMENA IN GEOLOGICAL SYSTEMS

PART III: LONG-LIVED RADIONUCLIDES IN BIOLOGICAL SYSTEMS

PART IV: NUCLEAR REACTOR SAFETY RESEARCH

PUBLICATIONS

SCIENTIFIC ACTIVITIES

PERSONNEL

ACKNOWLEDGEMENTS

INDEX OF AUTHORS

The Chemistry of

LONG-LIVED RADIONUCLIDES

Structural characterization of Am(III) formate complexes: combining EXAFS spectroscopy with DFT and thermodynamical calculations

A. Rossberg, D. R. Froehlich[1]

[1]Physikalisch-Chemisches Institut, Ruprecht-Karls-Universität Heidelberg, Heidelberg, Germany

We used iterative transformation factor analysis (ITFA) in order to isolate the EXAFS spectral contributions of the complexing ligand from a Am(III)/formate pH-series. Thermodynamic calculations were used as constraint for ITFA and for density functional theory (DFT) calculations to identify the coordination mode within the formed complexes.[1]

Clay host rock formations are considered as potential final repositories for high-level nuclear waste. In long term scenarios, the release of actinides (AN) from their primary containment, due to the intrusion of water and the corrosion of the outer steel barrier, has to be considered. Under reducing conditions the expected oxidation state of Am is +3. Both macromolecular, but also small organic compounds like formate (Form) contained in the pore water of clay formations, can interact with Am(III) by formation of Am(III)–Form complexes, hence influencing the migration of the released AN with impact on risk assessment analysis.

EXPERIMENTAL. Seven aqueous solutions were prepared with Am(III) and Form concentrations of 0.8–1.0×10^{-4} mol/L and 0.8–1.0 mol/L, respectively, while varying the pH between pH 2.16 and 3.94. Am-L_{III} EXAFS spectra were collected with a 13-element Ge detector at room temperature and dead-time correction of the signal was applied. For the 1 : 1 and the 1 : 2 Am(III)-Form complexes the pH-speciation was calculated with stability constants estimated by using the constants given in literature.[2] DFT-calculations were carried out with the LCGTO-FF-DF method for the Am(III)-hydrate and the Am(III)-Form complexes.[3] The structures of 1 : 1 and 1 : 2 Am(III)-Form complexes were calculated assuming different combinations of monodentately (**m**) and bidentately (**b**) coordinated Form ligands, like **m**, **b** and **mm**, **mb**, **bb** for the 1 : 1 and 1 : 2 complexes, respectively. Moreover, for each complex a coordination number (CN) of 8 and 9 was considered, which leads to a total number of 12 complexes to calculate.

RESULTS. ITFA[4] detected two components in the EXAFS spectral mixtures which change their ratio with the pH, indicating that water molecules are successively replaced by Form molecules with increasing pH. By using the pH-speciation the theoretical CN_{Water} and CN_{Form} can be calculated as a function of the pH for different CN combinations of the complexes. For the combination of 9/9/8 (Am(III)-hydrate/1 : 1 complex/1 : 2 complex) the best match between the ITFA-determined and the theoretical CN (Fig. 1) is obtained. The ITFA isolated spectra of one coordinated water and one coordinated Form molecule is shown in Fig. 2 together with the 95 % confidence level of the isolated spectra and the shell fit. The shell fit results in Am–O_{Form} and Am–O_{Water} distances of 2.41 Å and 2.48 Å, respectively. The significantly shorter Am–O_{Form} distance, the presence of C at 3.40 Å and the appearance of a non-coordinated O_{non} at 4.20 Å is in line with a monodentate coordination of Form. Note that each of the scattering contributions are above the noise level as indicated by the green line in Fig. 2. The difference in the Am–O_{Water} and Am–O_{Form} distance (ΔR_{DFT}) can be determined for each of the 24 combinations of the

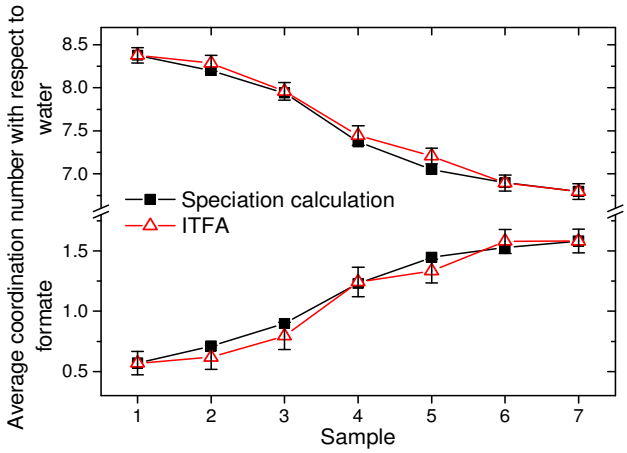

Fig. 1: Comparison of coordination numbers with respect to water and formate for samples 1–7 obtained by ITFA and thermodynamic speciation calculation. ITFA error bars are the confidence intervals at the 95 % confidence level.

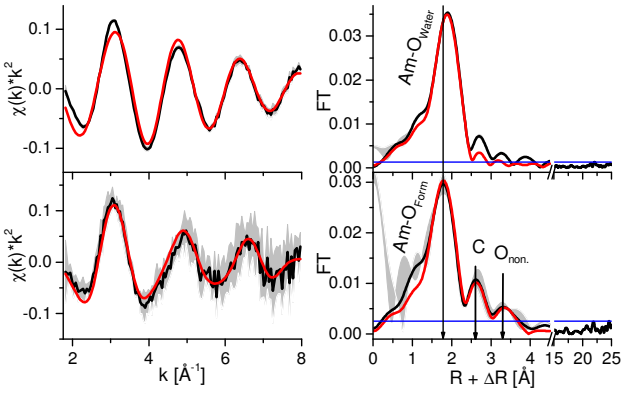

Fig. 2: ITFA isolated (black line) EXAFS contributions (left) and related Fourier Transforms (right) of one coordinated water molecule (top) and one coordinated formate (bottom) with shell fit (red line). Confidence interval at the 95 % confidence level (gray). Arrows point toward positions of prominent peaks. The noise level green) is estimated by using the R-range 15–25 Å.

DFT calculated complexes by using their distribution according to the pH-speciation. If a CN combination of 9/9/8 and **m** and **mm** complexes are assumed, the resulting ΔR_{DFT} of 0.08 Å agrees favorably with the measured ΔR_{EXAFS} of 0.07 Å.

The study shows that the combination of EXAFS with ITFA, thermodynamic calculations and DFT results in a consistent interpretation of the nature of the formed Am(III)-Form complexes for which only monodentate interaction between Am(III) and Form is observed. The pH-speciation of the spectral components is in agreement with the experimentally determined speciation.

[1] Froehlich, D. R. *et al.* (2017) *Inorg. Chem.*, submitted.
[2] Froehlich, D. R. *et al.* (2015) *Appl. Geochem.* **61**, 312–317.
[3] Dunalp, B. I. *et al.* (1990) *Adv. Quantum Chem.* **21**, 317–339.
[4] Rossberg, A. *et al.* (2003) *Anal. Bioanal. Chem.* **376**, 613–638.

Complexation study of a *tert*-butyl-calix[4]arene-based 2-hydroxynaphthalene ligand with uranium(VI) in non-aqueous solution

A. Bauer, K. Schmeide

The actinide uranium, well known from nuclear power cycle, plays also a role in rare earth production as it is an undesired constituent of the respective ores. To facilitate the production of rare earth elements, uranium has to be removed. Due to their modifiable selectivity and solubility calix[n]arenes are interesting compounds for the extraction of actinides and lanthanides.[1] The mechanism of uranium(VI) interaction with a *tert*-butyl-calix[4]arene-based 2-hydroxynaphthalene ligand (L1) was studied by TRLFS, UV-vis spectroscopy and isothermal calorimetry.

EXPERIMENTAL. All experiments were performed in acetonitrile at 25 °C. The ionic strength was kept constant at 0.01 M $NaClO_4$.
Interaction studies were performed by using time-resolved laser-induced fluorescence spectroscopy. 50 µM of uranyl nitrate was titrated by 100 µM L1 solution. The luminescence was excited at 266 nm.
Absorption changes of L1 due to addition of uranyl nitrate were observed in the UV-visible range from 250 to 500 nm. The binding constants were calculated by using HypSpec program (Protonic Software, U.K.).
With respect to thermodynamics the complexation of L1 with uranyl has been investigated using isothermal titration calorimetry (TAM III, TA Instruments, Germany). At certain time intervals, constant volumes of a 5 mM uranyl nitrate solution were added into a cell that contained 100 µM L1 solutions. The change of heat flow was observed as "spike" in a thermogram. OriginPro 2015G (OriginLab, Northampton, U.S.A.) was used for baseline adjustment and peak integration of thermograms. Fitting of the resulting data excluding the first data point was performed with the software CHASM-TA (Bio-Lewis, Mississippi State University, U.S.A.).

RESULTS. Uranyl nitrate dissolved in acetonitrile exhibits emission bands at 467, 486, 507, 529 and 552 nm. The complexation of the uranyl ion by the *tert*-butyl-calix[4]arene-based 2-hydroxynaphthalene ligand led to a decrease of the luminescence signal of uranyl nitrate. The luminescence disappeared already after an addition of 0.6 equivalents of L1. This is a strong indication for complexation.
The UV-vis spectrum of L1 is characterized by absorption bands at 321, 355 and 369 nm (Fig. 1). With increasing uranyl nitrate concentration the peaks decreased up to the addition of one equivalent of uranyl nitrate. Under equimolar conditions, an additional absorption maximum at 437 nm was observed. Factor analysis of the absorption spectra by the HypSpec program indicated the presence of one complex species. The stability constant of the 1 : 1 complex ($\log \beta_{1:1} = 5.93 \pm 0.02$) was found by fitting the data with HypSpec.
Figure 2 shows the thermogram for the complexation of uranyl with L1. It represents the recorded heat flow as a function of time. Negative peaks indicated heat absorption. The binding heats were determined by peak integration. The resulting titration curve (Fig. 3) shows the heats of binding as a function of molar ratio. It affirmed the formation of an 1 : 1 uranyl L1 complex. Consequently, ITC data were fitted into a set of single site binding mode.

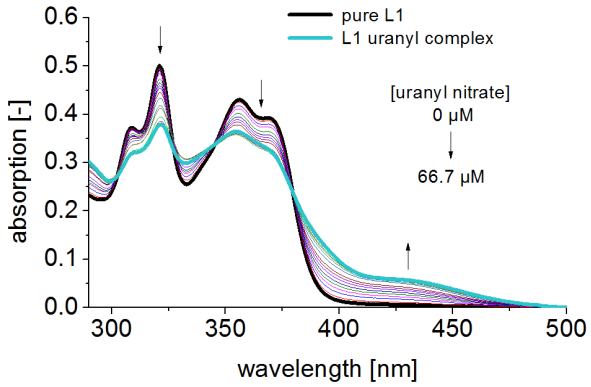

Fig. 1: UV-vis spectra of 16.7 µM L1 in acetonitrile at different uranyl nitrate concentrations; $I = 0.01$ M $NaClO_4$.

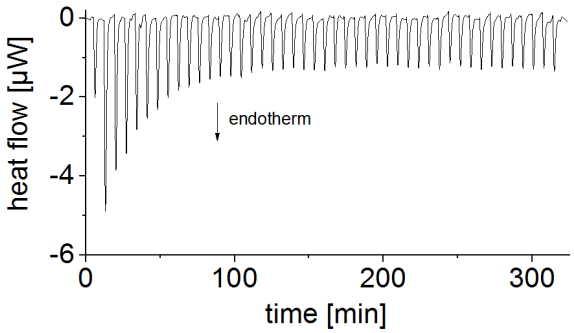

Fig. 2: Isothermal titration calorimetry data obtained for the binding interaction of L1 (100 µM) to uranyl nitrate (5mM) in acetonitrile at 25 °C.

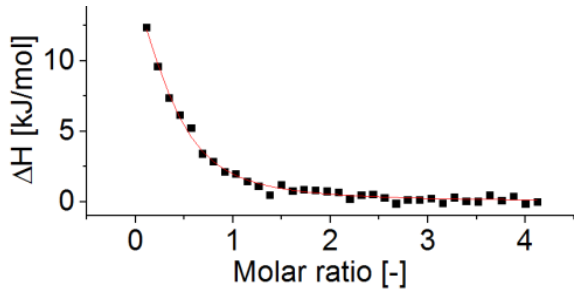

Fig. 3: Integrated heat data obtained for the binding interaction of L1 (100 µM) to uranyl nitrate (5 mM) in acetonitrile at 25°C.

The thermodynamic data ($\Delta H = 22.8 \pm 2.5$ kJ/mol; $T\Delta S = 48.8 \pm 2.7$ kJ/mol) suggested an endothermic and entropy-driven complexation process.[2, 3]

ACKNOWLEDGEMENTS. We thank A. Jäschke and Prof. Dr. B. Kersting for providing the calix[4]arene. The project (SE-FLECX) is funded by Federal Ministry of Education and Research (033R132A).

[1] Glasneck, F. *et al.* (2016) *Eur J Inorg Chem* **2016**, 3111–3122.
[2] Rao, L. F. (2007) *Chem Soc Rev.* **36**, 881–892.
[3] Freire, E. *et al.* (1990) *Anal Chem.* **62**, A950–A959.

Luminescence properties of uranyl-acetate species

H. Brinkmann, H. Moll, T. Stumpf

Time-resolved laser-induced fluorescence spectroscopy (TRLFS) was applied to characterize uranium(VI)-acetate species based on their luminescence properties. In contrast to previous interpretations, no indications were detected for the existence of the 1 : 3 complex.

EXPERIMENTAL. TRLFS experiments were performed in solutions with 50 µM uranyl perchlorate and 0.25 M acetic acid (AcOH; one sample contains no AcOH and is marked with an asterisk) at an ionic strength of 1 M ($NaClO_4$). NaOH and $HClO_4$ were used to adjust the pH of the samples between 1 and 4. The samples were measured at 25 °C and −120 °C. To excite the samples the fourth harmonic (266 nm, ~0.3 mJ) of a pulsed Nd:YAG laser (Continuum) was used and the luminescence was detected in a time dependent manner with an intensified CCD camera (Horiba Jobin Yvon IHR 550).

RESULTS. The static luminescence spectra of the test series are shown in Figs. 1 and 2. The spectra were taken at the same delay time after excitation and were normalized in Fig. 2 to emphasize the spectral changes. The band positions and lifetimes were summarized in Tab. 1.

The band positions and the lifetime of the sample without AcOH can be assigned to the free uranyl-ion and are in accordance with literature values.[1] The addition of AcOH and the increase of the pH, which correlates with the total amount of deprotonated acetate, lead to a quenching of the uranyl-luminescence (Fig. 1, left) and a decrease of the uranyl lifetime. This behavior was extensively discussed in literature and is caused by static and dynamic quenching.[2] Hence, the $UO_2(AcO)^+$ complex showed no luminescence properties. In a second phase (Fig. 1, right), the luminescence intensity increases and the emission bands were shifted to higher wavelengths (Fig. 2, left). A new band occurs at 460 nm. These changes can be assigned to the formation of the $UO_2(AcO)_2$ complex, showing a very short luminescence lifetime of 0.48 µs. To minimize the dynamic quenching the luminescence properties were measured at −120 °C. Below pH 2.2, a constant lifetime of 319 µs and no band shifts were observed for the uranyl-ion at −120 °C (Fig. 2, right) which is in good agreement with literature data.[1] Significant band shifts are only present at pH values above pH 2.4, which can be assigned to the formation of the $UO_2(AcO)_2$ complex with a much longer lifetime of 922 µs compared to those measured at 25 °C.

Under the chosen experimental conditions, the third uranyl-acetate complex $UO_2(AcO)_3^-$ should be formed, according to published stability constants for uranyl-acetate species. But no spectral changes (e.g. band shifts, quenching) or a third lifetime were observed, giving evidence for the 1 : 3 complex at 25 °C and −120 °C. Since these results give sufficient reasons to assume that the 1 : 3 complex does not exist and are therefore in big contrast to previous investigations, more effort will be put in this apparently simple system to clarify the formed species.

ACKNOWLEDGEMENTS. This project has received funding from the Euratom research and training program 2014-2018 under Grant Agreement no. 661880.

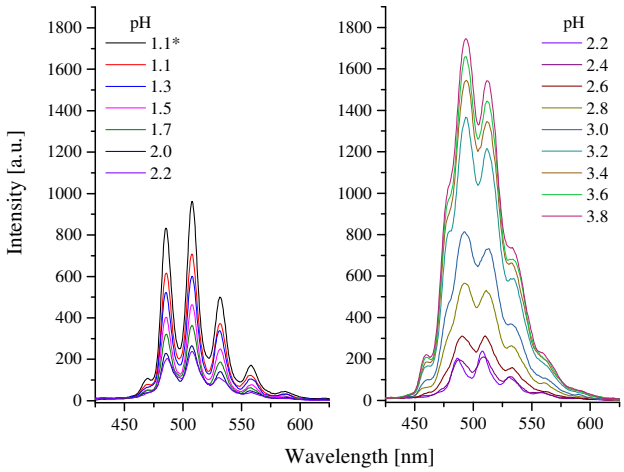

Fig. 1: Luminescence spectra of uranyl-acetate samples at 25 °C ($[UO_2^{2+}]$ = 50 µM, [AcOH] = 0.25 M, I = 1 M ($NaClO_4$)).

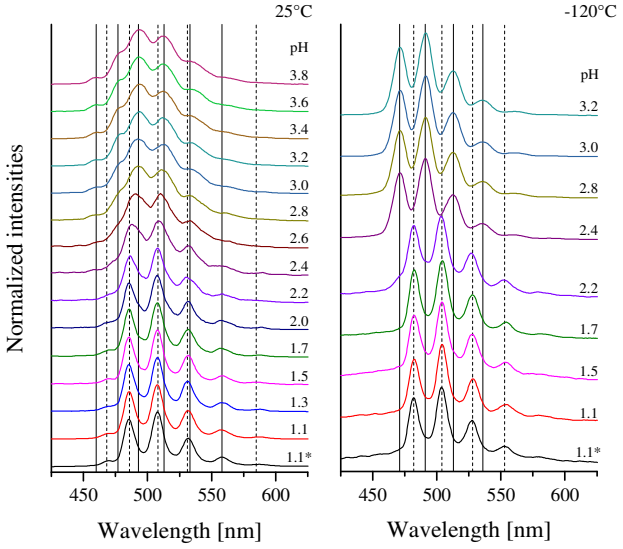

Fig. 2: Normalized luminescence spectra of uranyl-acetate samples at 25 °C (left) and −120 °C (right).

Tab. 1: Emission bands and calculated lifetimes.

Species	Emission Bands (nm)		Lifetimes (µs)	
	25 °C	−120 °C	25 °C	−120 °C
UO_2^{2+}	468, 486, **508**, 532, 558, 585, 619	482, **504**, 528, 553	2.11 ± 0.04 *	319 ± 22
Species 2 ($UO_2(AcO)_2$)	460, **493**, 513, 533, 562, 477	471, **491**, 513, 536	0.48 ± 0.03	922 ± 11

[1] Günther, A. *et al.* (2011) *Radiochim. Acta* **99**, 535–542.
[2] Sladkov, V. (2014) *J. Photochem. Photobiol., A* **295**, 40–45.

U(VI) complexation with selected flavonoids investigated by absorption and emission spectroscopy at light acidic conditions

A. Günther, G. Geipel

Flavonoids are secondary plant compounds and have important properties. Beside their antioxidant activity and effects as enzyme inhibitors, they can bind metals ions.[1] The possible release of flavonoids from the root into the soil can affect the migration of radionuclides in the biological and geological environment. In this work, the complexation behavior of selected flavonols and a flavonol glycoside towards U(VI) were spectroscopically investigated and the corresponding complex stability constants were determined.

EXPERIMENTAL. Methanolic solutions containing a constant concentration of flavonol (Fig. 1, 2×10^{-5} or 5×10^{-5} M) and variable uranyl perchlorate concentrations (5×10^{-6}–2.5×10^{-4} M) at ionic strength of 0.1 M were prepared. The redox voltage of 230 mV (~ pH 3) was adjusted with methanolic $HClO_4$ or NaOH.

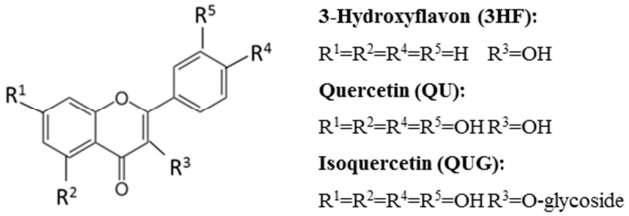

Fig. 1: Chemical structure of selected flavonols (neutral form at 230 mV).

The UV-vis spectra were recorded with a Varian Cary 50 Bio spectrophotometer. Time-resolved laser-induced fluorescence (TRLF) measurements were carried out by using a Spectra-Physics fs-laser system (800 nm, 1 kHz) with a pulse width of 130 fs and variable excitation wavelengths in the range of 270 and 410 nm. All spectroscopic measurements were performed at room temperature.

RESULTS. Figure 2 illustrates the evolution of the UV-vis spectra of QUG-U(VI) system with increasing metal/ligand concentration ratios.
Beside the decrease/increase of the absorption intensity of the bands for the free ligand, a new band appears at 420 nm (3HF/U(VI) – 390 nm, QU/U(VI) – about 450 nm).

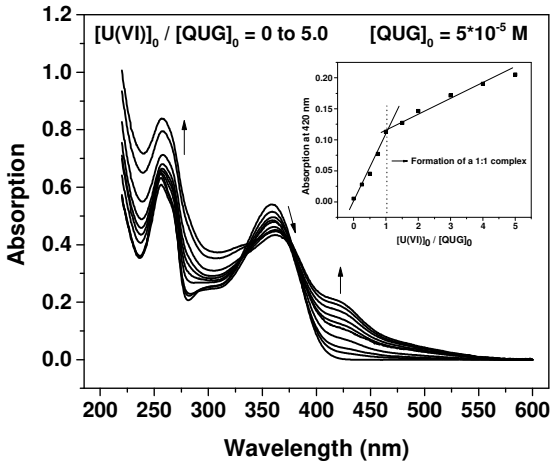

Fig. 2: UV-vis absorption spectra of QUG as a function of the U(VI) concentration and analysis of the data at 420 nm.

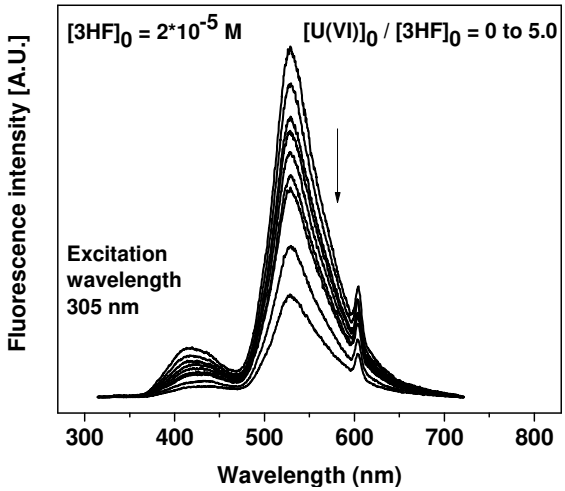

Fig. 3: Fluorescence spectra of 3-Hydroxyflavon as a function of the U(VI) concentration.

The plot of the absorption values at λ= 420 nm of the molecule complex spectra *versus* the metal to ligand ratio (Fig 2, inset) suggests the formation of a complex showing a 1 : 1 stoichiometry under light acidic conditions. Comparable results were obtained for the complex behavior of 3-Hydroxyflavon and quercetin under the given experimental conditions.
The formation of U(VI)-flavonol complexes was also demonstrated by the decrease of the fluorescence intensities of the free ligands with increasing U(VI) concentration (static quenching; example in Fig. 3), as the organic U(VI) complexes showed not fluorescence.
The stability constants of the complexes were assessed based on the following reaction equations at constant proton concentration (230 mV, equations 1 and 2):

$$Flavonol + U(VI) \Leftrightarrow U(VI)\,flavonol \quad (1)$$

$$K = \frac{[U(VI)\,flavonol]}{[Flavonol]\cdot[U(VI)]} \quad (2)$$

Using factor analysis program HypSpec [2] or slope analysis, comparable complex stability constants (log *K*) were obtained for both spectroscopic methods and summarized in Tab. 1.

Tab. 1: Stability constants log *K* of the 1:1 U(VI) flavonol complexes.

Flavonol	UV-vis (HypSpec)	Femto-TRLFS (Slope)
3HF	4.90 ± 0.02	4.55 ± 0.35
QU	4.45 ± 0.01	4.67 ± 0.49
QUG	4.39 ± 0.03	4.01 ± 0.27

[1] Kasprzak, M. M. *et al.* (2015) *RSC Adv.* **5**, 45853–45877.
[2] Gans, P. *et al.* (2008) Protonic Software, Leeds.

A Surface Enhanced Raman Scattering spectroscopic study of UO_2^{2+} at trace concentration

C. Franzen, L. Carstensen,[1] T. Firkala,[2] R. Steudtner
[1]Technische Universität Dresden, Dresden, Germany; [2]Helmholtz Institute Freiberg for Resource Technology, Freiberg, Germany

Techniques for rapid screening of uranium in environmental samples are needed. This study entails the development of Surface-Enhanced Raman scattering (SERS) spectroscopy for analyzing uranium(VI) in aqueous media with improved sensitivity.

The state of uranium in aqueous solutions is of prime importance in many analytical fields. However, there are only a few spectroscopic techniques which allow the detection and characterization of uranium complexes at environmental concentrations. Conventional Raman spectroscopy, which is a useful method for characterizing aqueous uranium species, suffers from a relatively high detection limit. Based on the enhancement of Raman signals for analyte molecules adsorbed to a characteristically roughened metallic surface, SERS spectroscopy has great potential for the trace detection of molecules in environmental samples and their analysis due to its lower detection limit and high specificity. The first SERS studies of the interaction mechanism of uranyl on a solid silver surface and on a sol-gel silver surface have been published previously.[1, 2]

EXPERIMENTAL. *Uranyl(VI)-solution*: An aqueous solution containing 1 mM UO_2Cl_2 and 1 M NaCl background electrolyte adjusted to pH 2.5 was used in all experiments.
Silver-solution: 30 mg of $AgNO_3$ were suspended in 100 mL deionized water in a 250 mL Erlenmeyer flask which was wrapped into alumina foil. This solution was then heated up to 90 °C with continuous stirring. Slowly, 2.5 mL of 1 % sodium citrate were added and the solution was kept at 90 °C for 25 min. Subsequently, the solution was cooled down to room temperature and the colloidal silver solution was stored in a light proofed screw cap jar.
Silver-substrate: A commercial copper sheet was immersed into a 10 mmol/L $AgNO_3$ aqueous solution for 5 min. Very quickly the simple galvanization reaction resulted in a roughened silver layer on the copper surface. Directly after the galvanization the copper based silver substrate was immersed into the uranyl test solution for another 5 min and dried.
Raman-Spectroscopy: A confocal Raman microscope (Aramis from Horiba Labram), with a laser excitation wavelength of $\lambda_{exc.}$ = 532 nm was used. The uranyl solution was mixed with the colloidal silver solution at a ratio of 1 : 3 and filled in a 2 mL glass cuvette. For solid samples, a glass holder was used and the sample was analyzed through a 50X objective.

RESULTS. It could be clearly shown that both the silver-solution and the silver substrate provoked an enhancement of the uranium signal (Fig. 1). For the 1 mM uranyl solutions, no signal for the symmetric stretching ν_1 mode of UO_2^{2+} could be detected with conventional Raman (Fig. 1, black spectra), whereas the ν_1 mode becomes clearly observable in the SERS spectrum (Fig. 1, red spectra).
The symmetric stretching ν_1 mode of UO_2^{2+} appeared at around 836 cm^{-1} and 770 cm^{-1} in the spectra of the Ag-solution and Ag-substrate method, respectively. The shift of these frequencies in comparison to the symmetric stretching band of aqueous uranyl around 854 cm^{-1} are attributed to

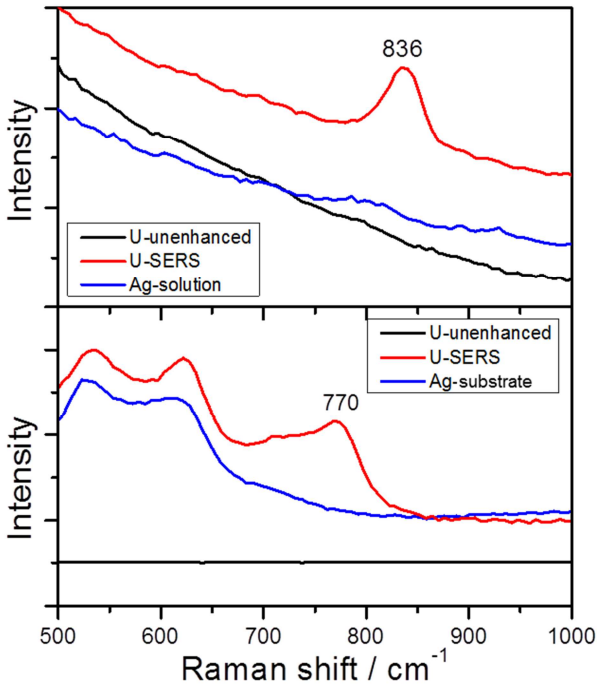

Fig. 1: Raman spectra of 1 mM uranyl solution. Ag-solution method (upper panel), Ag-substrate method (lower panel).

the development of a chemical bond between silver surface and uranyl species and are in good agreement with literature data. Depending on the applied measurement conditions and features of the SERS substrates, different researchers have assigned the distinct symmetric stretching mode of uranyl species at different wavenumbers, ranging from 700–840 cm^{-1}.[3, 4]
The results presented in this work demonstrate the great potential of SERS for the trace detection of uranium in environmental samples. This might be particular interesting, because there are portable Raman instruments, which could be used for in-line water quality monitoring in uranium contaminated sites. A similar application has been reported for arsenic in drinking water.[5]

ACKNOWLEDGEMENTS. The authors would like to thank S. Tsushima and H. Foerstendorf for fruitful discussions.

[1] Clavijo, R. E. *et al.* (1989) *Raman Spectrosc.* **20**, 461–465.
[2] Dai, S. *et al.* (1996) *Applied Spectrosc.* **50**, 536–537.
[3] Leverette, C. L. *et al.* (2009) *Vib. Spectrosc.* **50**, 143–151.
[4] Teiten, B.; Burneau, A. J. (1997) *Raman Spectrosc.*, **28,** 879–884.
[5] Du, J. *et al.* (2014) *Chem. Comm.* **50**, 347–349.

U(IV) fluorescence spectroscopy – A new speciation tool

S. Lehmann, R. Steudtner, V. Brendler

We combined absorption and fluorescence spectroscopy to study the speciation of U(IV) in solution in concentrations down to 10^{-6} M uranium. With our time-resolved laser-induced fluorescence setup we could determine the fluorescence decay time of U(IV) in perchloric as well as in chloric acid with 2.6 ± 0.3 ns at room temperature and 148.4 ± 6.5 ns at liquid nitrogen temperature. For the U(IV) sulfate system, we observed a bathochromic shift and a peak shape modification in the fluorescence spectra with increasing sulfate concentration in solution. Thus, the potential of U(IV) fluorescence for speciation analysis could be proven.

EXPERIMENTAL. First, a U(IV) stock solution was produced by reduction in an electrochemical cell. The formation of U(IV) was monitored by UV-vis spectroscopy and the residual content of U(VI) was determined by time-resolved laser-induced fluorescence spectroscopy (TRLFS) to be lower than 1 %. We studied the aqueous speciation of 10 mM to 1 µM U(IV) with various concentrations of perchloric, chloric and sulfuric acid.
To study these systems we used a combination of UV-vis spectroscopy with long path flow cell (LWCC), fluorometer and TRLFS. The excitation wavelengths λ_{exc} were 245 and 247 nm for TRLFS and fluorometric measurements, respectively. Additionally, a cryogenic unit was installed for measurements at liquid nitrogen temperature (77 K).

RESULTS. We detected the luminescence of the free U(IV) ion in acidic aqueous solution at room temperature (rt) and in frozen state at 77 K. At rt, we observed the typical fluorescence properties of U(IV) with the peak maxima at 321, 410 and 523 nm (Fig. 1) and a fluorescence decay time of 2.6 ± 0.3 ns in perchloric and chloric acid. A detection limit of 10^{-5} M at rt was determined, which was lowered by one order of magnitude by using cryo-TRLFS at 77 K. Simultaneously, the fluorescence lifetime increased up to 148.4 ± 6.5 ns. The spectroscopic results are in good agreement with earlier reports for rt and cryo measurements.[1, 2] With our setup we could study aqueous U(IV) systems with concentrations to be expected in the environment.[3, 4] In contrast to U(VI), which is often quenched by chloride, well resolved luminescence spectra of U(IV) were obtained in 0.1 as well as in 1 M HCl.
At low temperature, we observed a band splitting of the main band at 410 nm. Particularly for the U(IV) sulfate system, a peak shift and modification in dependence on speciation was observed (Fig. 2). The lifetime analysis indicated a three component system with free U(IV) and two U(IV) sulfate species. For U(IV), the actual NEA thermodynamic database also reports two sulfate species: USO_4^{2+}, and $U(SO_4)_2(aq)$.[5]
Therefore, the combination of UV-vis and TRLFS is a powerful tool for speciation determination of U(IV).

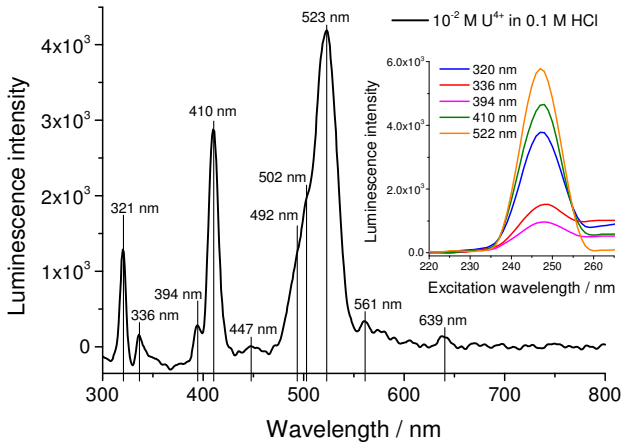

Fig. 1: Fluorescence spectrum of 10^{-2} M U(IV) in 1 M HCl excited at λ = 247 nm measured at 1 °C with fluorometer. The optimal excitation wavelength of all main peaks is shown in the inset.

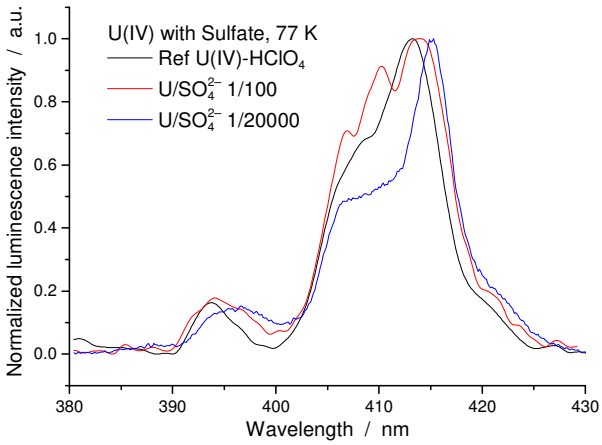

Fig. 2: TRLFS spectra of different U(IV)/Sulfate ratios excited at λ = 245 nm measured at liquid nitrogen temperature. Peak shift, shape modification and lifetime analysis indicated a three component system: free U(IV) and two U(IV) sulfate species.

ACKNOWLEDGEMENTS. The authors kindly acknowledge funding by the German Ministry of Economic Affairs and Energy under the grants 02E11334B.

[1] Lehmann, S. *et al.* (2010) *J. Radioanal. Nucl. Chem.*, **283**, 395–401.
[2] Kirishima, A. *et al.* (2004) *Radiochim. Acta* **92**, 705–710.
[3] Arnold, T. *et al.* (2011) *Geochim. Cosmochim. Acta* **75**, 2200–221.
[4] Bernhard, G. *et al.* (1998) *J. Alloys Compd.* **271**, 201–205.
[5] Guillaumont, R. *et al.* (2003) *Update on the chemical thermodynamics of U, Np, Pu, Am and Tc.* Elsevier, Amsterdam.

Synthesis and characterization of thorium(IV) and uranium(IV) complexes with Schiff bases

T. Radoske, J. März, P. Kaden, M. Patzschke, A. Ikeda-Ohno

We report herein the synthesis and characterization of several imine complexes of tetravalent thorium (Th(IV)) and uranium (U(IV)). The ligands investigated in this study are a *Schiff* base type, including the well-known salen ligand (H_2Le, Fig. 1). The complexation in solution was investigated by NMR measurements indicating paramagnetic effects of unpaired *f*-electrons of U(IV) on the ligand molecule. We also determined the solid-state molecular structures of the synthesized complexes by single crystal X-ray diffraction. The synthesized complexes show an eight-fold coordination geometry around the actinide center surrounded by two tetradentate ligands with 2N- and 2O-donor atoms.

The presence of organic ligands in nature could play an important role in determining the migration behavior of radionuclides in the environment. Organic substances containing both oxygen and nitrogen donor atoms have a strong coordination ability towards metals and, therefore, can potentially influence the chemical properties of radionuclides. These important factors should be taken into consideration for reliable safety assessment of radioactive waste storage and disposal. The possible interactions between radionuclides and naturally occurring organic substances can be studied by simplifying their representative functionalities. In this context, this study utilizes the tetradentate *Schiff* base salen ligand (H_2Le) and its derivative (Fig. 1), which could represent some major functionalities in natural enzymes.[1]

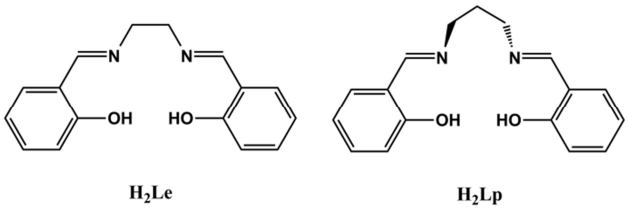

H_2Le H_2Lp

Fig. 1: Tetradentate *Schiff* base ligands; salen (H_2Le) and its derivative (H_2Lp).

EXPERIMENTAL. Materials handling and synthesis of compounds were performed in a water-free and N_2-filled glovebox and using standard Schlenk technique. Solvents were distilled from Na/K alloy and stored over molecular sieves (3 Å). Methanol was only degassed before distillation without the alloy. The starting compounds $ThCl_4(DME)_2$ [2] and UCl_4 [3] were synthesized by standard procedures reported in the literatures. Metal-ligand complexes were synthesized by mixing the metal tetrachloride and the ligand with a 1 : 2 ratio in methanol. Sodium methoxide was added to the ligand solution beforehand to promote deprotonation. The obtained precipitate was washed with pentane and redissolved into tetrahydrofuran. Single crystals suitable for XRD measurements were yielded by the diffusion of ether or methanol into the tetrahydrofuran solution containing the complex.

RESULTS. ^{1}H-NMR spectra of the U(IV)-salen complexes dissolved in THF (Fig. 2) show the absence of the hydrogens of hydroxyl groups indicating the complex formation between U(IV) and the O atoms of the hydroxyl groups of

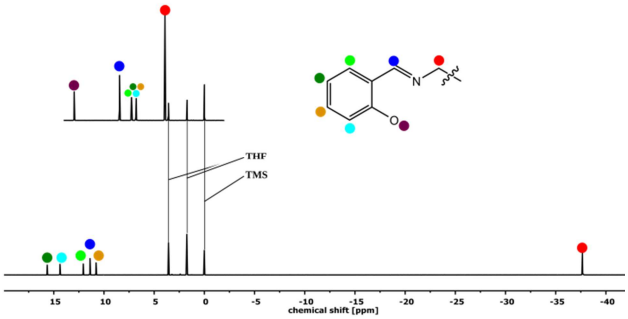

Fig. 2: ^{1}H-NMR spectra of H_2Le (top) and [ULe_2] (bottom) in THF-d8.

the ligand in solution. The observed large chemical shifts of over 40 ppm compared to the pure ligand suggest the paramagnetic effect originating from the *f*-electrons of U(IV). Single crystal XRD measurements of the Th(IV) and U(IV) complexes with the ligand H_2Lp reveal that two ligand molecules are coordinating to the metal center with 2N- and 2O-donor atoms, forming a square antiprismatic geometry around the metal center. When comparing the complexes [$ThLp_2$] and [ULp_2], the two complexes are isostructural, but the bond distances between the metal center and the donor atoms are slightly longer for the Th(IV) complex than for U(IV) due to the actinide contraction.[4]

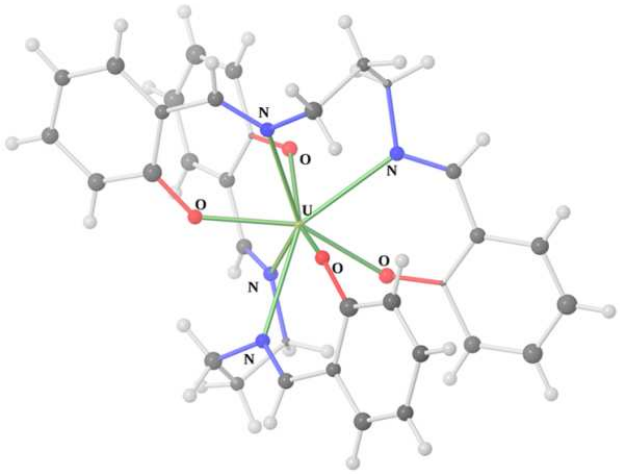

Fig. 3: Molecular structure of the complex [ULp_2].

ACKNOWLEDGEMENTS. We thank Dr. Olaf Walter at JRC-ITU for providing the studied *Schiff* base ligands.

[1] Maneiro, M. *et al.* (2003) *New J. Chem.* **27**, 727–733.
[2] Cantat, T. *et al.* (2010) *Chem. Commun.* **46**, 919–921.
[3] Patel, D. (2015) *New J. Chem.* **39** 7559–7562.
[4] Shannon, R. D. (1976) *Acta Cryst.* **A32**, 751–767.

Synthesis and characterization of chiral thorium(IV) and uranium(IV) benzamidinate complexes

S. Schöne, J. März, P. Kaden, M. Patzschke, A. Ikeda-Ohno

Two chiral benzamidinate complexes of tetravalent actinides (Th(IV) and U(IV)) were synthesized using a salt metathesis reaction of the corresponding actinide(IV) tetrachlorides and the potassium salt of the chiral benzamidine (*S*,*S*)-N,N-*Bis*-(1-phenylethyl)-benzamidine ((*S*)-HPEBA). The structure of the complexes was determined with single crystal X-ray diffraction. These are the first examples of chiral amidinate complexes of actinides.

Oxygen- and nitrogen-donor ligands are known to form stable complexes with actinides, which could potentially influence the migration behavior of these radioactive elements in a nuclear waste repository. Therefore, the understanding of the interaction mechanisms between actinides and these types of ligands would be crucial for the safety assessment of the waste repository. Based on this background, the present study focuses on the interaction of actinides with a benzamidinate ligand, which can be considered as a model of naturally occurring N-donor organic compounds. Furthermore, due to its chemical similarity to the relevant O-donor ligand of carboxylic acids, the comparison between these two major strong ligands is of particular scientific interest. The advantage to use amidinates is the possibility to tune the electronic properties on the donating atoms (i. e. coordinating N atoms) as well as steric properties by varying the substituents. Interestingly, only a limited number of chiral metal complexes with benzamidinates has been reported so far. Recently, the group of P. Roesky has shown an effective synthesis route for the chiral benzamidine (*S*,*S*)-N,N-*Bis*-(1-phenylethyl)-benzamidine ((*S*)-HPEBA) and the corresponding potassium salts,[1] and have successfully synthesized some lanthanide complexes with this chiral benzamidine.[2] The present study is inspired by these precedent studies to synthesize new benzamidine compounds of tetravalent actinides, Th(IV) and U(IV).

EXPERIMENTAL. All preparations and syntheses were performed in a water-free N_2-filled glovebox and standard Schlenk techniques. All solvents were distilled from Na/K alloy and stored over molecular sieve 4 Å. $ThCl_4(DME)_2$,[3] UCl_4,[4] and (*S*)-KPEBA[1] were prepared according to the standard procedures reported in the literature.

RESULTS. The synthesis route for the complexes [ThCl((*S*)-PEBA)$_3$] (**1**) and [UCl((*S*)-PEBA)$_3$] (**2**) is shown in Fig. 1.

The salt metathesis reaction can be easily monitored by a color change of the sample solution (toluene) from colorless to pale green, whereas the potassium chloride precipitates as an off-white solid.

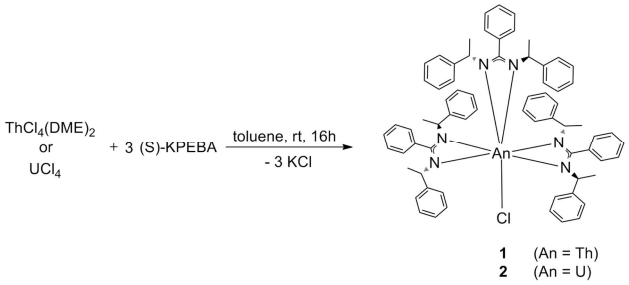

Fig. 1: Synthesis of [ThCl((*S*)-PEBA)$_3$] (**1**) and [UCl((*S*)-PEBA)$_3$] (**2**).

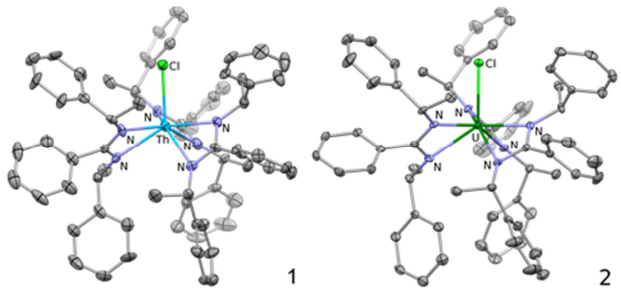

Fig. 2: Molecular structures of [ThCl((S)-PEBA)$_3$] (**1**, left) and [UCl((S)-PEBA)$_3$] (**2**, right).

Single crystals of complexes **1** and **2** were obtained by filtration of the resulting suspension, drying *in vacuo*, and recrystallization from a toluene/*n*-pentane solution. The crystal structures of the obtained single crystals were determined by single crystal X-ray diffraction. The determined molecular structures of **1** and **2** are shown in Fig. 2.

The Th(IV) and U(IV) complexes are isostructural with three benzamidinate ligands coordinating to the actinide(IV) cation. Additionally, one chloride (Cl^-) is bound to the actinide center resulting in the monocapped distorted octahedral coordination sphere. All three benzamidinate ligands are coordinating to the metal center asymmetrically and the tilt angle between the plane consisting of the coordinating N-C-N atoms of the amidinate ligand and the An–Cl axis varies within the three ligands from 40.22° to 50.44°. Due to the steric hindrance of the bulky amidinate ligands, no symmetrical coordination was observed in the obtained complexes. The averaged U–N bond length in **2** (2.43 Å) is slightly shorter than the Th–N bond length in **1** (2.49 Å) due to the actinide contraction.[5]

ACKNOWLEDGEMENTS. We thank Prof. Dr. Roesky (Karlsruhe Institute of Technology) for providing the benzamidinate ligand used in this study.

[1] Benndorf, P. *et al.* (2011) *J. Organomet. Chem.* **696**, 1150–1155.
[2] Benndorf, P. *et al.* (2012) *Chem. Eur. J.* **18**, 14454–14463.
[3] Cantat, T. *et al.* (2010) *Chem. Commun.* **46**, 919–921.
[4] Patel, D. (2015) *New J. Chem.* **39**, 7559–7562.
[5] Shannon, R. D. (1976) *Acta Crystallogr., Sect. A* **32**, 751–767.

Ln(III)-malate complexation studies using TRLFS and micro titration calorimetry

F. Taube,[1] M. Acker,[2] B. Drobot,[1] S. Taut,[2] T. Stumpf

[1]Professorship Radiochemistry, Technische Universität Dresden, Dresden, Germany; [2]Central Radionuclide Laboratory, Technische Universität Dresden, Dresden, Germany

The complexation of trivalent lanthanides was studied using Time-Resolved Laser-Induced Fluorescence Spectroscopy (TRLFS) and Isothermal Titration Calorimetry (ITC). Formation constants, complexation enthalpies and fluorescence lifetimes are determined over a wide pH range at I = 0.5 m NaCl.

Concrete is widely used as engineering barrier and for waste conditioning in waste repositories. Its binding agent is cement. Organic cement additives, which are used to improve the workability of fresh concrete, are complexation agents for radionuclides after they have been released during the concretes degradation. Thus, these additives might have an impact on the aqueous geochemistry of actinides. Here, the α-hydroxydicarboxylic acid or malic acid is examined. It is used in water-reducers or retarders in cement.[1, 2]

EXPERIMENTAL. TRLFS was performed using 5×10^{-6} M $EuCl_3$ and 0.01 M malic acid for the series with varied pH (pH 1–11). For the series at fixed pH, the concentration of malate varied from 0.01–0.5 M. The ITC technique is described elsewhere.[3] The measurements were performed using 1–5 mM $NdCl_3$ and 0.03–0.07 M malate at fixed pH values. In all experiments the ionic strength was adjusted to 0.5 mol·kg^{-1} NaCl.

RESULTS. In TRLFS experiments with Eu(III) malate, stability constants and lifetimes of three complexes (Tab. 1) were determined using the factor analysis program SPECFIT and the three-dimensional parallel factor analysis code PARAFAC.[4] Additionally to these species, a fourth species, probably Eu(III)-malate-hydroxide, was observed at high pH values.

In the thermogram measured by ITC (Fig. 1) three different effects are clearly visible. The integrated heat curve was therefore fitted using a theoretical model of three complexes and the protonation constants and enthalpies from separate experiments. The fit results are shown in Tab. 1. The first complexation step is endothermic while the second and third steps are slightly exothermic at this ionic strength. Small enthalpies around zero are known for small organic ligands due to the compensation of dehydration energy and binding energy of the reacting species. The complexation enthalpies for malate have similar values or a slightly smaller endothermic contribution than the enthalpies for the Eu-lactate complexes. Because these show bidentate binding with the carboxylate group and the deprotonated hydroxyl group,[5] this is a strong indicator for a chelating binding mode of the Nd-malate complexes, too. Preliminary results of EXAFS experiments with Am-malate are confirming the structural similarity to the Am-lactate system.

The stability constants of both methods agree well within uncertainties. The results in Tab.1 are similar to those determined in Kitano *et al.* (I = 1 M $NaClO_4$).[6] The averaged speciation for lanthanide-malate complexation (Fig. 2) can be assigned to trivalent actinide speciation as well. This is important for the long term safety assessment in a nuclear waste repository.

ACKNOWLEDGEMENTS. The project is funded by BMWi (contract number: 02E11451G).

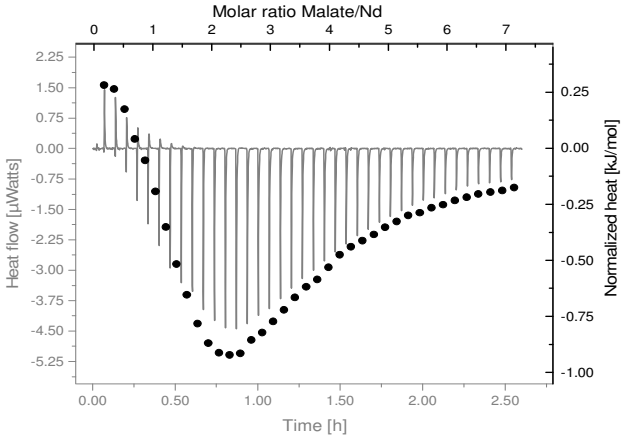

Fig. 1: Thermogram (gray) and integrated heat curve (black) of Nd-malate titration.

Tab. 1: Stability constants and lifetimes determined by TRLFS (left col.) and ITC (middle col.) at I = 0.5 m NaCl and T = 25 °C.

$\log \beta_n$ Eu(III)	Lifetime (µs)	$\log \beta_n$ Nd(III)	$\Delta_R H_n$ (kJ·mol^{-1})	Species
	112 ± 2			Ln^{3+}
4.36 ± 0.22	141 ± 2	4.85 ± 1.04	0.32 ± 0.24	$LnMal^+$
7.92 ± 0.36	207 ± 12	8.35 ± 1.42	−1.37 ± 0.82	$LnMal_2^-$
10.31 ± 0.46	281 ± 4	11.03 ± 0.22	−2.54 ± 1.58	$LnMal_3^{3-}$

2σ uncertainty.

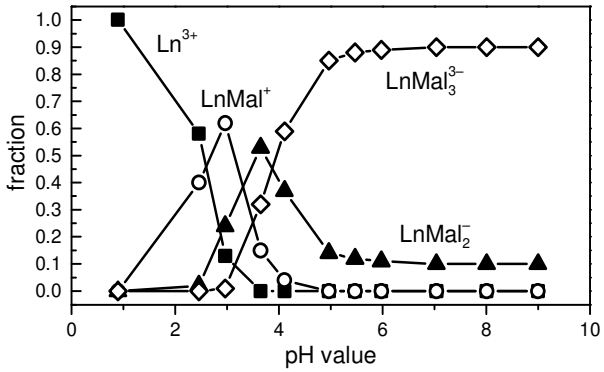

Fig. 2: Averaged computed speciation from ITC and TRLFS for Ln(III)-malate complexation, I = 0.5 m NaCl.

[1] Ramachandran, V. S. (1995) *Concrete Admixtures Handbook,* Noyes Publications, National Research Council, Ontario, Canada.
[2] Glaus, M. A. *et al.* (2004) *Technical Report 03-09*, Paul Scherrer Institut, Villigen PSI.
[3] Taube, F. *et al.* (2015) *Report HZDR−059*, p.40.
[4] Drobot, B. *et al.* (2015) *Chem. Sci.* **6**, 964–972.
[5] Barkleit, A. *et al.*(2014) *Dalton Trans* **43**, 11221–11232.
[6] Kitano, H. *et al.* (2006) *Radiochim. Acta* **94**, 541–547.

Hydroxyquinoline-Calix[4]arene-Conjugates as ligands for lanthanide complexes: Preparation, characterization, and extraction properties

A. Mansel, A. Jäschke,[1] M. Kischel,[1] B. Kersting[1]

[1]Institut für Anorganische Chemie, Universität Leipzig, Leipzig, Germany

The synthesis of a calixarene-based N_4O_4 donor ligand H_6L, in which two 8-hydroxyquinoline-2-carbaldehyde units are appended *via* hydrazone-carbonylmethoxy linkages in a 1,3-arrangement to the lower rim of tert-butyl-calix[4]arene and its coordination properties towards Eu^{3+} are described. Moreover, the ligand H_6L was found to extract Eu^{3+} and Tb^{3+} at pH 7–8 from aqueous solution, as established by radiotracing using the radionuclides ^{160}Tb and ^{152}Eu.

EXPERIMENTAL. *Synthesis of the ligand H_6L.* The new ligand H_6L was prepared in three steps starting from para-tert-butylcalix[4]arene. The reaction with ethyl bromoacetate in acetonitrile gave the calix[4]arene with the two ethyl acetate groups appended in 1,3-position of the calix[4]arene backbone. Treatment with hydrazine monohydrate gave the corresponding hydrazide in nearly quantitative yield. In the last step, 8-hydroxyquinoline-2-carbaldehyde was subjected to a condensation reaction with the hydrazide to give the target compound, which was isolated in the neutral H_6L form. The yield was 73 %. H_6L is readily soluble in chloroform and dichloromethane. All compounds gave satisfactory elemental analysis and their formulation was confirmed by ESI-MS, ^1H, ^{13}C NMR, IR, and UV-vis spectroscopy. H_6L was also characterized by X-ray crystallography.

Liquid-liquid extraction. In orienting experiments, we studied the ability of H_6L to act as an extraction agent for lanthanide ions, in view of reports that functionalized calixarene ligands exhibit good extraction efficiency. The two-phase solvent extraction studies were performed in chloroform/water mixtures and were monitored by radiotracing utilizing ^{160}Tb as well as ^{152}Eu. The radionuclides were purchased with a specific activity of 980 MBq/mg ^{160}Tb and 587 MBq/mg and were dissolved in 1 mL 10 mM/L nitric acid to give the stock solution. All radiometric measurements were performed by using a γ-counter. The ligand H_6L was dissolved in chloroform to give solutions with a concentration range from 0.5–1000 µM/L. The radionuclide stock solutions were diluted to give an activity of ~10 kBq/mL. The pH was adjusted to the desired value with 0.1 M nitric acid or ammonia. 3 mL of the organic solution was shaken with 3 mL of the aqueous solution in a stoppered vial on a horizontal shaker at 300 min^{-1}. The phases were allowed to equilibrate for 60 min. After separation of the phases for 1 min, an aliquot of 2 mL of the aqueous phase were measured by γ-counting in comparison to 2 mL of the aqueous solution before extraction. The percentage extraction was calculated by means of the two activities.

RESULTS. Figure 1 shows the extraction yields of H_6L towards Tb^{3+} and Eu^{3+} as a function of pH. The extraction yields markedly depend on the pH value showing a sigmoidal profile of the lanthanide extraction (~95–98 %), which is nearly quantitative above pH ~7 at a metal to ligand ratio of 1:10. The strong pH dependence is in good agreement with the acid-base behavior of H_6L, which is considered to be present in its triply deprotonated form based on the pK_a values of the hydroxyquinoline and hydrazine units. Deprotonation of H_6L was also implied by a shift of the pH value of the aqueous phase that accompanied the extraction of the Ln^{3+} ions. Finally, the addition of H_2SO_4 lead to 92 % back-extraction of the lanthanide ion at a pH value of 4. Overall, H_6L described in this study exhibits good extraction ability for Tb^{3+} and Eu^{3+} ions which, due to its solubility properties, may be of use as an alternative extraction agent for lanthanide ions.

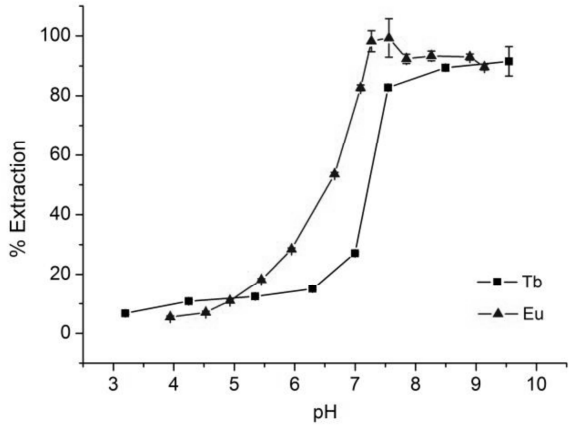

Fig. 1: Extraction yields obtained for H_6L at different pH values. Conditions: chloroform/water (1:1, v:v), $[Ln^{3+}]$ = 100 µM/L, $[H_6L]$ = 1 mM/L, 25 °C, equilibration time 60 min.

ACKNOWLEDGEMENTS. The project (SE-FLECX) is funded by Federal Ministry of Education and Research (033R132A).

Long-Lived Radionuclides & Transport Phenomena in

GEOLOGICAL SYSTEMS

Uranium(VI) retention by Ca-bentonite under (hyper)alkaline conditions

T. Philipp, K. Schmeide

The sorption behavior of U(VI) on Ca-bentonite was studied in saline, (hyper)alkaline solution *via* batch experiments. At pH 8.5–9.5 sorption is low in the presence of CO_2 due to the formation of weakly sorbing uranyl carbonate species, which have been observed to dominate speciation up to pH 10 by time-resolved laser-induced fluorescence spectroscopy (TRLFS). In the pH region 10–12, U(VI) retention is almost complete. The retention can either be attributed to strongly sorbing uranyl hydroxo complexes or to a partial precipitation of uranium due to an altered solubility of U(VI) induced by ions leached out of the bentonite.

Bentonite is considered as buffer material within the geotechnical barrier of deep geological repositories for radioactive waste.[1] Therefore, profound understanding of the radionuclide retention processes in bentonite under environmentally relevant conditions is essential for the long-term safety assessment of such repositories.
The pore water chemistry of North German clay formations is characterized by high ionic strengths,[2] promoting the corrosion of concrete, which is part of the engineered barrier. Upon corrosion, hyperalkaline ($10 < pH < 13$) cement pore waters evolve, which, in turn, can alter the retention potential of bentonite towards radionuclides.[3] The sorption behavior of U(VI) in such hyperalkaline environments is largely unknown. Therefore, batch sorption experiments were conducted in combination with TRLFS in order to gain insight into the underlying processes on the molecular level.

EXPERIMENTAL. Batch sorption experiments of U(VI) on Ca-bentonite were performed, varying the following parameters: U(VI) concentration: 1×10^{-9}–1×10^{-4} M, solid to liquid (S/L) ratio: 3–20 g/L, and pH 8–13. All experiments were conducted in the absence as well as in the presence of CO_2 using a so called 'diluted Gipshut solution' (2.5 M NaCl, 0.02 M $CaCl_2$, 0.02 M Na_2SO_4, 0.0051 M KCl) as electrolyte.[4] Bentonite suspensions were pre-equilibrated for 2–3 weeks. Sorption time was 7 days.
The aqueous speciation of U(VI) in the diluted Gipshut solution (pH range 8.5–12) was investigated with cryo-TRLFS (−120 °C) using a pulsed Nd:YAG laser (0.3 mJ, 266 nm).

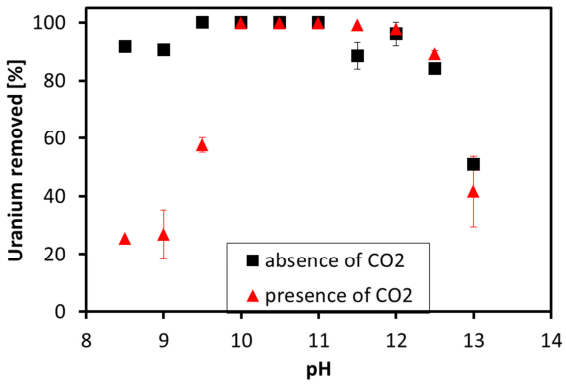

Fig. 1: U(VI) sorption on Ca-bentonite (10 g/L) as a function of pH in diluted Gipshut solution (I = 2.63 M) in the presence (c(U) = 1×10^{-6} M) and absence (c(U) = 5×10^{-7} M) of CO_2.

RESULTS. At pH 8, log(K_d) values of 3.03 L/kg and 2.19 L/kg were determined from sorption isotherms in the absence and in the presence of CO_2, respectively (data not shown). The reduced U(VI) sorption in the presence of CO_2 up to pH 9.5 (Fig. 1) can be explained with the formation of only weakly adsorbing uranyl carbonate species. The TRLFS spectra verify the prevalence of these complexes, which show a characteristic shift of the maxima to lower wavelength compared to the uranyl aquo ion (Fig. 2).

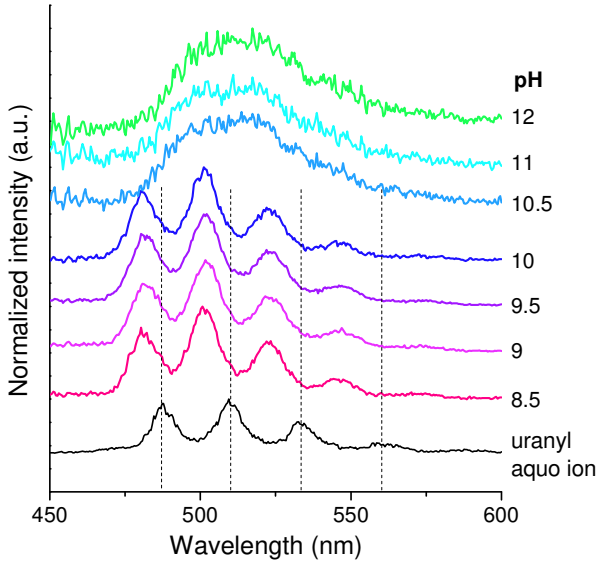

Fig. 2: Luminescence spectra of U(VI) (c(U) = 1×10^{-6} M) in diluted Gipshut solution in the presence of CO_2.

In the pH region 10–12, an almost complete retention of U(VI) was observed in the absence as well as in the presence of CO_2 (Fig. 1). Above pH 10.5, TRLFS measurements revealed an abrupt change in U(VI) speciation to uranyl hydroxo complexes even in the presence of CO_2 (Fig. 2). A strong sorption of the presumably prevailing $UO_2(OH)_3^-$ complex might explain the quantitative removal in this pH range. However, also precipitation processes have to be considered. Even when the solubility of U(VI) in the initial Gipshut solution is given, leaching of the bentonite modifies the electrolyte composition, thus influencing the U(VI) solubility. Ions leached out of the bentonite to significant amounts are Ca, Mg, Si, Al and CO_3^{2-}. In the future, pH-dependent solubility tests of U(VI) in the leachate of Ca-bentonite will be performed. Furthermore, the U(VI) surface complexes shall be examined with TRLFS to get insight into the mechanisms of U(VI) removal.
At pH > 12, the U(VI) retention decreases again (Fig. 1), presumably due to the formation of the anionic uranyl hydroxo complex $UO_2(OH)_4^{2-}$, that is strongly repulsed by the negatively charged mineral surface at high pH.

ACKNOWLEDGEMENT. This work was funded by the BMWi (No. 02 E 11415B).

[1] Lommerzheim, A. *et al.* (2014) *Report DBETEC 08-2014-Z.*
[2] Brewitz, W. (1982) Report *GSF-T 136.*
[3] Gaucher, E. C. *et al.* (2006) *Waste Manage* **26**, 776–788.
[4] Meleshyn, A. (2015), personal communication.

Stability of uranium(VI) doped CSH phases in high saline water

J.-M. Wolter, K. Schmeide

To evaluate the long-term stability of U(VI) doped calcium silicate hydrate (CSH) phases at high saline conditions, leaching experiments with NaCl, NaCl/Na_2SO_4 and NaCl/$NaHCO_3$ containing solutions were performed. Time-resolved laser-induced fluorescence spectroscopy (TRLFS), infrared spectroscopy (IR) and X-ray powder diffraction (XRD) were applied to study the U(VI) binding onto the CSH phases and to get a deeper understanding of structural changes due to leaching. Results indicate that neither NaCl nor Na_2SO_4 affect the structural stability of CSH phases and their retention potential for U(VI). However, carbonate containing solutions lead to a decomposition of CSH phases and thus, to a release of incorporated uranium.

Cementitious materials will be used for the geotechnical barrier of a deep geological repository where long-lived radioactive waste like used fuel rods will be stored.[1] Calcium silicate hydrate (CSH) phases, as main component of hardened cement paste, are known for their retention potential for radionuclides like uranium which is the main component of used fuel rods.[2] The pore waters of North German clay stone formations are characterized by high ionic strengths,[3] which potentially lead to a corrosion of concrete. Thus, with respect to long-term safety assessment of cement containing repositories chemical alteration processes at high saline conditions have to be studied. Therefore, the leaching of U(VI) doped CSH phases in high ionic strengths electrolyte solutions is studied in batch experiments in combination with spectroscopic methods.

EXPERIMENTAL. All experiments were performed in an inert gas box (CO_2 and O_2 < 2 ppm). CSH phases were prepared in artificial cement pore water (0.18 M KOH, 0.114 M NaOH) in the presence of 2×10^{-5} M U(VI), starting from fumed silica and carbonate-free CaO, at a solid-to-liquid (S/L) ratio of 24 g/L. The CSH phases possessed calcium-to-silicon (C/S) ratios between 1.0 and 2.0 and U(VI) loadings from 32 to 54 ppm (Tab. 1). TRLFS measurements were performed at 153 K (0.3 mJ, 266 nm). For leaching experiments, the CSH phases were equilibrated in 2.5 M NaCl, 2.5 M NaCl/0.5 M Na_2SO_4 or 2.5 M NaCl/0.02 M $NaHCO_3$ (S/L = 10 g/L) over a time period of 780 h. During this time the solutions were analyzed for Ca, Si and U.

Tab. 1: Composition of synthesized CSH phases.

C/S ratio	U (ppm)	U (mol/kg)
1.0	32	1.3×10^{-4}
1.6	37	1.5×10^{-4}
2.0	54	2.3×10^{-4}

RESULTS. The formation of CSH phases is confirmed by XRD and IR spectroscopy (data not shown). The TRLFS spectra obtained for the various CSH phases (not shown) are in agreement with those reported by Tits *et al.*[4] Thus, an incorporation of U(VI) in the CSH phases is verified. The results of leaching experiments are exemplarily shown for the CSH phase with C/S ratio of 1.6 for Ca and U in Figs. 1 and 2. The release of calcium into the supernatant solution in presence of NaCl and Na_2SO_4 is shown in Fig. 1.

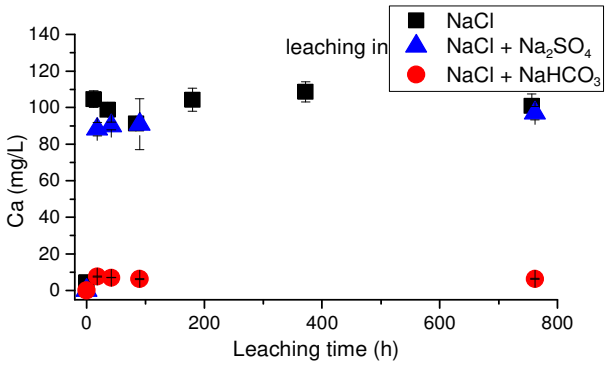

Fig. 1: Calcium concentration in leaching solution as a function of leaching time obtained for CSH phases with C/S ratio of 1.6.

This can mainly be attributed to a release of calcium from the interlayers of CSH phases. Simultaneously, the pH values of the supernatant solutions increases to values between 11.2 and 12, depending on the C/S ratio. In the presence of $NaHCO_3$, the calcium concentration in solution is much lower due to precipitation of $CaCO_3$, and pH values between 11.4 and 10.1 are observed.
In the presence of NaCl and Na_2SO_4, the release of silicon (data not shown) and uranium (Fig. 2) is minimal. In the presence of $NaHCO_3$, however, the silicon and uranium concentration in solution is increased. Since silicon can only be released from the complex layers of CSH phases, the release of silicon and simultaneously, the release of uranium can be related to a decomposition of the CSH phases in the presence of carbonate. Spectroscopic investigations also confirmed the decomposition of CSH phases and the release of uranium due to carbonate.

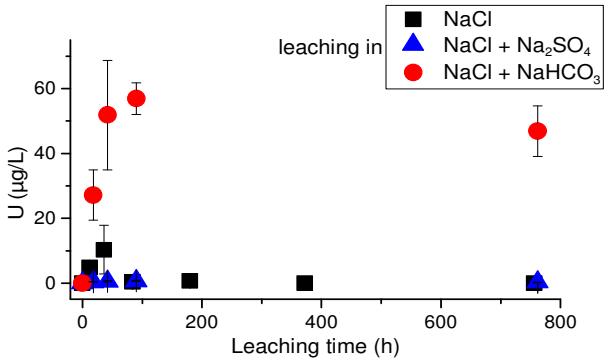

Fig. 2: Uranium concentration in leaching solution as a function of leaching time obtained for CSH phases with C/S ratio of 1.6.

ACKNOWLEDGEMENT. This work was funded by the BMWi (No. 02 E 11415B).

[1] Lommerzheim, A. *et al.* (2014) *Report DBETEC 08 2014 Z.*
[2] Batchelor, B. (2006) *Waste Manage.* **26**, 689–698.
[3] Brewitz, W. (1982) Report *GSF-T 136.*
[4] Tits, J. *et al.* (2011) *J. Colloid Interface Sci.* **359**, 248–256.

The ternary sorption system U(VI)-phosphate-silica explained by spectroscopy and thermodynamic modelling

H. Foerstendorf, M. Stockmann, M. J. Comarmond,[1] K. Heim, R. Steudtner, K. Müller, V. Brendler, T. E. Payne[1]

[1]Australian Nuclear Science and Technology Organisation, Lucas Heights, Australia

Spectroscopic data of sorption processes potentially provide direct impact on Surface Complexation Modelling (SCM) approaches. Based on spectroscopic data of the ternary sorption system U(VI)/phosphate/silica strongly suggesting the formation of a precipitate as the predominant surface process, SCM calculations accurately reproduced results from classical batch experiments.

Phosphate is known to influence uranium sorption in natural systems and model minerals.[1, 2] In the presence of phosphate, the spectroscopic results of the sorption processes of U(VI) on SiO_2, a major component of soils and rocks, strongly suggested the predominant formation of a precipitation at the oxide surface. Surface Complexation Modelling (SCM) was used for predictive modelling and provided insight on the proposed sorption processes.

EXPERIMENTAL. The performance of the batch experiments, *in situ* IR experiments, and SCM calculations are described elsewhere.[3]

RESULTS. The tracking of the sorption processes by *in situ* IR spectroscopy is accomplished by consecutive acquisition of spectra with a time resolution in the sub minute range. Within the first 10 minutes after sorption of U(VI) in the presence of phosphate was induced, the spectrum exhibits a weak positive band (marked by * in Fig. 1A) reflecting the $\nu_3(UO_2)$ mode of the uranyl(VI) ion. This band evolves with ongoing sorption and shows an increased intensity in the spectrum of the late sorption process which is shown with reduced ordinate scaling for clarity (Fig. 1B). In the frequency range above 950 cm^{-1}, superimposed bands at 1125 and 994 cm^{-1} develop with ongoing sorption (Fig. 1B). A comparison with spectra of an aqueous solution and of a precipitate obtained from U-phosphate solutions (data not shown) and earlier investigations suggests the formation of

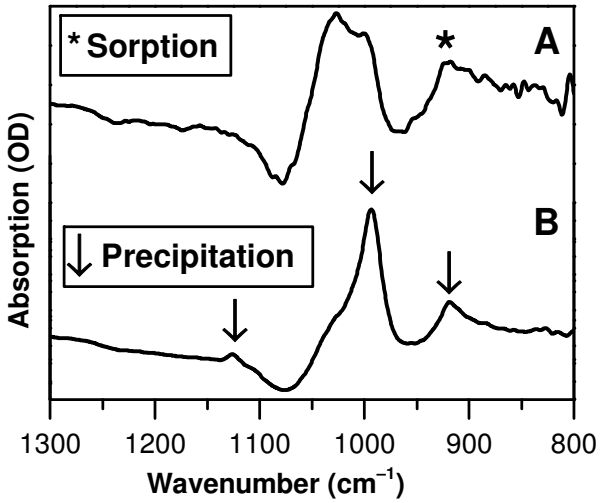

Fig. 1: Mid-IR spectra obtained within the first 10 minutes (A) and after 60 minutes of exposure time of an aqueous U(VI)/P solution (B) at pH 4. The bands marked by (*) and (↓) represent sorption complexes and precipitates at the SiO_2 surface, respectively. Note that the ordinate scaling of the latter spectrum is reduced by a factor of 0.3 for clarity ($[U]_{init}$ = $[P]_{init}$ = 20 µM, 0.1 M NaCl).

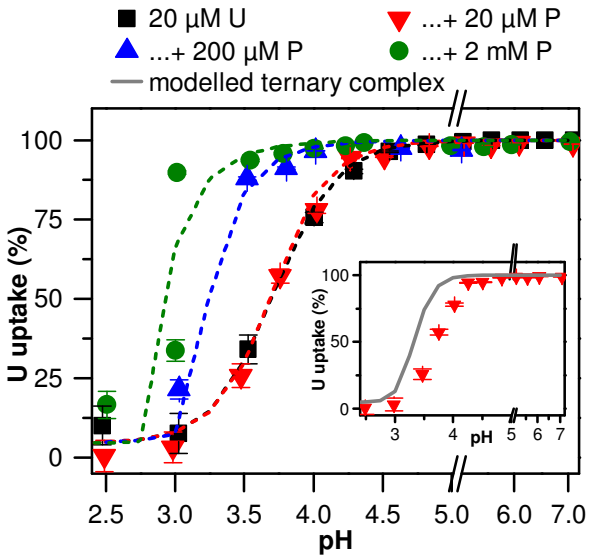

Fig. 2: Uranium(VI) uptake onto SiO_2 in the presence of different phosphate concentrations. Total [U] = 20 µM; Total [P] = 0 µM (black squares), 20 µM (red triangles), 200 µM (blue triangles) or 2,000 µM (green dots) (SiO_2 mass loading = 10 g L^{-1}; 0.1 M NaCl; equilibrium with air; 25 °C). Predictive results of Surface Complexing Modeling for the batch experiments performed at given phosphate concentrations are plotted as dashed lines. Inset: The respective batch and SCM results for [U] = [P] = 20 µM if formation of a ternary surface complex is considered. Note that for clarity reasons an axis break was added in the abscissa and only the largest error bars are shown at low pH values.

a surface precipitate.[4] In addition, from *in situ* IR and luminescence spectroscopy on the binary sorption system U(VI)-silica, the formation of two uranyl(VI) surface species are strongly suggested.[3, 5]

According to the spectroscopic results and literature data, the two binary uranyl(VI) surface species $\equiv SiO_2UO_2^0$ and $\equiv SiO_2UO_2OH^-$, and relevant solid phases – most probably Na-Autunite – are likely to be formed under the prevailing conditions and were considered during the predictive sorption modeling. The results clearly demonstrate that both processes, adsorption and precipitation, contribute to the removal of U(VI) from the aqueous phase. Both binary surface species in addition to the surface precipitate Na-Autunite describe the experimental data quite well as shown in Fig. 2 (dashed lines). By considering the ternary surface complex an overestimation of the experimental data, mainly for the 20 µM U, 20 µM P system, can be observed (Fig. 2, inset). While the key findings of the present work shows that a uranyl-phosphate ternary species is not required to explain the experimental data, the formation of ternary surface species might occur during the sorption processes as transient species being relevant only under highly diluted conditions.[3]

[1] Payne, T. E. *et al.* (1998) *Adsorption of Metals by Geomedia*, p. 75–97, Academic Press, San Diego, U.S.A.
[2] Del Nero, M. *et al.* (2010) *J. Colloid. Interface Sci.* **342**, 437–444.
[3] Comarmond, M. J. *et al.* (2016) *Environ. Sci. Technol.* **50**, 11610–11618.
[4] Müller, K. *et al.* (2013) *Chem. Geol.* **357**, 75–84.
[5] Zhao, Y.-J. *et al.* (2015) *Nucl. Sci. Tech.* **26**, S10313-1–8.

Uranium(VI) sorption onto magnetite: Increasing confidence in surface complexation models using chemically evident surface chemistry

F. Bok

Surface complexation models have made great efforts in describing the sorption of various radionuclides on naturally occurring mineral phases. Unfortunately, many of the published sorption parameter sets are built upon unrealistic or even wrong surface chemistry. This work describes the benefit of combining spectroscopic and batch sorption experimental data to create a reliable and consistent surface complexation parameter set.

In the system uranium(VI)-magnetite-water, two main retention processes occur: sorption and reduction. The reduction of U(VI) to its tetravalent form and the immobilization caused by the formation of hardly soluble uranium(IV)-(hydr-)oxides is well known. This process was found to occur within days to months. The sorption of U(VI) onto the surface of magnetite is an even faster process (< 4 h).[1] However, the current models are insufficient to describe natural systems due to the lack of parameter for carbonate-containing surface complexes.

CALCULATIONS. Already published experimental data were used to re-evaluate the $\log_{10}K$ values needed to describe the sorption of U(VI) onto magnetite. The experimental data points for the fitting procedures were re-digitized using the software package Engauge-Digitizer.[2] For the fitting procedures, the speciation code PHREEQC[3] was coupled with the parameter estimation software UCODE2005[4] using the aqueous speciation and mineral solubility parameters based on the PSI/Nagra Chemical Thermodynamic Database 12/7.[5] The Diffuse-Double-Layer model (DDL) was used to describe the sorption process.

To create a consistent parameter set, first the protolysis constants ($pK_{a1/2}$) for magnetite were fitted using the titration data from literature[1] in combination with published surface site density data.[6] In the next step, the formation constant of a surface complex within the carbonate-free system was fitted using the sorption data from literature.[1] Although there are no spectroscopic studies on the structure of surface complexes of uranium on magnetite, it can be assumed that the spectroscopic results of goethite can be extrapolated and thus, a bidentate surface complex was chosen.[7]

$$2 \equiv FeOH + UO_2^{2+} + 3\,H_2O \leftrightarrow (\equiv FeO)_2H{-}UO_2(H_2O)_3^{+} + H^+$$

The obtained parameters were used as a boundary parameter to fit the $\log_{10}K°$ value for the carbonate-containing ternary surface complex to respective sorption data.[8]

$$2 \equiv FeOH + UO_2^{2+} + CO_3^{2-} + H_2O \leftrightarrow (\equiv FeO)_2{-}UO_2(CO_3)(OH)^{3-}$$

Tab. 1: Parameter for the surface complexation modelling of U(VI) onto magnetite.

DDL model parameter	value
Site density (nm^{-2})	14.20*
$pK°_{a1}$	5.10
$pK°_{a2}$	9.12
$\log_{10}K°$ [$(\equiv FeO)_2H{-}UO_2(H_2O)_3^{+}$]	0.67
$\log_{10}K°$ [$(\equiv FeO)_2{-}UO_2(CO_3)(OH)^{3-}$]	−0.84

*[6].

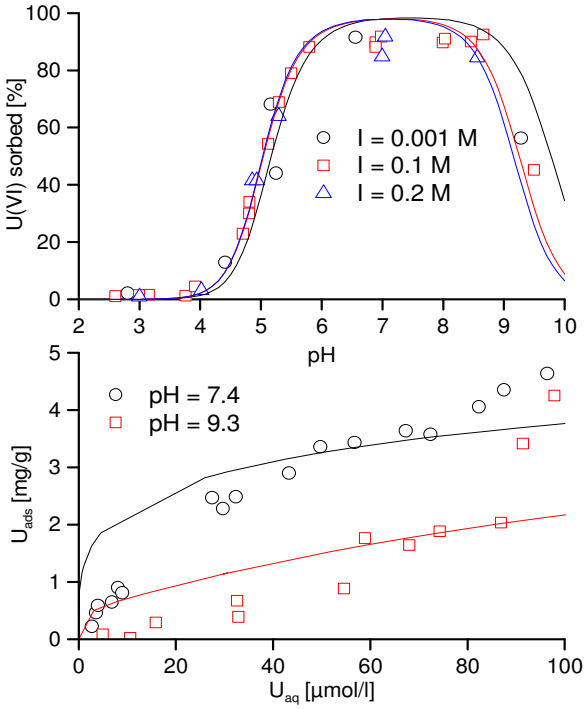

Fig. 1: Fitting results for the sorption of U(VI) onto magnetite in carbonate-free (top) and carbonate-containing system (bottom). Experimental points were taken from literature.[1, 8]

RESULTS. The model parameters are listed in Tab. 1. The best fitting results were obtained using a bidentate-bound, unhydrolyzed U(VI) surface complex where only one of the two surface groups became deprotonated as recently suggested[9] in combination with a bidentate-bound ternary U(VI) surface complex containing one carbonate and one hydroxide ion attached to the radionuclide.

CONCLUSIONS. The sorption of U(VI) onto magnetite can be modelled using only two surface complexes representing a realistic surface chemistry. In combination with PSI/Nagra Chemical Thermodynamic Database 12/7, this robust model can be extrapolated over a wider range of environmental conditions.

[1] Missana,T. *et al.* (2003) *Geochim. Cosmochim. Acta* **67**, 2543–2550.
[2] Mitchell M. (2014) Engauge Digitizer, https://github.com/markummitchell/engauge-digitizer (2016-12-01)
[3] Parkhurst, D. L. *et al.* (2013) *U.S. Geological Survey Techniques and Methods, Vol. book 6-A43*, p. 497.
[4] Poeter, E. P. *et al.* (2005) *U.S. Geological Survey Techniques and Methods, Vol. book 6-A11*, p. 283.
[5] Thoenen, T. *et al.* (2014) *PSI Report No. 14-04*, p. 445.
[6] Sahai, N. (1997) *Geochim. Cosmochim. Acta* **61**, 2801–2826.
[7] Sherman D. M. *et al.* (2008) *Geochim. Cosmochim. Acta* **72**, 298–310.
[8] Sagert, N. H. *et al.* (1989) *J. Colloid Interface Sci.* **130**, 283–287.
[9] Geckeis, H. *et al.* (2013) *Chem. Rev.* **113**, 1016–1062.

Quantitative uranium speciation with U $M_{4,5}$-edge HERFD absorption spectra

K. O. Kvashnina, A. Rossberg

This report gives a brief description of the quantitative uranium speciation performed by iterative transformation factor analysis (ITFA) of High Energy Resolution X-ray Fluorescence Detection (HERFD) data collected at the $M_{4,5}$ edge.

The HERFD method allows recording X-ray absorption spectra with substantially better energy resolution and permits the identification of the oxidation states and number of the 5*f* electrons of actinide systems. Moreover, the advances in factor analysis has made it possible to estimate the exact contribution of the different chemical states in the actinide system by ITFA program, where the exact composition can be found without the input of the solely separated compounds.[1, 2]

We show here an example of the speciation studies of the magnetite nanoparticles co-precipitated with U(VI) solution.[3] We used ITFA in order to decompose the spectral mixtures into the spectra and the fractions of the components (Fig. 1). It is clearly indicated in Fig. 1B that only the first three eigenvectors show a signal, while the following (4–6) consist of counting noise (ordinate) and noise in the monochromaticity; hence, only three components are necessary to describe the variation in the spectral mixtures. In the beginning, it was considered that the UO_2 sample contains 100 % of the U(IV) state, and UO_3 contains 100 % of the U(VI) state. The initial analysis showed that the Umh sample contains 100 % of the U(VI) and we used the spectrum of the Umh sample as input of the 100 % of the U(VI) fraction. The iterative target test (ITT) procedure was used to extract the spectrum of the third component and to determine the relative concentrations of all three components.[4] Figure 1C shows the spectra of the separated compounds corresponding to the U(IV), U(V) and U(VI) oxidation states. The analysis shows that all the samples Um1, Um3, Um6 and Um10 contain various fractions of the U(IV), U(V) and U(VI) valence states, being present simultaneously in the same sample. The results are summarized in Tab. 1. Such a quantitative empirical analysis can be applied to any spectrum measured at the actinide $M_{4,5}$ edges.

Tab. 1: Fractions of U(IV), U(V) and U(VI) valence states in the Um1, Um3, Um6 and Um10 samples (values are given in %).

Sample	U(IV)	U(V)	U(VI)
Um1	20	80	0
Um3	0	80	20
Um6	0	72	28
Um10	1	62	37

[1] Rossberg, A. *et al.* (2003) *Anal. Bioanal. Chem.* **376**, 631–638.
[2] Rossberg, A. *et al.* (2009) *Environ. Sci. Technol.* **43**, 1400–1406.
[3] Pidchenko, I. *et al.* (2017) *Environ. Sci. Technol.,* accepted.
[4] Bryden, T. H. *et al.* (1988) *Anal. Chem.* **60**, 1154–1158.

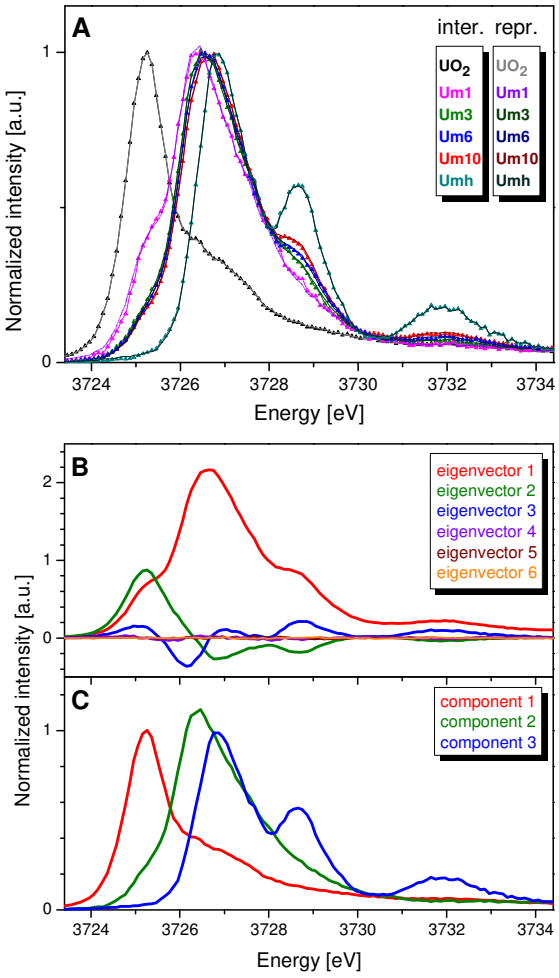

Fig. 1: Interpolated experimental (triangles) and reproduced (solid lines) U M_4 HERFD spectra of the samples containing 1,000 ppm U (Um1), 3,000 ppm U (Um3), 6,000 ppm U (Um6) and 10,000 ppm U (Um10) formed by co-precipitation of the U with magnetite (Fe_3O_4) nanoparticles and compared to the UO_2 and 3,000 ppm U(VI) adsorbed onto γ-Fe_2O_3 (Umh) serving as reference compounds (A). ITFA-extracted eigenvectors (B); isolated single component spectra belong to the U(IV), U(V) and U(VI) contributions (C).

Redox reactions of Tc^{VII} with magnetite and mackinawite: solving an old enigma

E. Yalcintas,[1] A. C. Scheinost, X. Gaona,[1] M. Altmaier[1]

[1]Institute for Nuclear Waste Disposal, Karlsruhe Institute of Technology, Karlsruhe, Germany

While the reduction of heptavalent technetium, Tc(VII), by magnetite and mackinawite under anoxic conditions is well known, the identification of the resulting Tc(IV) species shows substantial disagreement between different studies. Here we use a systematic variation of initial Tc concentration, loading and pH to decipher the Tc species by EXAFS spectroscopy and to shine light on their formation pathways.[1]

Tc in its heptavalent oxidation state is highly mobile due to the high solubility and negative charge of its pertechnetate anion (TcO_4^-). Under the anoxic conditions of nuclear waste repositories as well as in marine sediments, it is easily reduced by Fe(II)-bearing minerals like magnetite and mackinawite. Previous research showed formation of a range of sparingly soluble Tc(IV) species like TcO_2-like and TcS_x-like polymers with or without additional Fe, which may also be attached to the reducing Fe phases, or their incorporation into Fe minerals due to the similar ionic radii of Tc(IV) and Fe(II) or Fe(III).[2–4] To elucidate formation of this variety of Tc species, we systematically varied initial Tc concentration, loading and pH (Tab. 1) and determined the Tc speciation with Tc K-edge XAFS spectroscopy at ROBL.

Tab. 1: Experimental conditions (background electrolyte: 0.1 M NaCl).

Sample	$[TcO_4^-]$ (M)	S/L (g/L)	Loading (ppm)	pH_m	E_h (mV)	$[Tc]_{final}$ (M)
Mag-0	2×10^{-5}	5	400	6.00	−120	$\leq 1\times10^{-8}$
Mag-1	2×10^{-4}	50	400	9.28	−149	$\leq 4\times10^{-10}$
Mag-2	2×10^{-4}	33	600	9.16	−146	$\leq 4\times10^{-10}$
Mag-3	2×10^{-4}	22	900	9.08	−139	$\leq 4\times10^{-10}$
Mag-4	2×10^{-5}	5	400	9.12	−138	$\leq 4\times10^{-10}$
Mag-5	2×10^{-5}	3	600	8.90	−121	$\leq 4\times10^{-10}$
Mag-6	2×10^{-5}	2	900	8.68	−109	$\leq 4\times10^{-10}$
Mack-1	2×10^{-4}	50	400	9.07	−315	$\leq 4\times10^{-10}$
Mack-2	2×10^{-4}	33	600	9.16	−381	$\leq 4\times10^{-10}$
Mack-3	2×10^{-4}	22	900	8.99	−309	$\leq 4\times10^{-10}$
Mack-4	2×10^{-5}	5	400	9.02	−289	$\leq 4\times10^{-10}$
Mack-5	2×10^{-5}	3	600	8.91	−280	$\leq 4\times10^{-10}$
Mack-6	2×10^{-5}	2	900	8.83	−271	$\leq 4\times10^{-10}$

In the presence of magnetite (Fig. 1), we identified two different spectral components, Tc substituting for Fe in the magnetite structure and Tc–Tc dimers sorbed to the magnetite {111} faces through a triple bond (Fig. 3). The sorption endmember is favored at higher [Tc], whereas incorporation prevails at low [Tc] and less alkaline pH conditions. The key role of pH in the uptake mechanism is interpreted in terms of magnetite solubility, with higher [Fe] and greater recrystallization rates occurring at lower pH values.

In the presence of mackinawite, a TcS_x-like phase is predominant under all investigated conditions, although the contribution of up to 20 % of $TcO_2 \cdot xH_2O$(s) (likely as surface precipitate) is observed for the highest investigated loadings (900 ppm), emphasizing the role of (surface) concentration.

These results provide key inputs for an accurate mechanistic interpretation of the Tc uptake by magnetite and mackinawite, controversially discussed in literature, and represent a highly relevant contribution to the investigation of Tc retention processes in the context of nuclear waste disposal.

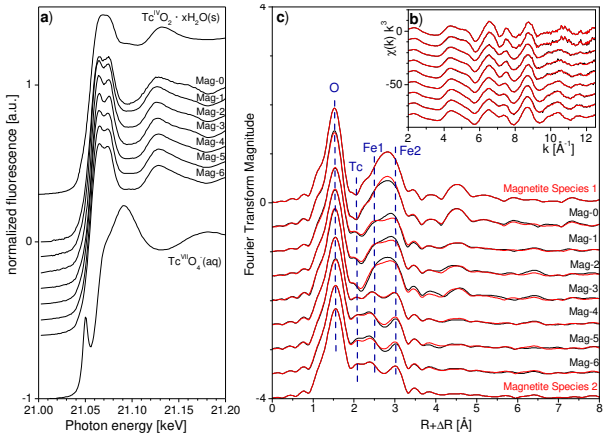

Fig. 1: Tc-K edge XAS spectra of Tc sorbed on magnetite. a) XANES, b) k^3-weighted EXAFS spectra, c) corresponding Fourier Transform Magnitude (FTM). Black lines represent the experimental data, the red lines in b) and c) represent their reconstruction with two principal components. The ITFA-derived FTM spectra of the two endmembers are plotted on top and bottom.

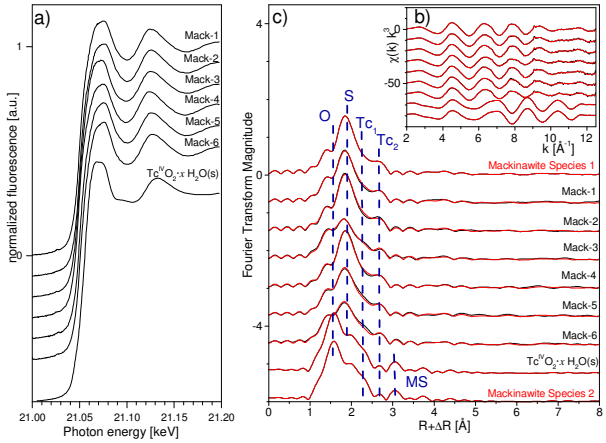

Fig. 2: Tc-K edge XAS spectra of Tc sorbed on mackinawite, else as in Fig. 1.

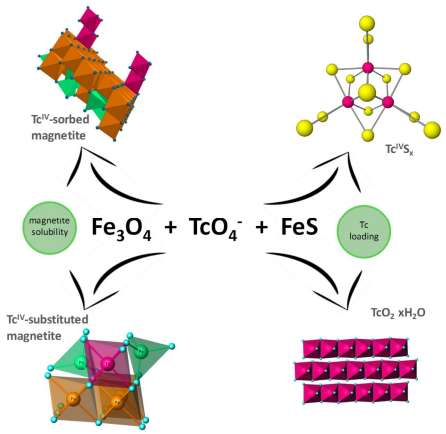

Fig. 3: Schematic formation pathways of Tc^{IV} species in presence of magnetite and mackinawite.

[1] Yalcintas, E. *et al.* (2016) *Dalton Trans.* **45**, 17874–17885.
[2] Peretyazhko, T. S. *et al.* (2012) *Geochim. Cosmochim. Acta* **92**, 48–66.
[3] Marshall T. A. *et al.* (2014) *Environ. Sci. Technol.* **48**, 11853–11862.
[4] Wharton, M. J. *et al.* (2000) *Appl. Geochem.* **15**, 347–354.

Isothermal titration calorimetry of sorption processes: a promising approach

N. Jordan, C. Reder, H. Foerstendorf, B. Drobot,[1] K. Fahmy
[1]Technische Universität Dresden, Dresden, Germany

As a consequence of nuclear waste disintegration heat, elevated temperatures in the near field may influence radionuclide retention significantly. However, there is a nearly complete lack of spectroscopic investigations of sorption processes at elevated temperatures. In addition, experimental data on free Gibbs energy ($\Delta_R G$), enthalpy ($\Delta_R H$) and entropy ($\Delta_R S$) of reactions of most radionuclides including fission products such as ^{79}Se are sparse. Using the Se(IV)/hematite system, we show that microcalorimetry can provide these thermodynamic parameters with high accuracy and in a manner that allows studying various radionuclides.

EXPERIMENTAL. Details about hematite and the performance of batch experiments can be found elsewhere.[1–3] The detection of the heat of the sorption reaction of Se(IV) onto hematite was accomplished by microcalorimetric titrations experiments at 25 °C using a TAM Instrument. A hematite suspension (1.8 mL) was introduced into the titration ampoule and permanently stirred using a gold propeller. After thermal equilibration, 25 successive injections of 10 µL 0.1 mol L^{-1} Se(IV) at pH 5 were performed. All experiments were carried out at 25 °C. Concentration of hematite varied from 1 to 12 g L^{-1} (0.1 mol L^{-1} NaCl, pH 5).

RESULTS. Elevated temperature (up to 60 °C) reduces the sorption of Se(IV) by hematite (Fig. 1) and consequently suggests an exothermic adsorption process.
The heat flow was recorded as a function of time during the titrations. The obtained thermogram from a hematite suspension (4 g L^{-1}) is exemplarily shown in Fig. 2. The adsorption process was found to be exothermic, in agreement with findings of batch experiments. As the number of injections increases, the signal continuously decreases. Indeed, during the course of injections, the binding sites of hematite are being gradually saturated by Se(IV), and the exothermic effect gets consequently reduced. After the twentieth injection (Fig. 2), i.e. in saturation, the signal remains constant and reflects only the heat of dilution.
The heat (in J) related to each injection can be derived from single peak areas. The sum of all injections represents the corresponding enthalpy of the overall reaction ($\Delta_R H$). Assuming that all Se(IV) is adsorbed onto the hematite surface after the first injection (to be checked in more detail), the molar enthalpy of adsorption (J mol^{-1}) can be determined and, thus, the number of adsorbed Se(IV) molecules as well. By applying the Langmuir isotherm and assuming the proportionality of q_m to the mass to volume ratio, the Langmuir constant (log K_L = 4.3) can be derived (Fig. 3).
In the future, spectroscopic techniques evidencing the nature of the adsorption process and the number of relevant species at the surface will be combined with microcalorimetry. Thus, a thermodynamic description of the radionuclide mobility in natural systems will be assessed with much more confidence and lower uncertainties.

ACKNOWLEDGEMENTS. Authors are grateful to Anne Bauer for technical introduction into microcalorimetry.

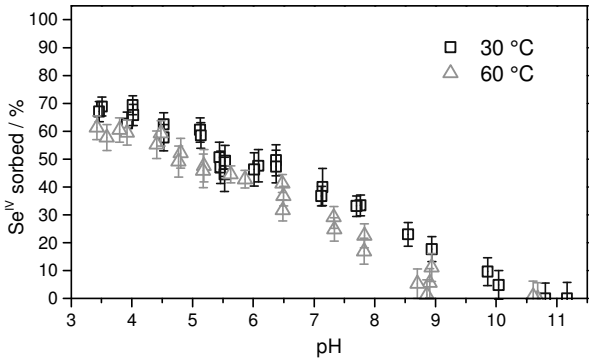

Fig. 1: Selenium(IV) sorption edges onto hematite at different temperatures (NaCl 0.1 mol L^{-1}, $[Se(IV)]_{initial} = 5\times10^{-5}$ mol L^{-1}, m/v = 0.25 g L^{-1}, 2 days of shaking, under N_2).

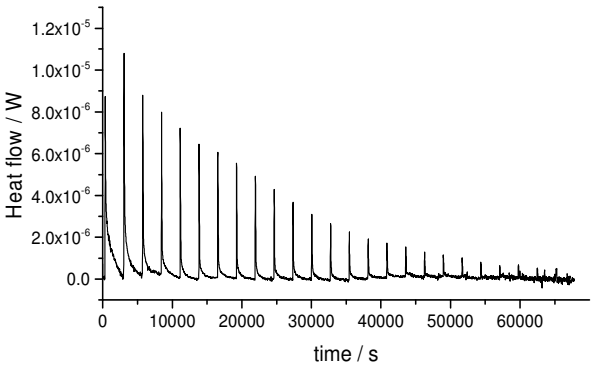

Fig. 2: Power (heat flux)–time curve for the sorption of Se(IV) onto hematite (4 g L^{-1}, $[Se(IV)]_{initial}$ = 0.1 mol L^{-1}, 0.1 mol L^{-1} NaCl, 25 °C).

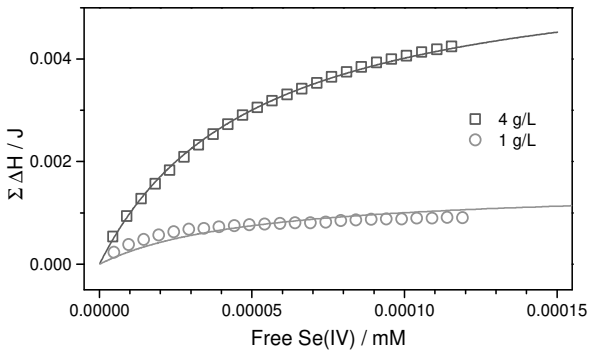

Fig. 3: Cumulative heat of adsorption as a function of the free concentration of Se(IV).

[1] Müller, K. *et al.*, (2015) *Environ. Sci. Technol.* **49**, 2560–2567.
[2] Jordan, N. *et al.* (2013) *Geochim. Cosmochim. Acta* **103**, 63–75.
[3] Jordan, N. *et al.* (2013) *J. Colloid Interface Sci.* **390**, 170–175.

Hard X-ray emission spectroscopy with pink beam

K. O. Kvashnina, A. Rossberg, J. Exner, A. C. Scheinost

Valence-band X-ray emission spectroscopy (XES) with a "pink beam", i. e. a beam with large energy bandwidth produced by a double-multilayer monochromator, is introduced here to overcome the weak count rate of monochromatic beams produced by conventional double-crystal monochromators. Our results demonstrate that – in spite of the large bandwidth in the order of 100 eV – the high spectral resolution of the Johann-type spectrometer is maintained, while the two orders of magnitude higher flux greatly reduces the required counting time. The short working distance Johann-type X-ray emission spectrometer and multilayer monochromator is available at ROBL.

XES is an element-selective method which provides a unique approach to study the electronic structure. The element sensitivity is achieved by creating a core hole with incident X-rays above the X-ray absorption edge. The event, when the core hole is filled by the valence electrons, can be measured by XES. Due to the dipole-allowed selection rules, XES can be used as fingerprint of the partially occupied density of states projected onto a selected atom in hybridization with ligands. Thus, the effects of the crystal structure and hybridization between different atoms and their electronic states can be studied by XES.[1, 2]

EXPERIMENTAL. Measurements of the non-resonant $K\beta_{1,3}$ XES lines of the transition metals are commonly fast even with monochromatic beam, but the valence band $K\beta_{2,5}$ XES lines are very weak (Fig. 1), hence, require very long counting times. In order to overcome this limitation related to the weak count rate, we used a double-reflection multilayer monochromator at ROBL. Multilayer optics operate at a typical incident angles of a few degrees with a bandwidth about 100 times larger than that of the conventional double-crystal optics. At the same time, the multilayer optics provides a significant flux increase, which is commonly used for methods such as X-ray imaging or fluorescence spectroscopy, where the narrow bandwidth of the crystal optics is not required. We show here that combination of the multilayer optics with X-ray emission spectrometer gives the possibility to probe the valence band excitations of the matter near the Fermi level in a relatively short time while maintaining a high energy resolution.

RESULTS. Figure 1 compares the $K\beta_{2,5}$ XES lines of ZnO recorded with either the Si(111) double-crystal (red) or the double multilayer (blue) monochromator. A 0.5-m bending-radius Johann-type X-ray emission spectrometer is used for both measurements.[3] Under these conditions, we gained a factor of 25 in the data collection rate with multilayers compared to crystals. The time spent on the $K\beta_{2,5}$ XES data collection with multilayer optics is 15 minutes (blue curve, Fig. 1), which compares to 1.5 hours with the Si(111) crystals (red curve, Fig. 1).
Therefore, the spectrometer equipped with a 0.5-m crystal analyzer in combination with the pink beam improves the signal's intensity by a factor > 100 in comparison to the 1-m spectrometer in combination with a monochromatic beam. The proposed method is broadly applicable to time-resolved X-ray emission analysis at different generations of synchrotron facilities and X-ray free-electron laser light sources.

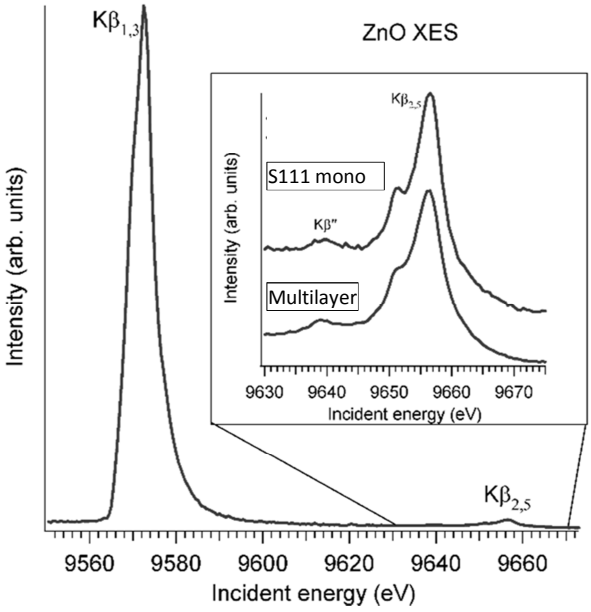

Fig. 1: Experimental $K\beta_{1,3}$ and $K\beta_{2,5}$ emission lines of ZnO recorded with a pair of Si(111) crystals and the 1-m spectrometer (red), and with a pair of multilayer s and the 0.5 m spectrometer (blue).

[1] Kowalska, J. K. (2016) *Inorg. Chem.* **55**, 4485–4497.
[2] March, A. M. (2015) *J. Phys. Chem. C* **119**, 14571–14578.
[3] Kvashnina, K. O. *et al.* (2016) *J. Synch. Radiat.* **23**, 836–841.

Sorption competition of trivalent metals on corundum (α-Al_2O_3) studied on the macro- and microscopic scale

S. Virtanen,[1] M. Eibl, S. Meriläinen,[1] A. Rossberg, J. Lehto,[1] T. Rabung,[2] N. Huittinen

[1]University of Helsinki, Helsinki, Finland; [2]Karlsruhe Institute of Technology, Karlsruhe, Germany

In this study we investigated the potential competitive influence of Y^{3+} on the uptake of trivalent lanthanides and actinides on corundum (α-Al_2O_3). Both batch sorption and time-resolved laser fluorescence spectroscopic (TRLFS) data showed a decreased uptake of Eu^{3+} or Cm^{3+}, respectively, in the presence of Y^{3+}, pointing toward sorption competition between the trivalent ions. A change in the actinide speciation on the corundum surface could be observed in the presence of Y^{3+}. In extended X-ray absorption fine structure (EXAFS) investigations, the speciation change could be attributed to a systematic transition from a tetradentate Am^{3+} surface complex to a tridentate one, when increasing the total metal ion concentration on the mineral surface.

The uptake of metals by solid surfaces is often investigated in single element studies, thus, not accounting for potential effects of sorption competition in the presence of multiple dissolved elements or compounds. It has been shown that metal cations with similar chemical properties (such as tendency toward hydrolysis or oxidation state) influence the uptake of one another on solid surfaces, implying that the retention of metal cations may be overestimated when considering only one element at a time.[1, 2] Thus, sorption competition reactions and potential changes in the metal ion speciation in the presence of multiple solutes should be accounted for when describing the fate of contaminants in the environment. In this study, we have investigated the potential competitive influence of Y^{3+} on the uptake of trivalent lanthanides and actinides on corundum combined batch sorption (Eu^{3+}), TRLFS (Cm^{3+}), and EXAFS (Am^{3+}) investigations.

RESULTS. The batch sorption experiments show that the uptake of Eu^{3+} on the mineral surface decreases with increasing Y^{3+} concentration, pointing toward competition between the trivalent elements. The same results are obtained in TRLFS investigations where Cm^{3+} remains in solution at much higher pH values in the presence than in the absence of Y^{3+} (Fig. 1). In addition, the speciation of the actinide changes in the alkaline region when Y^{3+} is present, as seen by the red-shift of the emission spectra (Fig. 1, bottom, right). In order to explain the speciation change observed in the laser spectroscopic investigations, EXAFS studies were conducted for Am^{3+} in the presence and absence of Y^{3+}. By varying the Am and Y concentrations in the corundum samples a total metal ion concentration between 6×10^{-6} M and 2.2×10^{-4} M was achieved. The fitted EXAFS data clearly show that the overall coordination number of Am^{3+} decreases from approximately 9 to 8 with increasing metal ion loading leading to a contraction of the Am–O distance (Fig. 2, top). For the Am–Al scattering shell the CN is seen to decrease from approximately 3 to 2, while the distance to the surface gets slightly longer (Fig. 2, bottom).

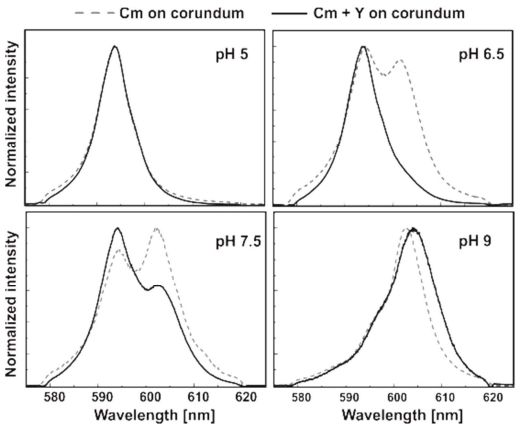

Fig. 1: Comparison of luminescence emission spectra of 10^{-7} M Cm^{3+} on 0.5 g/L corundum in the absence (grey, dashed lines) and presence of 10^{-4} M Y^{3+} (black lines).

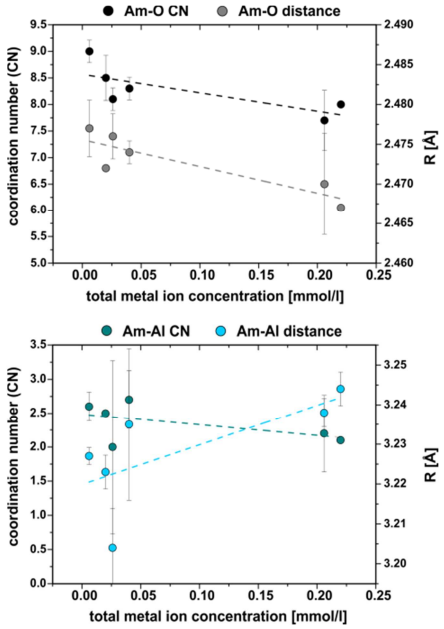

Fig. 2: Obtained coordination numbers (CN) and distances (R) for Am-O (top) and Am-Al (bottom) scattering shells in the EXAFS investigations on Am^{3+} uptake by corundum in the presence and absence of Y^{3+}.

Based on the changes in the CNs and recorded luminescence lifetimes in the Cm^{3+}-TRLFS investigations, the attachment of the actinides on the corundum surface could be assigned. The luminescence lifetimes indicate the presence of 5 H_2O molecules in the first coordination sphere of the actinide ion over the whole investigated pH- and metal-ion concentration range. Thus, for an overall coordination number of 9 at lower metal ion loadings, tetradentate coordination to the surface must occur on a site connected to three aluminum atoms. With increasing metal ion concentration the overall CN decreases to 8, implying that a complex with tridentate coordination to the surface becomes prevailing.

Our results have clearly shown that the presence of cations with similar chemistries will influence the uptake properties of one another on solid surfaces. In addition, a speciation change may be accompanied by the presence of competing ions on the mineral surface if the overall concentration is high enough.

[1] Bradbury, M. H. *et al.* (2005) *Geochim. Cosmochim. Acta*, **69**, 4187–4197.

[2] Trivedi, P. *et al.* (2001) *Colloids Surf. A* **191**, 107–121.

Incorporation of Eu(III) into calcite under recrystallization conditions

S. E. Hellebrandt, S. Hofmann, N. Jordan, A. Barkleit, M. Schmidt

The interaction of three calcite powders with Eu(III) under recrystallization conditions was studied on the molecular level using site-selective time-resolved laser fluorescence spectroscopy (TRLFS). Batch contact studies with reaction times from 1 week up to 3 years revealed that the speciation differs from that observed previously in co-precipitation experiments and is dominated by a newly identified species „γ". The speed of formation of this species was found to depend greatly on the recrystallization rate of the studied minerals.[1]

Calcite is present in clay rock formations as well as the major degradation product of cementitious materials. Consequently, calcite may play a significant role as a retention barrier for the transport of contaminants in the environment. Its performance as such a barrier will depend on the specific conditions of this interaction.[2]

EXPERIMENTAL. Three calcite powders (C1–3) were chosen for this study. C1 and C3 were obtained as powders from Merck and Solvay. C2 was obtained from Ward's Science, U.S.A., as a single crystal and ground to a grain size < 63 µm. All solids were characterized by powder XRD, BET, and SEM. The specific surface area of the powders was found to be 0.6 ± 0.1, 1.1 ± 0.1 and 18.0 ± 0.1 m²/g for calcite C1, C2 and C3, respectively.[1]

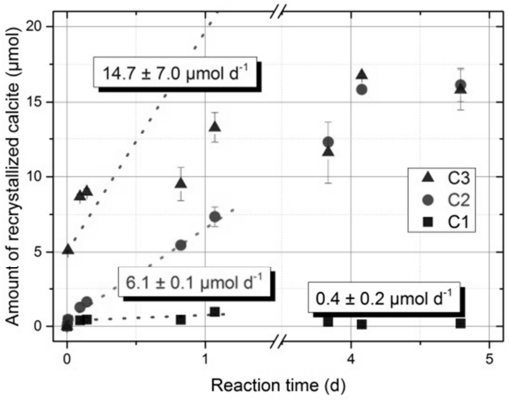

Fig. 1: Amount of recrystallized calcite (µmol) (■) C1, (●) C2 and (▲) C3 (m/v = 2.5 g/L, 0.01 mol/L NaCl) as a function of time.

RESULTS. The exchange rate of calcium ions between the solid and liquid phase was determined by tracer experiments using ^{45}Ca (Fig. 1). It is commonly assumed that the kinetics of this exchange is directly linked to the recrystallization rate and, therefore, the reactivity of calcite.[3]
Three stages of recrystallization kinetics can be identified. The highest rate is observed within the first hours of the reaction, followed by a decrease of the rate and eventually equilibrium. Both calcites C2 and C3 exhibit significantly higher rates compared to C1, which does not reach equilibrium within the reaction time.
We used site-selective TRLFS to identify Eu(III) species in each of the three calcite materials at various stages of the reaction (Fig. 2). In total, four species named α–δ were identified. Each species was subsequently characterized by their emission spectra and fluorescence lifetimes (Tab. 1).
The main product of the incorporation reaction is none of the species A, B, or C that were previously identified in co-precipitation experiments,[4] but instead the new species γ

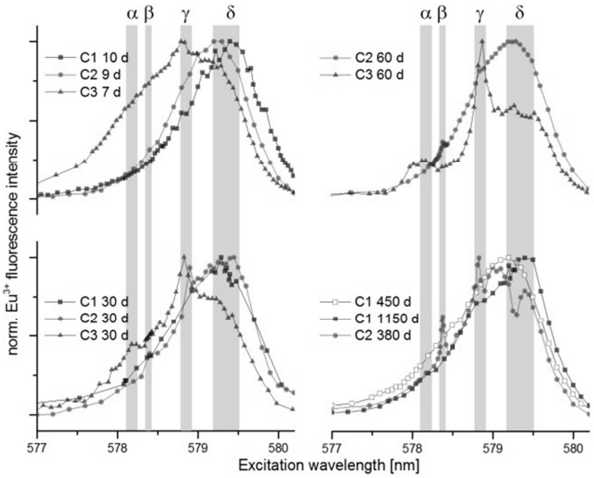

Fig. 2: $^7F_0 \rightarrow {}^5D_0$ Excitation spectra after 7 days (C1–C3), 30 days (C1–C3), 60 days (C2 and C3) and after longer reaction times (C1 450 and 1150 days; C2 380 days).

was identified. The site occupied by species γ is of low symmetry (as all other species) and bears little resemblance to the trigonal Ca site. The newly identified incorporation mechanism must then either induce a significantly stronger distortion in the crystal's lattice, or Eu occupies a non-crystallographic site. One could speculate that the structural control of a local disturbance in the lattice is stronger in the slow process close to equilibrium than in the faster reaction upon mineral growth. During growth of calcite, cations would be expected to adsorb in crystallographic locations, while in case of recrystallization the initial sorption reaction may be more likely at surface defects.

Tab. 1: Characteristics of the observed species.

	α	β	γ	δ
$\lambda_{exc.}$ (nm)	578.2	578.4	578.8	579.4
τ (µs)	3700 ± 350	2450 ± 150	3750 ± 450	700 ± 50
n(H_2O)	0.0	0.0	0.0	0.9

We observed two other incorporation species, α and β. Species β has been observed in previous co-precipitation experiments as species B.[4] Species α was hitherto unknown and is always a minor species. It remains unclear what the mechanism of formation of these minor species is, and whether they are transitory species. Species β only occurs after species γ, and γ is not significantly reduced where it occurs, so the two species must form independently.
Our findings conclusively show that Eu(III) is incorporated into calcite under recrystallization conditions. The observed speciation is different from that found in co-precipitation experiments and will depend on calcite's recrystallization rate or reaction kinetics. Eventually, species γ becomes predominant independent of the time required to reach this point. This means that calcite will act differently as a retention barrier, e. g. on a nuclear waste disposal site, depending on whether it is present as a component of the host rock formation and, thus, close to thermodynamic equilibrium or formed later on as a secondary phase.

[1] Hellebrandt, S. E. *et al.* (2016) *Sci. Rep.* **6**, 33137.
[2] Stumpf, T. *et al.* (2002) *J. Colloid Interface Sci.* **249**, 119–122.
[3] Berner, U. *et al.* (1983) *Am. J. Sci.* **283**, 641–683.
[4] Schmidt, M. *et al.* (2008) *Angew. Chem. Int. Ed.* **47**, 5846–5850.

Complexation of Eu(III) with a polymeric cement additive as a potential carrier of actinides

H. Lippold, M. Becker

In the long term, cementitious materials in a final repository will be exposed to leaching processes generating highly alkaline solutions. Polymeric additives, so-called superplasticizers, are considered as potential mobilizing agents for released radionuclides, since it is uncertain whether complete degradation will take place under the evolving aqueous conditions. Regarding the complexing properties of superplasticizers, there are only indirect assessments so far. In this study, first systematic investigations on complexation with Eu(III) as an analogue of trivalent actinides were performed at variable pH and electrolyte content ($NaCl$, $CaCl_2$) using ultrafiltration as a separation method. A stability constant was derived according to the charge neutralization model. For this purpose, the proton exchange capacity was determined by potentiometric titration.

EXPERIMENTAL. A commercial superplasticizer "MasterGlenium® 51", consisting of polycarboxylate ethers (PCE) as a 35 % aqueous solution, was obtained from BASF. Direct titration was carried out with 0.1 N NaOH in 0.1 M $NaClO_4$ under a N_2 atmosphere following the procedure proposed by Young *et al.*[1] Complexation with Eu(III) was investigated using ^{152}Eu as a radiotracer. After equilibration for 24 h, bound Eu fractions were determined *via* ultrafiltration with Sartorius "Vivaspin 2" polyethersulfone centrifuge filters (MWCO: 3 kDa) at 6,000 rpm. Retention was 97 % for PCE and 1 % for Eu at pH 6.

RESULTS. Different from other acidic polyelectrolyte systems, such as humic substances, the PCE mixture under study shows a sharp equivalence point on titration (Fig. 1), which indicates a comparatively low dispersity, that is a narrow molecular weight distribution. The content of carboxyl groups (proton exchange capacity) was determined to be 1.17 meq g^{-1}.

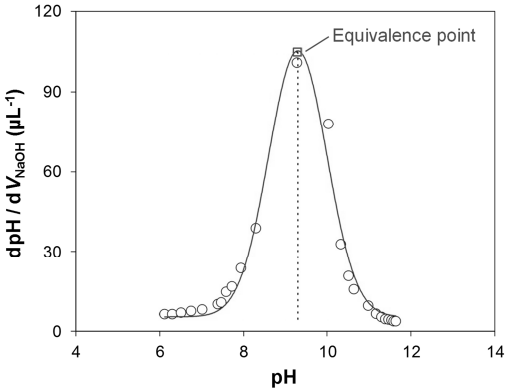

Fig. 1: Titration curve for PCE (30.5 mg, V_{eq} = 358 µL 0.1 N NaOH). Solid line: Gaussian fit.

These carboxyl groups are potentially strong complexing ligands for multivalent metals. Figure 2 shows a binding isotherm for Eu(III) at ambient pH. Saturation is nearly reached at the highest Eu concentration, allowing a determination of complexation parameters according to the charge neutralization model,[2] which corresponds to the Langmuir equation with an equilibrium constant normalized to ion

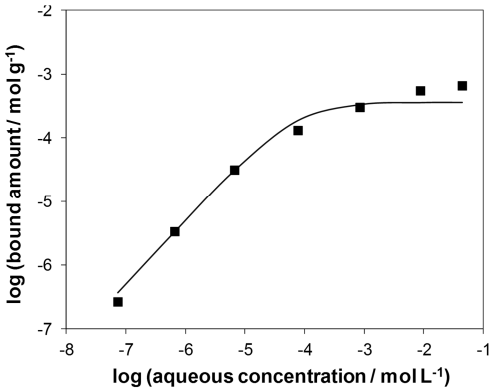

Fig. 2: Isotherm of binding of Eu(III) to PCE (pH 6). Line: Langmuir fit.

charge (stability constant β) and a maximum load normalized to proton exchange capacity and ion charge (loading capacity, LC). Fitting the Langmuir equation yielded a log (β/L mol^{-1}) of 4.6 and an LC of 92 % comparable to values obtained for humic substances, which are known to control the mobility of actinides in far-field scenarios.[3] At pH 12, which is encountered in cementitious systems, Eu is completely bound to PCE, as it can be seen in Fig. 3. This high degree of interaction is not decreased even in the presence of 4 M NaCl. In contrast, complexation decreases from 100 % to 5 % on addition of 0.7 M to 4 M $CaCl_2$ (corresponding to ionic strengths of 2.1 M to 12 M). The electrolyte effects are much stronger at pH 6. The re-rise of bound amounts at high ionic strengths is possibly a consequence of decreasing activity coefficients.

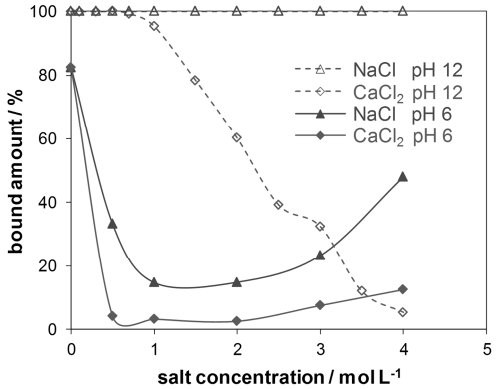

Fig. 3: Effects of pH and electrolytes on binding of Eu(III) to PCE (10^{-6} M Eu, 100 mg L^{-1} PCE).

The strong complexing ability of PCE is evident. In order to evaluate their mobilizing potential, adsorption on cement phases, buffer materials and host rock must be likewise investigated as a function of pH and electrolyte content. Furthermore, detailed studies on leaching and degradation are indispensable.

ACKNOWLEDGEMENTS. This work was funded by the German Federal Ministry for Economic Affairs and Energy (BMWi), support code 02 E 11415B.

[1] Young, S. D. *et al.* (1981) *J. Soil Sci.* **32**, 579–592.
[2] Kim, J. I. *et al.* (1996) *Radiochim. Acta* **73**, 5–10.
[3] Choppin, G. R. (1992) *Radiochim. Acta* **58/59**, 113–120.

Site-selective fluorescence spectroscopy investigations of $LnPO_4$ xenotime ceramics for radioactive waste disposal

H. Lösch, A. Hirsch,[1] J. Holthausen,[2] L. Peters,[1] S. Neumeier,[2] N. Huittinen
[1]Institute of Crystallography, RWTH Aachen University, Aachen, Germany; [2]Forschungszentrum Jülich, Jülich, Germany

Europium incorporation in different $LnPO_4$ (Ln = Tb, Lu and $Gd_{1-x}Lu_x$) phases crystallizing in the xenotime structure was investigated with site-selective TRLFS, PXRD and Rietveld analyses. Based on recorded emission spectra and diffraction patterns, the formation of three different crystal systems (xenotime, anhydrite, and monazite) could be identified. Aging of the ceramic samples and a second sintering step led to an accumulation of europium in the grain boundaries and on the surface.

EXPERIMENTAL. The synthesis of the Eu^{3+}-doped $LnPO_4$ samples was done according to a hydrothermal route described by Roncal-Herrero.[1] Subsequent to the synthesis, site-selective TRLFS studies were conducted to investigate the incorporation of Eu^{3+} within the ceramic structure. A re-characterization of the samples using TRLFS and PXRD was performed after one year of storage under ambient conditions (25 °C, air, normal pressure). The TRLFS and PXRD analyses were followed by a second sintering step to investigate the behavior and re-distribution of the dopant within the solid matrix. This sintering step of the xenotime phases was performed at 1250 °C for 15 h. The PXRD investigation was performed on a Phillips X´Pert Pro diffractometer using a θ−θ geometry, CuK_α radiation in the range 10−80° and a step size of 0.008°. The site-selective TRLFS investigations ($^7F_0 \rightarrow {}^5D_0$) were performed with a pulsed Nd:YAG pumped dye laser set-up.

RESULTS. The diffraction pattern of Eu^{3+} doped $TbPO_4$ indicated the formation of two different phases (Fig. 1). The major phase (87 wt-%) could be identified as a $TbPO_4$ in an uncommon and unexpected anhydrite-like phase with an orthorhombic structure. The minor phase (13 wt-%) belonged to the expected xenotime structure. The second sintering caused an increase of the xenotime phase to 39 wt-%. The excitation spectra of the Eu^{3+}-doped $TbPO_4$ directly after the synthesis and after one year storage showed only on narrow signal corresponding to one Eu-species. Based on the splitting pattern of the recorded emission spectra, this species could be assigned to Eu^{3+} incorporation in the anhydrite structure. After the second sintering a minor phase was identified in the TRLFS investigations, corresponding to Eu^{3+} incorporation in monazite.

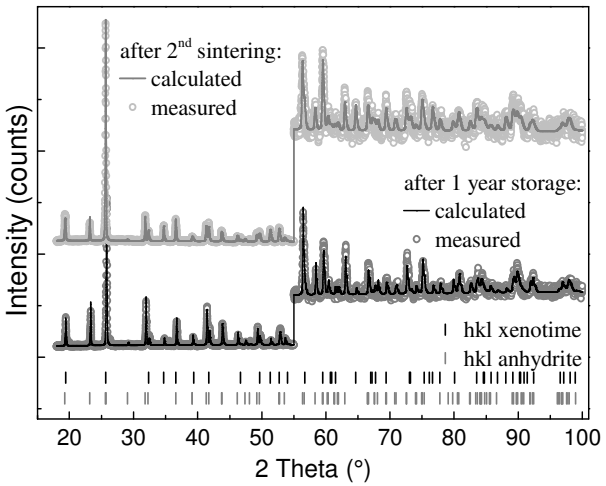

Fig. 1: PXRD patterns of Eu^{3+}-doped $TbPO_4$ after one year storage and a second sintering.

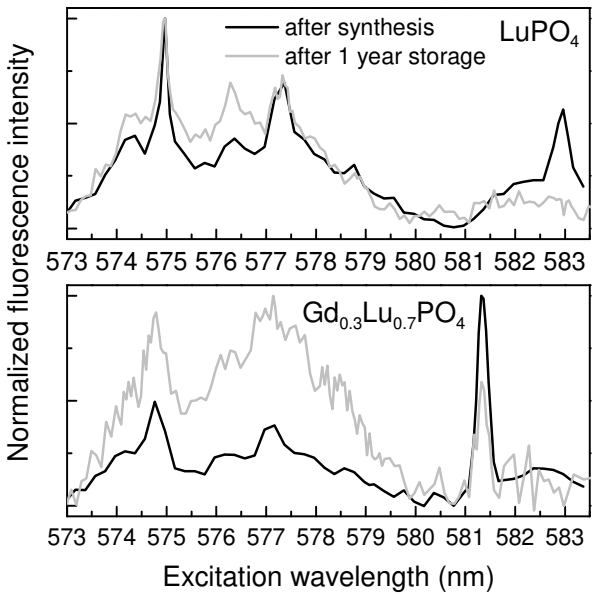

Fig. 2: Excitation spectra of $LuPO_4$ (above) and $Gd_{0.3}Lu_{0.7}PO_4$ (below) after the synthesis and after one year storage in the lab under ambient condition.

In the diffraction patterns of $LuPO_4$ and $Gd_{1-x}Lu_xPO_4$ (x = 0.7, 0.5), only reflexes of a xenotime phase were observed. After the synthesis, the excitation spectra of $LuPO_4$ and the $Gd_{1-x}Lu_xPO_4$ solid solutions showed peaks at 583.0 and ~581 nm, respectively, corresponding to incorporated Eu^{3+} in the xenotime structure (Fig. 2). In addition, two minor signals in the blue shifted area around 575 and 577 nm were observed. These signals could be explained by the accumulation of europium in the grain boundaries and on the grain surfaces.[2] After one year of storage, the signal at 583.0 nm ($LuPO_4$) completely vanished, while for the solid solutions, a significantly decreased intensity of the signal at 581.0 nm ($Gd_{1-x}Lu_xPO_4$) was observed pointing toward partitioning of Eu^{3+} from the crystal structures. The analysis of the lifetimes indicated biexponential decay after synthesis as well as after one year storage. The long lifetime suggests a full loss of the Eu^{3+} hydration sphere upon incorporation in the xenotime lattice, as it can be expected after sintering at 1450 °C. The shorter lifetime ranges from 200−850 µs corresponding to 4.5−0.5 water molecules in the first hydration sphere of Eu, which indicates the presence of a partly hydrated Eu^{3+} species as expected for a sorbed surface species or a grain-boundary associated cation.

CONCLUSION. The results of the performed TRLFS and PXRD investigations show the formation of an anhydrite phase instead of the expected xenotime structure. It can also be seen that the storage over one year in the lab leads to a strong change of the crystal structure corresponding to partly accumulation of the Eu^{3+} in the grain boundaries and on the surface.

[1] Roncal-Herrero, T. *et al.* (2011) *Nanopart. Res.* **13**, 4049−4062.
[2] Holliday, K. *et al.* (2013) *Radiochim. Acta* **101**, 267−272.

Formation of Zr(IV)-nanoparticles on Muscovite (001): effect of background electrolyte

C. Qiu, J. E. Stubbs,[1] P. J. Eng,[1] M. Schmidt

[1]Center for Advanced Radiation Sources, University of Chicago, Chicago, IL, U.S.A.

The formation of Zr(IV) oxo-hydroxide nanoparticles on the muscovite (001) surface was investigated as a function of ionic strength (NaCl) using X-ray surface diffraction techniques. The best fit model revealed a structural ordering of Zr nanoparticles that extends up to ~3 nm above substrate surface and increases with NaCl concentrations. We propose a plausible mechanism to explain the Zr nanoparticle aggregation process.

EXPERIMENTAL. Solutions of 0.1 mM Zr(IV) were prepared and adjusted to pH 2.5. Ionic strength was adjusted to 1 mM, 10 mM, or 100 mM using NaCl. Muscovite crystals were cleaved to expose a fresh surface and reacted with each Zr(IV) solution for over 24 hours prior to Crystal Truncation Rod/Resonance Anomalous X-ray Reflectivity measurements, which were performed under *in situ* conditions. All samples were probed by atomic force microscopy (AFM) in parallel for determination of the size and shape of the Zr nanoparticles at different stages.

RESULTS. A hitherto unresolved question in the aqueous chemistry of Zr(IV), as well as other tetravalent cations, such as Pu(IV) and Th(IV), is how the oligo- and polymerization of their hydrolysis products proceeds on a molecular scale.[1] Recent studies show that these reactions are strongly accelerated at mineral interfaces.[2] Muscovite mica is favorable in this context, due to its atomically flat, negatively charged, and chemically unreactive (001) basal plane. Through CTR/RAXR modeling, we derived the electron density of Zr above the muscovite surface (Fig. 1, top), which reveals the internal cation network in the Zr-nanoparticles. Here, we propose a plausible chemical route to depict the Zr nanoparticle aggregation induced by increased concentration of background electrolyte. Without background electrolyte, the observed Zr(IV) species exists as tetramer and/or octamer as primary particles without further aggregation due to strong electrostatic repulsion between them. The addition of NaCl weakens the electrostatic repulsion by formation of a Stern layer around the particles to enable colloidal aggregation that evolves through several stages as confirmed by AFM images (Fig. 1, middle). In combination the two methods show that the pathway of the aggregation begins by connecting two or more primary tetrameric building units "head-to-head" to form rod-shaped structures (nanorod). Afterwards, the "side-by-side" aggregation becomes favored, which leads to the formation of two-dimensional nanosheets. The net positive charge of these nanosheets is accumulated at its edge sites, where the terminal oxygen groups would undergo protonation to be positively charged at low pH. On the other hand, the hydroxo groups (–OH–) bridging adjacent Zr ions are charge-neutralized by one proton and two Zr–O bonds. As a result, "face-to-face" stacking is the final stage of the nanoparticle growth. The face-to-face stacking is favored due to the fact that the electrostatic repulsion force diminishes (or even disappears) when non-charged oxygen groups (bridging hydroxyl groups) are involved in the aggregation (Fig. 1, bottom).

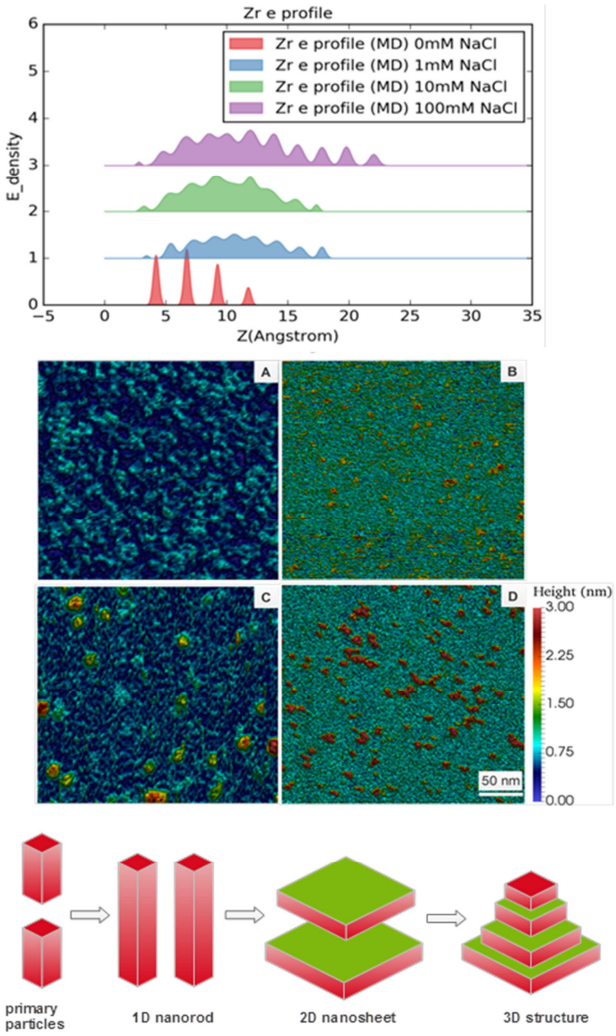

Fig. 1: Zr electron density as a function of NaCl concentrations based on the best fit CTR/RAXR model (top). AFM images for different NaCl concentrations (A to D: 0, 1, 10, 100 mM NaCl) (middle). Schematic diagram of progressive evolution of Zr(IV) nanoparticle aggregation (bottom). Note the surfaces paint in red are positively charged and surfaces paint in green are charge neutral.

ACKNOWLEDGEMENTS. This study is funded by Helmholtz Young Investigator Group "Structures and reactivity at the aqueous/mineral interface" (VH-NG-942).The X-ray data were collected at the GSECARS beamline 13-IDC at the Advanced Photon Source (APS), Argonne National Laboratory (DOE Contract No. DE-AC02-06CH11357) and the Rossendorf Beamline BM20 at the ESRF.

[1] Knope, K. E. *et al.* (2012) *Chem. Rev.* **113**, 944–994.
[2] Schmidt, M. *et al.* (2013) *Environ. Sci. Technol.* **47**, 14178–14184.

Phase composition of yttrium-doped zirconia ceramics

C. Hennig, S. Weiss, A. Ikeda-Ohno, R. Gumeniuk,[1] A. C. Scheinost
[1]Institut für Experimentelle Physik, TU Bergakademie Freiberg, Freiberg, Germany

Ceramic material might be an alternative to borosilicate glass for the immobilization of nuclear waste. The crystallinity of ceramic material increases the corrosion resistance over several magnitudes in relation to amorphous glasses. The stability of such ceramics depend on several parameters, among them the crystal phase composition. A reliable quantitative phase analysis is necessary to correlate the macroscopic material properties with structure parameters. We performed a feasibility study based on yttrium-doped zirconia ceramics as analogue for trivalent actinides to ascertain that the nanosized crystal phases in zirconia ceramics can be reliably determined.

EXPERIMENTAL. Aqueous solutions of 0.1 M $ZrO(NO)_2 \cdot H_2O$ (p.a., Aldrich) and $YCl_3 \cdot 4H_2O$ (p.a., Merck) were mixed and titrated to pH 9 to obtain precipitates of desired molar ratios. The solids were washed and freeze-dried at 60 °C for 24 h. The TGA-DSC measurements were performed with a Jupiter-F5/Netzsch. Powder diffraction measurements were performed on the Huber 6-circle diffractometer at the Rossendorf beamline at 16 keV with a $LaCl_3$:Ce scintillation detector. The samples were heated at 1,000 °C for 24 h and measured under ambient conditions.

RESULTS. TGA-DSC measurement of the ZrO_2 sample with 2.7 mol-% Y is shown in Fig. 1. There is a continuous mass loss of 20 wt-% up to 600 °C and an endothermic peak at 115 °C, which both reveal the dehydration processes of the initial material. A well-pronounced exothermic peak at 451 °C, which is not correlated with a mass loss, indicates the bulk crystallization of ZrO_2. The sample with 11.1 mol-% Y shows a similar exothermic peak at 475 °C.

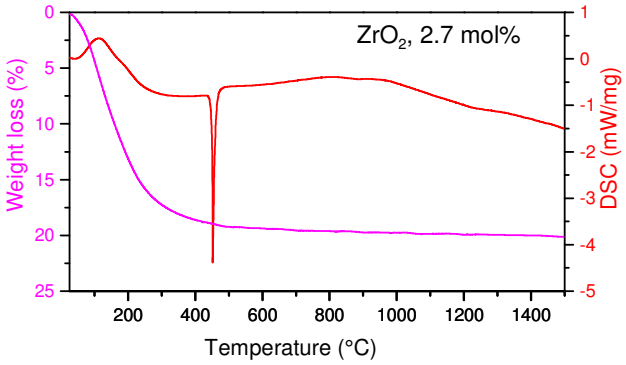

Fig. 1: TGA-weight loss and DSC curves of the ZrO_2 sample with 2.7 mol-% Y, heating rate 20 °C min^{-1}, under synthetic air.

Although these peaks reveal the crystallization process, they are not indicative for the crystalline phase forming.[1] X-ray powder diffraction (XRD) was performed with the aim to identify the phase composition of the ceramic material after thermal treatment. Figure 2 shows the XRD pattern of the ZrO_2 sample with 11.1 mol-% Y. The phase analysis reveals that the ZrO_2 ceramics consist exclusively of the cubic modification (c-ZrO_2), space group $Fm\bar{3}m$. This is in line with the observation in the literature.[2] Without doping ZrO_2 crystallizes in the monoclinic space group $P2_1/c$ (m-ZrO_2). In thermodynamic equilibrium, the ZrO_2/Y_2O_3 system shows the coexistence of c-ZrO_2 and m-ZrO_2 in the range of approximately 1–7 mol-% Y. Differences from that phase

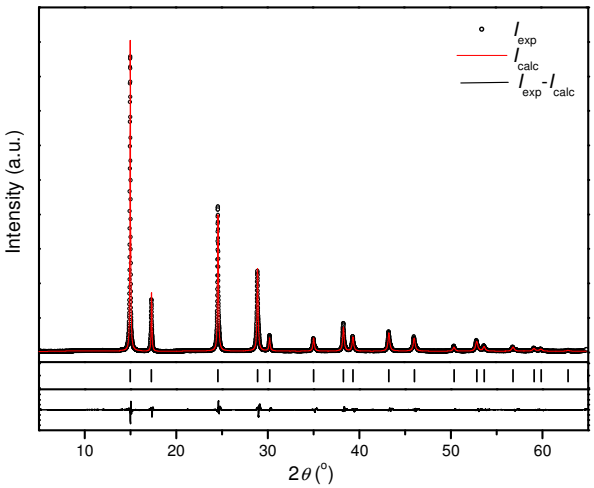

Fig. 2: XRD pattern of the ZrO_2 sample with 11.1 mol-% Y. Experimental intensities are shown as black circles, calculated ones as red lines. The difference is given as black line at the bottom part of the panel. The theoretical peak positions are presented as vertical bars.

composition can appear if the synthesis route follows a sol/gel process with subsequent sintering below the melting point as performed in this study. As an example, the XRD pattern of the ZrO_2 with 2.7 mol-% Y is shown in Fig. 3. The quantitative phase analysis indicates that the ceramics consist partly of the tetragonal phase, t-ZrO_2, with the space group $P4_2/nmc$. The two-phase Rietveld refinement reveals a phase composition of 10.4 wt-% m-ZrO_2 and 89.6 wt-% t-ZrO_2.

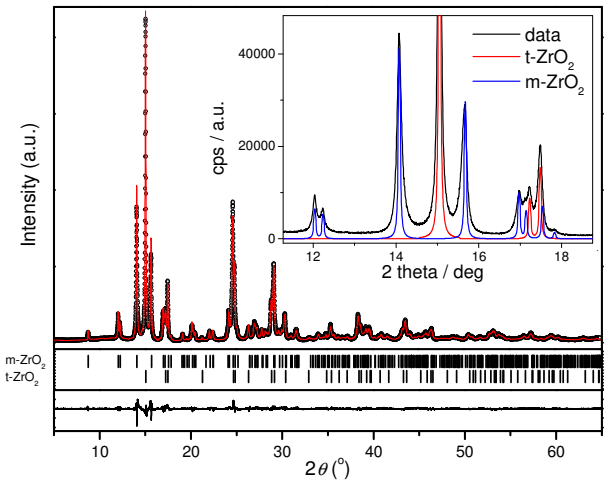

Fig. 3: XRD pattern of the ZrO_2 sample with 2.7 mol-% Y with the same designation as in Fig. 2. The inset shows a selected range of the powder diffraction pattern with the peaks of t-ZrO_2 and m-ZrO_2.

It can be concluded that phase composition of zirconia ceramics can be reliably analyzed. The installation of a Pilatus 2M detector at the Rossendorf beamline in 2017 will significantly enhance the XRD detection sensitivity.

[1] Srinivasan, R. *et al.* (1988) *J. Mater. Res.* **3**, 787–797.
[2] Scott, H. G. (1975) *J. Mater. Sci.* **10**, 1527–1535.

Characterization of the sorption behavior of trivalent actinides on zirconium(IV) oxide

M. Eibl, S. Virtanen,[1] S. Meriläinen,[1] J. Lehto,[1] T. Rabung,[2] N. Huittinen
[1]University of Helsinki, Finland; [2]Institute for Nuclear Waste Disposal, KIT, Karlsruhe, Germany

The uptake of trivalent Eu and Cm on zirconium(IV) oxide was investigated in batch sorption and TRLFS studies, respectively. Sorption of Eu^{3+} was found to start at a pH-value of 4. Based on TRLFS results, sorption of Cm^{3+} was assigned to occur through inner-sphere complex formation at the zirconia surface. A deconvolution of the TRLFS emission spectra gave three different sorption species with strong red-shifts of the peak positions (600.3 nm, 604.3 nm and 608.2 nm) compared to similar systems.

Zirconium(IV) oxide is a corrosion product of the zircalloy cladding material surrounding nuclear fuel rods.[1] Therefore, studies involving interaction of actinides with ZrO_2 are necessary to enable predictions about the long term safety of final repositories for nuclear waste.

EXPERIMENTAL. In the batch sorption investigations, the sorption of 1×10^{-7} M and 1×10^{-5} M Eu^{3+} on 0,5 g/L and 5 g/L ZrO_2 was studied as a function of pH. The samples were separated by centrifugation at a relative centrifugal force of 4,025 and the Eu^{3+} concentration in the supernatant was measured with inductively coupled plasma mass spectrometry. The surface complexation and in situ speciation of 5×10^{-7} M Cm^{3+} in a 0.5 g/L ZrO_2 suspension at varying pH was investigated by TRLFS. All samples were prepared in a glove box under inert atmosphere (N_2; $O_2 < 0.1$ ppm). For the measurements, the samples were pipetted into cuvettes, which were sealed in the glove box. The laser system was a pulsed Nd:YAG (Continuum Surelite II or Powerlite Precision II 9020) pump laser coupled to a solid-state optical parametric oscillator (OPO, PANTHER EX OPO, Continuum). The excitation of Cm was carried out at 396.6 nm and the luminescence emission spectra were recorded 1 µs after the exciting laser pulse.

RESULTS. From the batch sorption experiments using Eu^{3+} as an actinide analogue, sorption can be seen to occur already at a pH-value of approximately 4.0–4.2 depending on the metal ion concentration used in the experiments. Complete sorption is reached at approximately pH 5.3 in both cases (Fig. 1).
The emission spectra obtained in the TRLFS measurements show a deviation from the aquo ion starting at pH 4.0, implying that inner-sphere sorption occurs on the ZrO_2 surface. A deconvolution of the spectra collected at various pH values (3.0–10.8) reveals three different pH-dependant species on the ZrO_2 surface showing peak positions at 600.3 nm, 604.3 nm and 608.2 nm (Fig. 2).

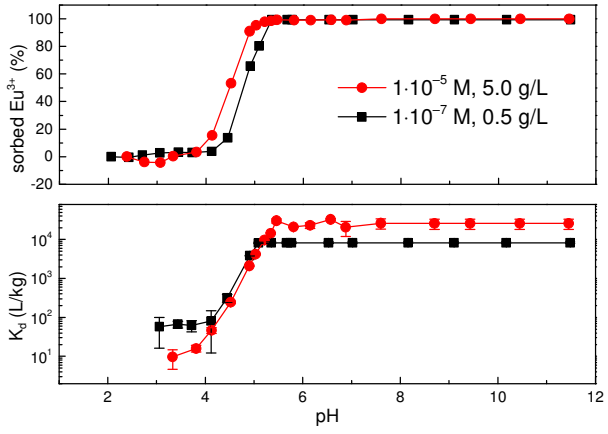

Fig. 1: Batch sorption curves for Eu^{3+} on ZrO_2 plotted as sorption percentage (top) and as sorption distribution coefficient, K_d (bottom).

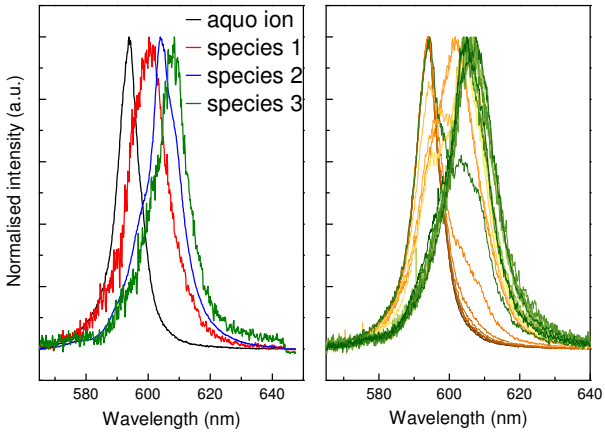

Fig. 2: Deconvoluted species from sorption experiments of 5×10^{-7} M Cm^{3+} on 0.5 g/L ZrO_2 (left) and emission spectra from the sorption experiments in the pH-range from 3.0 to 10.8 (right).

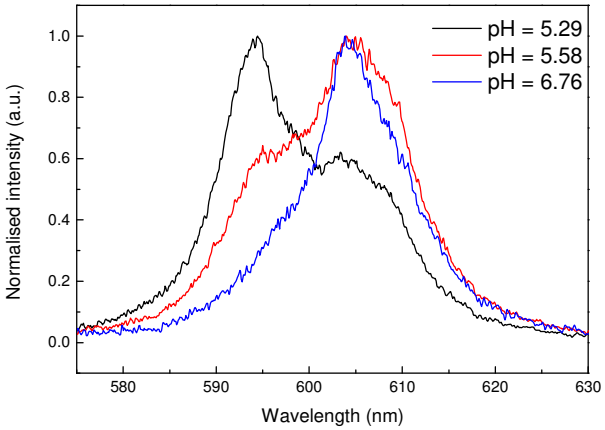

Fig. 3: Selected emission spectra from sorption species of 5×10^{-7} M Cm^{3+} on 0.5 g/L ZrO_2.

The red shift of the two latter species is very large in comparison to Cm^{3+} surface complexes found on other oxide minerals such as corundum or γ-Al_2O_3.[2, 3] In addition, a closer look on the emission spectra shows a red shifted shoulder in the pH-region between 5 and 6 which disappears with increasing alkalinity (Fig. 3).
Therefore, it is not clear whether the identified sorption species can be explained only by the adsorption of Cm^{3+} hydrolysis complexes with increasing pH as done in previous studies on Cm^{3+} sorption onto oxide minerals[2, 3] or whether a different retention mechanism has to be considered. Thus, further investigations need to be done for a complete understanding of the surface sorption processes on the ZrO_2 system.

[1] Cox, B. (2004) *J. Nucl. Mater.* **336**, 331–368.
[2] Rabung, T. *et al.* (2006) *Radiochim. Acta* **94**, 609–618.
[3] Kupcik, T. *et al.* (2016) *J. Colloid Interface Sci.* **461**, 215–224.

Effect of glutamic acid on copper sorption onto kaolinite – Batch experiments and surface complexation modeling

L. Karimzadeh, R. Barthen, M. Stockmann, M. Gründig, K. Franke, J. Lippmann-Pipke

In this work, we study the mobility behavior of Cu(II) under conditions related to an alternative, neutrophile biohydrometallurgical Cu(II) leaching approach. Sorption of copper onto kaolinite influenced by glutamic acid (Glu) was investigated in the presence of 0.01 M $NaClO_4$ by means of binary and ternary batch adsorption measurements over a pH range of 4 to 9 and surface complexation modeling.

EXPERIMENTAL. Sorption experiments were performed in continuously stirred glass beakers containing 500 mL distilled water and 0.01 M $NaClO_4$ as the background electrolyte. Solutions were titrated first to an acidic initial pH (~4) using trace metal grade HNO_3. Next, 500 mg kaolinite was added to the well-stirred solution. The suspension was pre-equilibrated for 24 hours. The binary sorption systems containing kaolinite and 0.1 mM Glu or 0.1 mM Cu(II) and the ternary sorption system containing kaolinite and a equimolar ratio of Cu(II) and Glu were obtained by adding the respective solutions. The pH of the suspensions was adjusted to the pH range from 4–9 by addition of 0.1 mM NaOH and left to equilibrate for 30 min. After stabilization of the pH, a 10 mL aliquot of the suspension was pipetted into a 12 mL plastic vial, agitated with a shaker (ROTATHERM) for 24 hours. After this time, the pH of the suspension was measured again, and samples were filtered through 0.2 µm cellulous acetate syringe filters (Sartorius Stedim Biotech GmbH, Germany). All samples were analyzed for Cu(II) and Glu. For surface complexation reactions, the CD-MUSIC model introduced by Hiemstra with using the geochemical speciation code PHREEQC (version 3) was used to describe the sorption of Cu(II) and/or Glu on the surface of the kaolinite mineral.[1, 2] One type of surface hydroxyl groups (≡SOH) was chosen as sorption edge sites with formation of monodentate Cu(II) complexes on variable charge surface sites.

RESULTS. Copper sorption in the absence of Glu was dependent on pH and initial copper concentration. In contrast, sorption of Glu was weak (~5 %) and independent of pH (Fig. 1). In Fig. 1b, the adsorption behavior of Cu on kaolinite in the absence of Glu is compared to that of the ternary sorption system (presence of Glu). Adsorption edge data show that Glu significantly affect the Cu(II) adsorption. Above pH 5 and in the presence of Glu, the uptake of Cu(II) is inhibited relative to the single-sorbat system. Glu reduces the copper sorption onto kaolinite at alkaline pH and therewith enhances copper mobility in the presence of kaolinite due to the formation of Cu(II)-ligand complexes in solution. However, under acidic pH Glu slightly decreased copper mobility. This can be interpreted as sorption of Cu-glutamate complexes on the sorption surface edge sites of kaolinite.[3] The presence of Cu(II) slightly increased the adsorption of Glu by kaolinite (Fig. 1a). This can be explained by the formation of a ternary complex where the positively charged cupric ion serves as a bridge between the negatively charged kaolinite surface and the Glu molecule.[4]
The application of the CD-MUSIC model successfully describes the experimental data. The low affinity of glutamate, as well as the weak influence of cupric ions on glutamate adsorption to kaolinite surfaces, is well presented in the results of modeling (Fig. 1a). Furthermore, modeling of the Cu(II) adsorption edge data using the surface complexation reactions provides a close fit to the experimental data (Fig. 1b) and predicted the effect of Glu on metal adsorption.

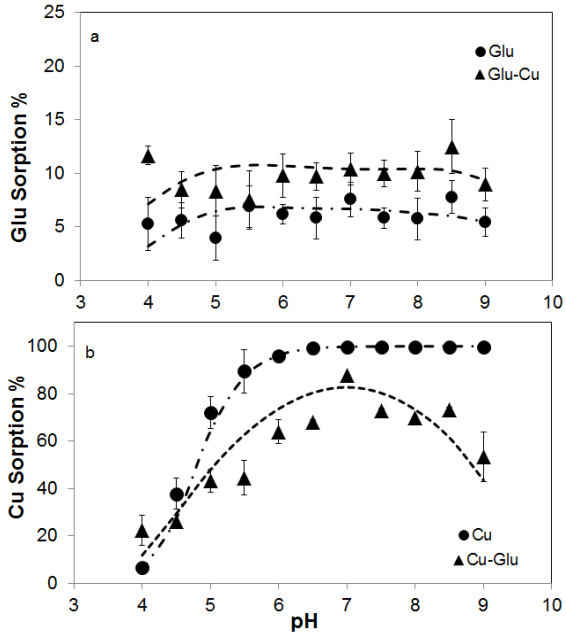

Fig. 1: Results of measured (points) and modelled (lines) glutamic acid adsorption (a) and Cu(II) adsorption (b) on kaolinite.

ACKNOWLEDGEMENTS. This work is conducted in the framework the EcoMetals project funded jointly by the German Federal Ministry of Education and Research (BMBF) project ref. No. 033RF001, and the Agence Nationale de la Recherche (ANR), France.

[1] Hiemstra, T. *et al.* (1996) *J. Colloid Interface Sci.* **179**, 488–508.
[2] Parkhurst, L. D. *et al.* (2013) *User's guide to PHREEQC V.3* , p. 497, U.S.G.S., Denver, U.S.A.
[3] Fitts, J.P. *et al.* (1999) *J. Colloid Interface Sci.* **220**, 133–147.
[4] Yeasmin, S. *et al.* (2014) *J. Colloid Interface Sci.* **432**, 246–257.

Extraction of 3D velocity and porosity fields from GeoPET data sets

J. Lippmann-Pipke, S. Eichelbaum,[1] J. Kulenkampff
[1]Nemtics Visualization, Leipzig, Germany

Geoscientific process monitoring with positron emission tomography (GeoPET) is proven to be applicable for quantitative tomographic transport process monitoring in natural geological materials.[1, 2] We benchmarked GeoPET by inversely fitting a numerical finite element model to a diffusive transport experiment in Opalinus clay. The obtained effective diffusion coefficients, $D_{e,\parallel}$ and $D_{e,\perp}$, are well in line with data from literature.[3] But more complex, heterogeneous migration, and flow patterns cannot be similarly evaluated by inverse fitting using optimization tools. Alternatively, we started developing an algorithm that allows the quantitative extraction of velocity and porosity fields, $v_{i=x,y,z}(x,y,z)$ and $n(x,y,z)$ from GeoPET time series, $c_{PET}(x,y,z,t)$. They may serve as constituent data sets for reactive transport modelling.

EXPERIMENTAL. To assist in developing the algorithm, a phantom (Fig. 1) was manufactured and used in an experiment with tracer transport visualization by means of GeoPET. Further was that phantom scanned by means of µCT and used for a numerical flow and transport model. The obtained velocity and porosity fields serve as control for the results obtained by the algorithm extracting velocity and porosity fields from GeoPET data sets.

RESULTS. The algorithm (embedded in a graphical user interface and running under Linux and Windows) well evaluates 4D data sets from tomographic measurements (PET or MRI) and from numerical model runs (e.g. COMSOL Multiphysics®). The algorithm is capable of tackling noise, measurement thresholds, and concentration "gabs" along flow paths (discontinuous flow patterns). It returns – among other things – calculated concentration fields (if source data had to be cut, rotated or scaled), the velocity and porosity fields, the direction of flow, the transport error, and flow topology information. The software saves these results in various formats, e. g. for subsequent use in numerical modelling software.
The algorithm will be provided as open source along with a detailed performance analysis and evaluation of the returned results in a full journal article (in preparation).

ACKNOWLEDGEMENTS. The authors thank D. Lösel and M. Gründig for her support during the conduction of the experiments and N. Korn for his engagement during the early stages of the development of the algorithm.

[1] Kulenkampff, J. *et al.*, (2016) *Solid Earth* **7**, 1207–1215.
[2] Kulenkampff, J. *et al.*, (2016) *Solid Earth* **7**, 1217–1231.
[3] Lippmann-Pipke, J. *et al.* (2017) *Comp. Geosci.* **101**, 21–27.

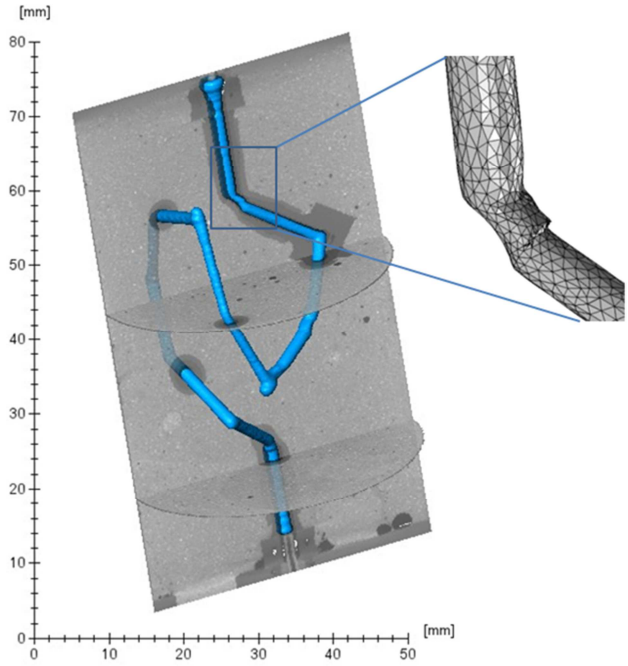

Fig. 1: *Left*: Phantom of tube embedded in concrete. *Right*: Detail of meshed geometry obtained from µCT for numerical flow model.

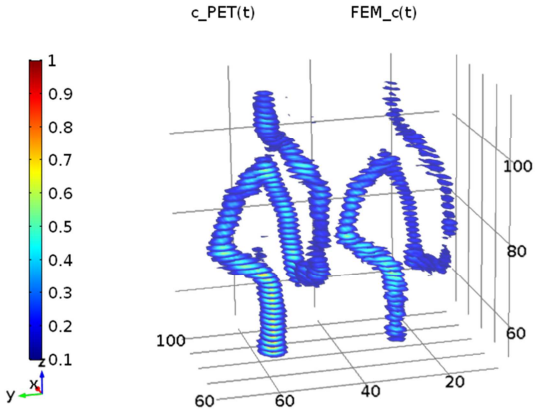

Fig. 2: *Left*: Measured concentration distribution during the GeoPET tracer flow experiment at a certain time, *t*. *Right:* Result of the respective simulation based on velocity and porosity fields as extracted from $c_{PET}(x,y,z,t)$.

Long-Lived Radionuclides in

BIOLOGICAL SYSTEMS

Internal hydration of a metal-transporting ATPase is controlled by membrane lateral pressure

K. Fahmy, E. Fischermeier,[1] P. Pospisil,[2] A. Sayed, M. Solioz,[3] M. Hof

[1]Technische Universität Dresden, Dresden, Germany; [2]J. Heyrovský Inst. Physical Chemistry of the A.S.C.R., Prague, Czechia; [3]University of Bern, Bern, Switzerland

The active transport of ions across biological membranes requires their hydration shell to interact with the interior of membrane proteins. However, the influence of the external lipid phase on internal dielectric dynamics is hard to access by experiment. Using the octahelical transmembrane architecture of the copper-transporting P_{1B}-type ATPase from *Legionella pneumophila* (LpCopA) as a model structure, we have established the site-specific labeling of internal cysteines with a polarity-sensitive fluorophore. This enabled dipolar relaxation studies in a solubilized form of the protein and in its lipid-embedded state in nanodiscs (NDs). Time-dependent fluorescence shifts revealed the site-specific hydration and dipole mobility around the conserved ion-binding motif. The spatial distribution of both features is shaped significantly and independently of each other by membrane lateral pressure.[1]

EXPERIMENTAL. The plasmid pMSP1E3D1 was from Addgene and expressed and purified as described.[2] The LpCopA gene lpg_1024 from *Legionella pneumophila* was synthesized by GeneArt (Life Technologies) cloned in the pProExHTa vector and expressed with an N-terminal 6His-tag in C43(DE3)pLysS or BL21(DE3) Rosetta cells. Cysteines were replaced by serine except for either of the ion-binding Cys382 or Cys384. After cell lysis, membrane proteins were solubilized with *n*-dodecyl-β-D-maltoside (DDM) at 0.63 % w/v and purified 1 mL Ni-NTA HiTrap column on which the protein was also labeled specifically at Cys382 or Cys384 with the solvatochromic fluorophore 6-bromoacetyl-2-dimethylaminonaphthalene (BADAN). BADAN-labeled LpCopA was assembled into NDs at molar ratios of LpCopA : MSP1E3D1(monomer) : asolectin of 1 : 5 : 200 at 3 to 8 µM LpCopA. The detergent was removed with Bio-Beads SM-2 (BioRad) and LpCopA-NDs purified with His SpinTrap columns (GE-HealthCare). Time-resolved emission was studied by single photon counting.[3]

RESULTS. Figure 1 shows the time-dependent fluorescence shift (TDFS) of the peak emission frequency of BADAN linked to the native copper-binding cysteine C382 in the transmembrane domain of LpCopA when the protein was solubilized in detergent micelles. The dipolar relaxation in the environment of the label lowered the excited state energy at later emission times leading to a decrease in emission frequency. The amount and kinetics of the dipolar relaxation correlate with the amplitude $\Delta\nu_{total}$ and the average

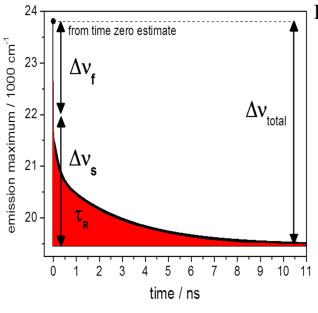

Fig. 1: TDFS of BADAN bound to C382. The calculated frequency ν(0) is displayed as a dot. The total TDFS, $\Delta\nu_{total}$, covers the shift from ν(0) to ν(∞), accounting for the fast TDFS (less than 30 ps, $\Delta\nu_f$), and the slower experimentally resolved TDFS ($\Delta\nu_s$). The overall TDFS kinetics is derived from the average time constant τ_R.

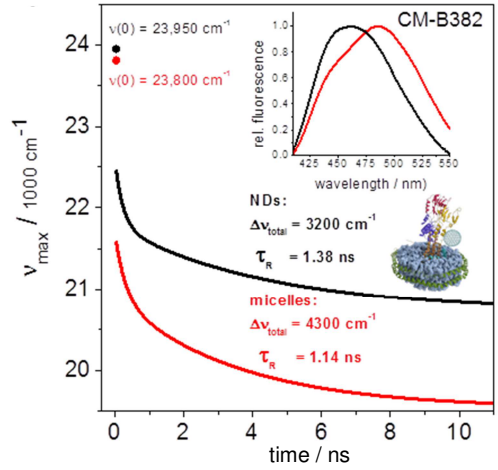

Fig. 2: TDFS of BADAN bound to C382 (A) or C384 (B) of the CM-mutant. The ν(0) frequencies are displayed as filled circles. Samples were measured in detergent solution (red) and in nanodiscs (black). Insets show the static emission spectra of the two states. The molecular graphics show the putative structure of LpCopA in the MSP1E3D1-bounded bilayer of lipids from soy bean (asolectin).

realxation time τ_R, respectively. Both parameters were strongly affected by the reconstitution of the membrane protein into NDs: the relaxation time became longer and the total frequency shift reduced (Fig. 2). This can be explained by a lower degree of intramembrane protein hydration and restricted dipole mobility. Correspondingly, the lateral pressure exerted by the lipid bilayer on the transmembrane helices lead to tighter helical packing and dehydration at the metal-binding site. The effects are large enough to be seen as fluorescence shifts also in the static emission spectra (Fig. 2 insets). The peak emission was translated into apparent dielectric constants using BADAN emission measured in solvents of different polarity. Figure 3 summarizes the lipid-induced alterations which show that the hydration of the active site of ion transporters can be regulated by the membrane environment without requiring direct contact between the lipidic phase and the ion-coordinating site.

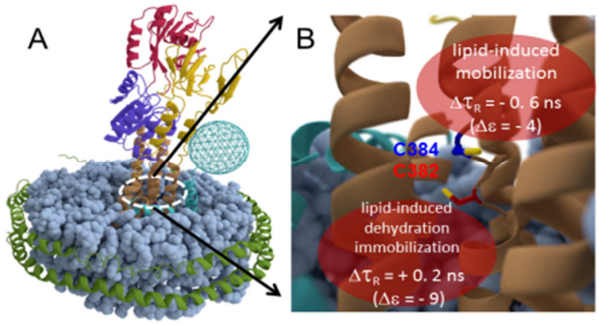

Fig. 3: Putative structure of LpCopA in NDs (A) and sketch of the ion-binding site with the lipid-regulated physical properties (B).

ACKNOWLEDGEMENTS. We are grateful to Jenny Philipp and Elisabeth Lessmann for valuable biochemical and technical support.

[1] Fischermeier, E. *et al.* (2017) *Angew.Chem.* **129**, 1289–1292.
[2] Ritchie, T. K. *et al.* (2009) *Methods Enzymol.* **464**, 211–231.
[3] Jurkiewicz, P. *et al.* (2005) *J. Fluoresc.* **15**, 883–894.

Glutathione attenuates uranyl toxicity in *Lactococcus lactis*

K. Fahmy, M. Obeid,[1] M. Solioz,[2] J. Oertel
[1]Technische Universität Dresden, Dresden, Germany; [2]University of Bern, Bern, Switzerland

We investigated the role of intracellular glutathione (GSH), which in a large number of taxa plays a role in the protection against the toxicity of heavy metals. Anaerobically grown *Lactococcus lactis* containing an inducible GSH synthesis pathway was used as a model organism allowing the study of GSH-dependent uranyl detoxification without interference from additional reactive oxygen species. Microcalorimetric measurements of the metabolic heat showed that intracellular GSH attenuates the toxicity of uranium at a concentration in the range of 10–150 µM. Isothermal titration calorimetry revealed the endothermic binding of U(VI) to the carboxyl group(s) of GSH. The data indicate that the primary detoxifying mechanism is the intracellular sequestration of carboxyl-coordinated U(VI) into an insoluble complex with GSH.[1]

EXPERIMENTAL. The strain NZ9000-pNZ3203 of *L. lactis* subsp. *cremoris* (NIZO food research B.V., The Netherlands) carries a plasmid with the *gshA* and *gshB* genes under the control of the *nisA* promoter, rendering the expression of the two genes, which are required for GSH synthesis, inducible by nisin. Bacteria were grown at pH 7.2 in M17 medium. Rate constants for exponential growth phases were calculated using the relation: $\int P(t)\,dt = H(t)$, with P(t): heat flow at time t (µW), and H(t): integrated heat (Joule). For exponential growth, the slope of a linear stretch in a heat flow *vs.* integrated heat plot is $dP/dH = k$ which is the growth rate k of the culture.

RESULTS. Plots of the heat flow *vs.* integrated heat recorded from *L. lactis* cultures in the presence of varying concentrations of uranyl are shown in Fig. 1. Linear stretches represent exponential growth phases. Non-induced cells do not produce GSH and the rate of their second exponential growth phase (proportional to the slope of the fitted lines) declines pronouncedly with increasing uranyl concentration (left panel). In the presence of nisin, the cells produce intracellular GSH and their second exponential growth becomes more resistant to uranyl (right panel). The quantitative analysis in Fig. 2 shows that uranyl does not affect initial growth rate k_1 but specifically interferes with the metabolism at later exponential growth described by k_2. GSH clearly attenuates the toxicity of uranyl during that phase, allowing larger exponential growth still up to 100 µM uranyl nitrate. The molecular mechanism of GSH-dependent modulation of uranyl toxicity is most likely due to the formation of an insoluble GSH uranyl complex as revealed by isothermal titration calorimetry of uranyl nitrate in aqueous GSH solution. Figure 3 shows the transition from complex formation (endotherm) to precipitation (exotherm) The determined enthalpic and entropic terms agree with the binding of uranyl the carboxylate function of GSH.[2]

ACKNOWLEDGEMENTS. We are grateful to Jenny Philipp for valuable biochemical and technical support.

[1] Obeid, M. *et al.* (2016) *Appl. Environ. Microbiol.* **82**, 3563–357.
[2] Bismondo, A. *et al.* (1992) *Thermochim. Acta* **196**, 131–136.

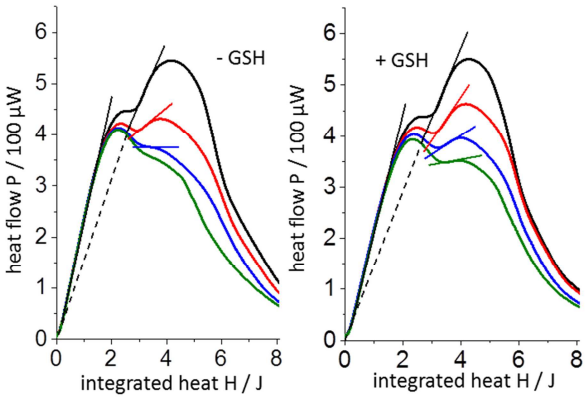

Fig. 1: Metabolic thermal power *vs.* integrated metabolic heat. Colored lines indicate exponential growth at 0, 50, 100, 150 µM uranyl. Left: growth without GSH production, right: growth with GSH production. Slopes scale with growth rates k_1 and k_2 (H > 3 J).

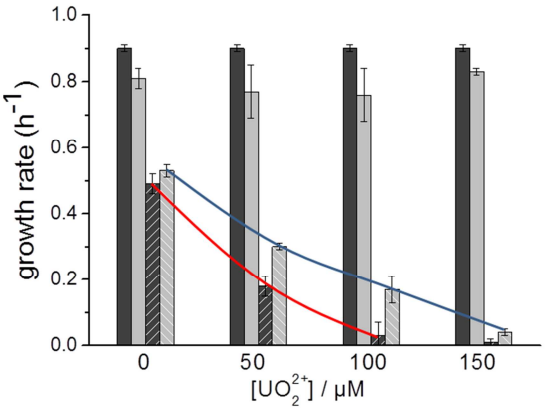

Fig. 2: Growth rates k_1 (no texture) and k_2 (hatched) of early and late exponential growth, respectively, as function of uranyl nitrate concentration. Rate k_1 is independent of GSH production (light grey), whereas k_2 (dark grey) decreases with uranyl concentration (red trace). The decrease is less pronounced in the presence of GSH (blue trace).

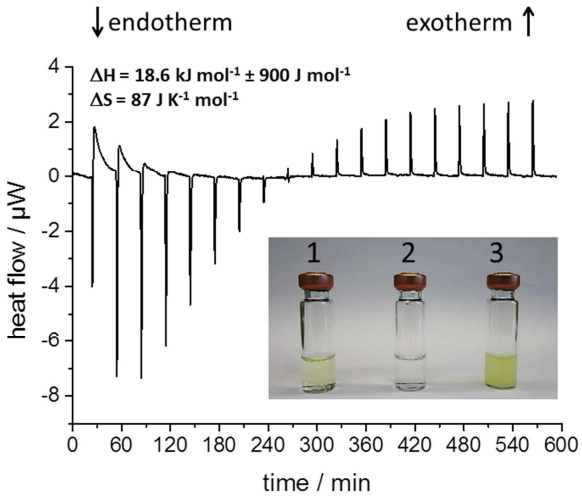

Fig. 3: Isothermal titration calorimetry. Ten-microliter aliquots of a 200 mM solution of GSH were injected into 5 mM uranyl nitrate at pH 4.5. The picture shows the uranyl (1) and GSH (2) solution before mixing. The turbidity upon mixing reveals an insoluble complex (3).

Pu oxidation state distributions in suspensions of the Mont Terri Opalinus Clay isolate *Sporomusa* sp. MT-2.99

H. Moll, A. Cherkouk, F. Bok

The time-dependent ^{242}Pu oxidation state distribution in the presence of *Sporomusa* sp. cells as a function of pH with or without Na-pyruvate was analyzed. In all cases, the presence of bacterial cells enhanced removal of Pu from solution and accelerated Pu interaction reactions, e.g. biosorption and bioreduction.

Clay is one potential host rock for a safe storage of nuclear waste in a deep geological repository. The indigenous bacterium *Sporomusa* sp. MT-2.99 was isolated from Mont Terri Opalinus Clay, which can serve as such a potential host rock.[1] In order to describe the fate of accidentally released plutonium in such an environment, knowledge is necessary on how these bacteria are interacting with plutonium. Our report aims to summarize the knowledge regarding Pu-*Sporomusa* interactions.[2, 3]

EXPERIMENTAL. The experimental details are summarized in literature.[2, 3] New experiments were performed anaerobically at [dry biomass] of 0.33 ± 0.01 $g_{dry\ weight}$/L in the presence of 10 mM Na-pyruvate at pH 4 at 25 °C in 0.1 M $NaClO_4$. Details about the Eh-pH calculations using geochemical speciation "Geochemist's Workbench"® 11.0.3 can be found in.[4]

RESULTS. Figure 1 depicts a generalized Eh–pH diagram of the dominant Pu species that exist for a range of Eh and pH values calculated under anaerobic conditions. As a result of the batch experiments, in the blanks with no electron donor, the decrease of Pu(VI) at pH 6.1 was 3.2 times faster than at pH 4. The increase of Pu(V) at pH 6.1 was 3.3 times faster than at pH 4.

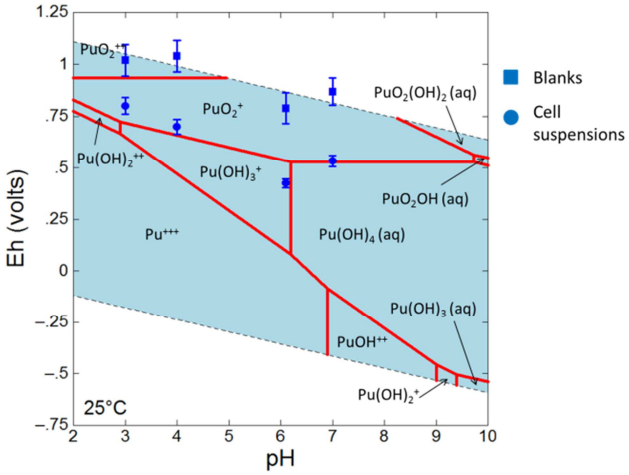

Fig. 1: Eh–pH diagram of Pu calculated for a 0.1 M $NaClO_4$ solution with 180 µM Pu in the absence of CO_2 at 25 °C. The diagram includes the measured Eh and pH values from selected experiments at pH 3, 4, 6.1, and 7 (blanks and corresponding cell suspensions).[4]

At pH 4, Pu(VI) was more stabilized in the blanks. This observation and the dominance of Pu(V) is in agreement with the Eh-pH calculations shown in Fig. 1. A significant change of the Pu oxidation state distributions was observed in the supernatants compared with the blanks if no electron donor was added. At both pH values, a fast decrease of Pu(VI) combined with a fast increase of Pu(V) was observed. These processes were accelerated due to the influence of the cells. The observed cell mediated reduction process of Pu(VI) to Pu(V) is not yet fully understood. The dominance of Pu(V) in the supernatants/cell suspensions is also in agreement with the Eh-pH calculations shown in Fig. 1 (for pH 3, 4, and 7). For the cell suspension at pH 6.1 predominantly Pu(IV) was predicted (cf. Fig. 1). This could not be confirmed experimentally due to the dominance of Pu(V).
The cells displayed a strong pH dependent affinity for Pu. In the absence of Na-pyruvate, a strong enrichment of stable Pu(V) in the supernatants was discovered, whereas Pu(IV)-polymers dominated the Pu oxidation state distribution on the biomass at pH 6.1 (cf. Fig. 2). A pH-dependent enrichment of the lower Pu oxidation states (e.g. Pu(III) at pH 6.1 which is considered to be more mobile than Pu(IV) formed at pH 4) was observed in the presence of up to 10 mM Na-pyruvate (cf. Fig. 2).

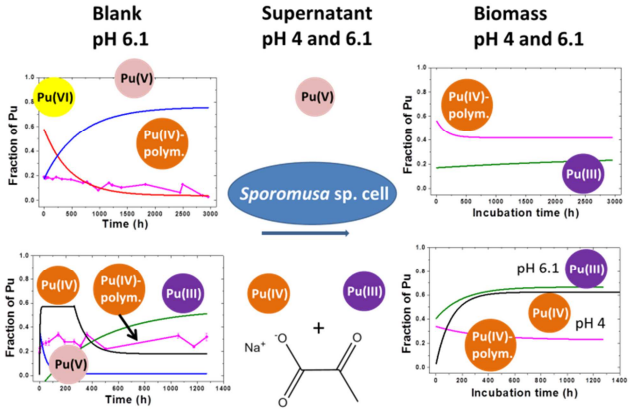

Fig. 2: Summary of Pu oxidation state distributions measured in the batch experiments with *Sporomusa* sp. MT-2.99 cells.

To conclude, a moderate to strong impact of *Sporomusa* sp. cells on the Pu speciation was observed. Parameters influencing the Pu interaction process were the pH, the initial Pu concentration, the Pu speciation and the presence or absence of an electron donor, in this case Na-pyruvate. The results presented contribute for a better mechanistic understanding for Pu biogeochemistry at the molecular level in the presence of host rock indigenous bacterial cells.

ACKNOWLEDGEMENTS. The authors thank the BMWi for financial support (contract no.: 02E10618 and 02E10971), Velina Bachvarova and Sonja Selenska-Pobell for isolation and Monika Dudek for cultivation of the bacteria, as well as the BGR for providing the clay samples.

[1] Bachvarova, V. *et al.* (2010) *Report FZD-530*, p. 18.
[2] Moll, H. *et al.* (2015) *Report HZDR-059*, p. 15.
[3] Moll, H. *et al.* (2016) *Report HZDR-067*, p. 47.
[4] Moll, H. *et al.* (2017) *Environ. Sci. Pollut Res.*, submitted.

Interaction of Eu(III) and Cm(III) with mucin – A key component of the human mucosa

C. Wilke, A. Barkleit

To evaluate the potential health risks caused by the ingestion of lanthanides (Ln) and actinides (An), investigations into the chemical behavior of these metals in the human gastrointestinal tract are necessary. Mucin is an important part of the protective mucosa layer in the digestive system. We have recently reported that mucin interacts strongly with Eu(III) and Cm(III), representatives of Ln(III) and An(III), respectively, under *in vivo* conditions.[1] In order to investigate the complexation behavior of this protein with Ln(III)/An(III), TRLFS measurements were performed on Eu(III)/Cm(III)-mucin solutions with different protein concentrations and at different pH. The results indicate the formation of at least two independent mucin species. At higher pH, the formation of hydroxide species was also observed.

In general, the lanthanide and actinide elements have no significant vital roles. However, through different processes such as nuclear accidents, these heavy metals could be potentially released into the environment where they could be incorporated into the food chain and eventually into the human body through oral ingestion. Because of the chemical- and radiotoxicity of An, it is important to understand their chemical and biological behavior under *in vivo* conditions for the reliable health risk assessment of these elements. Our previous report has revealed that the protein mucin is an important binding partner for Eu(III) and Cm(III) in the human gastrointestinal tract.[1] Mucins are high molecular weight glycoproteins and an important component of mucosa, which is a thick and viscoelastic layer covering the whole digestive system. Mucosa also acts as a protective barrier to pathogens and toxic substances. Responsible for its protective functions is the protein mucin.[2] Based on this background, this study focuses on the interaction of this protein with Eu(III) and Cm(III) as representatives of the Ln(III) and An(III), respectively.

EXPERIMENTAL. A solid form of mucin was weighed and dissolved in an aqueous solution to mix with Eu(III) or Cm(III). The final metal concentrations in the sample solutions were 1×10^{-5} M and 3×10^{-7} M for Eu(III) and Cm(III), respectively. For the constant pH experiments, the mucin concentration was ranged from 0.01 to 2 mg/mL, while the pH was varied between 1 and 10 with a mucin concentration of 1 mg/mL for the constant mucin concentration experiments. All sample solutions had a constant ionic strength of 0.1 M NaCl. The TRLFS measurements of the prepared samples were carried out at room temperature. For radiation safety reasons, the measurements with Cm(III) were performed in a glove box under nitrogen atmosphere, while the measurements with Eu(III) were carried out in ambient atmosphere.

RESULTS. In Fig. 1, the luminescence spectra of Eu(III) (left) and Cm(III) (right) with different mucin concentrations are shown. The Eu(III) spectra exhibit an increasing trend in luminescence intensity associated with the $^5D_0 \rightarrow {}^7F_2$ emission band at ~615 nm with increasing the mucin concentration. Additionally, the presence of the symmetry forbidden $^5D_0 \rightarrow {}^7F_0$ emission band at ~580 nm indicates the formation of asymmetric complexes. These results suggest the complex formation between Eu(III) and mucin. The Cm(III) spectra show a red shift with increasing mucin concentration and the spectral shape is unchanged above the mucin concentration of 0.3 mg/mL. At the highest mucin concentrations, at least two independent species were detected with the average luminescence lifetimes of $\tau_1 = 146 \pm 7$ µs and $\tau_2 = 431 \pm 16$ µs, and $\tau_1 = 94 \pm 3$ µs and $\tau_2 = 268 \pm 5$ µs for Eu(III) and Cm(III), respectively. The longer lifetimes correspond to 6–7 water molecules in the first coordination sphere, while the shorter lifetimes suggest ~2 water molecules remaining in the first coordination sphere.

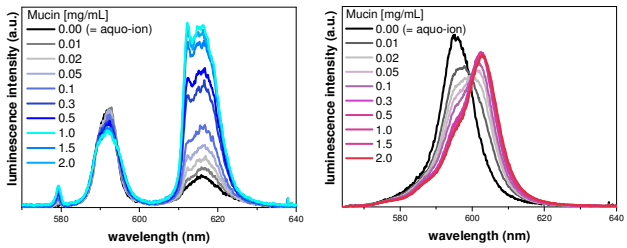

Fig. 1: Luminescence spectra of Eu(III) (1×10^{-5} M, left) and Cm(III) (3×10^{-7} M, right) with different mucin concentrations at pH 4.5 and room temperature.

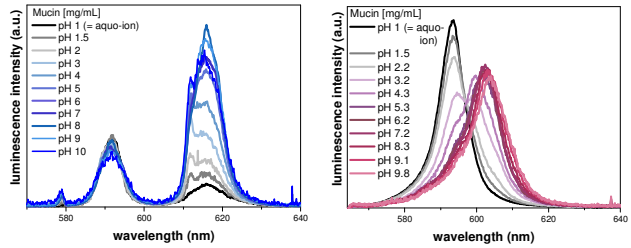

Fig. 2: Luminescence spectra of Eu(III) (1×10^{-5} M, left) and Cm(III) (3×10^{-7} M, right) at different pH with a constant mucin concentration of 1 mg/mL at room temperature.

As shown in Fig. 2, the luminescence spectra of Eu(III) at different pH show again an increasing trend in the luminescence intensity associated with the $^5D_0 \rightarrow {}^7F_2$ emission with increasing the pH up to 8. However, the luminescence intensity decreases at pH 10 due to the formation of hydroxide species. The Cm(III) spectra at different pH indicate a red shift with increasing pH and a peak splitting at pH 3.2. As observed for the Eu(III) results, there is a decrease in the Cm(III) luminescence intensity at pH 10 because of the formation of hydroxide species. The luminescence lifetimes decay bi-exponentially for both experiment series. At pH 8–9, which represents the highest pH range before the hydroxide precipitation occurs, the average lifetimes are $\tau_1 = 362 \pm 15$ µs and $\tau_2 = 784 \pm 22$ µs, and $\tau_1 = 131 \pm 7$ µs and $\tau_2 = 403 \pm 12$ µs for Eu(III) and Cm(III), respectively. These lifetimes correspond to 2–4 and 1 water molecules in the first coordination sphere.

ACKNOWLEDGEMENTS. This work was funded by the Federal Ministry of Education and Research (02NUK030F).

[1] Wilke, C. *et al.* (2015) *Report HZDR-059*, p.12.
[2] Bansil, R. *et al.* (2006) *Curr. Opin. Colloid Interface Sci.* **11**, 164–170.

Thermal unfolding of a Ca- and Lanthanide-binding protein

K. Fahmy, J. Knoeppel, M. Göttfert[1]
[1]Technische Universität Dresden, Dresden, Germany

The MIIA (metal ion-induced autocleavage)-domain of the protein Vic_001052 from the pathogen *Vibrio coralliilyticus*, comprises 173 amino acids and exhibits Ca-dependent autoproteolytic activity.[1] It shows homology to nodulation proteins which are secreted by *Rhizobiacea* into plant host cells where they exert Ca-dependent functions. We have studied the structural and energetic aspects of metal protein interactions of the MIIA domain which appear attractive for engineering metal-binding synthetic peptides. Using a non-cleavable MIIA domain construct, we detected very similar structural changes upon binding to Ca^{2+} and Eu^{3+}. The thermal denaturation of the Ca-bound state was studied by circular dichroism (CD) spectroscopy. The metal-bound folded state unfolds reversibly into an unstructured metal-free state similar to the metal-free state at room temperature.

EXPERIMENTAL. The MIIA- domain was expressed and purified as described and studied spectroscopically in pure aqueous solution.[1] After acquisition of a CD spectrum between 320 and 185 nm, the protein (3–4 µM) was heated at a rate of 1 °C/min in the presence of Ca^{2+} (100 µM). Every 2 °C, near UV-CD-spectra were taken from 250 nm to 185 nm at a rate of 100 nm/min and a bandwidth of 3 nm. Two spectra were averaged at each temperature with a residual variation of less than 0.1 °C.

RESULTS. CD-spectra of the MIIA-domain are shown in Fig. 1. Between 18 °C and 40 °C, the protein shows a negative peak at 220 nm and a strong positive band at 195 nm. This band shape is indicative of a fraction of α-helical structure and was only observed in the presence of Ca^{2+}. It corresponds to 15 % helical secondary structure at room temperature as analyzed by DichroWeb.[2] With increasing temperature, the CD-signature of the folded state disappears, whereas a new negative peak at 200 nm is formed and is the only prominent feature above 70 °C. The high temperature CD spectra are thus indistinguishable from the room temperature spectra of the protein measured in the absence of metal ions (not shown). As all spectra intersect in an isosbestic point at 210 nm, it is justified to analyze the data in a two

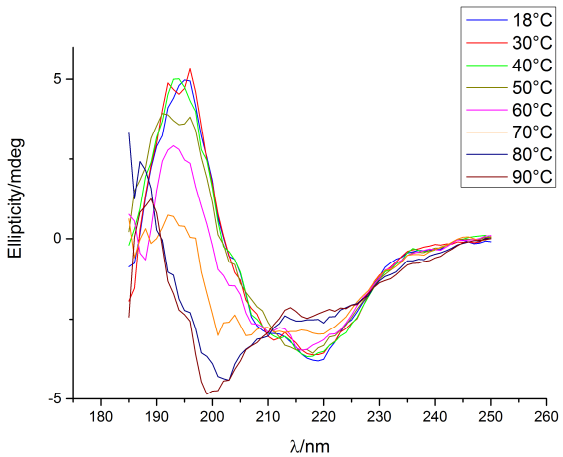

Fig. 1: CD-spectra of the Ca^{2+} bound MIIA-Domain at different temperatures. The plot shows the thermal denaturation from the folded state at room temperature to a state, which is similar to the state without metal-ions present, at high temperatures.

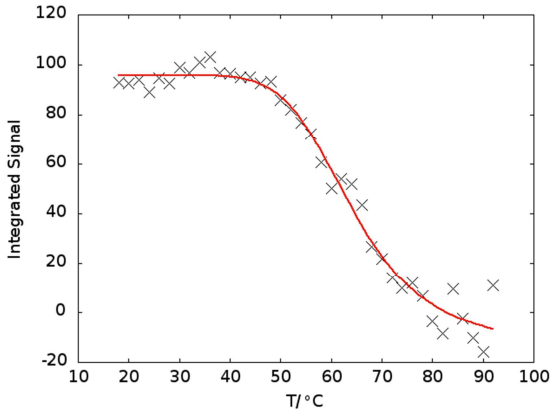

Fig. 2: Integrated spectral intensity (S(λ < 210 nm) − S(λ > 210 nm)) as a function of temperature. The curve shows the fit of the sigmoid according to the equation for S given in the text.

state model of protein unfolding. For this purpose, the data points for λ < 210 nm of each spectrum are summed up and subtracted from the sum of data points for λ > 210 nm. This integration increases the signal to noise ratio and its numeric value scales with the concentration of the unfolded state, which is expected to increase from zero to saturation upon heating. The resulting sigmoidal temperature dependence of the integrated CD signal (S) is shown in Fig. 2. It is estimated to satisfy a two state model (U: unfolded, F: folded state) with a temperature-dependent equilibrium constant K = [U] / [F] according to $S = A_2 / (1 + K^{-1}) - A_1$. Using

$$K = \exp\left(\frac{\Delta G}{RT}\right) = \exp\left(\frac{\Delta S}{R} - \frac{\Delta S T_m}{RT}\right),$$

and the observed temperature T_m = 64 °C, at which half of the protein was unfolded, a satisfactory fit is obtained (Fig. 2) with unfolding entropy $\Delta S = 71$ J mol^{-1} K^{-1} and enthalpy $\Delta H = 23.9$ kJ mol^{-1}. The unfolding was reversible as shown in Fig. 3. With Eu^{3+}, no reversibility was observed.

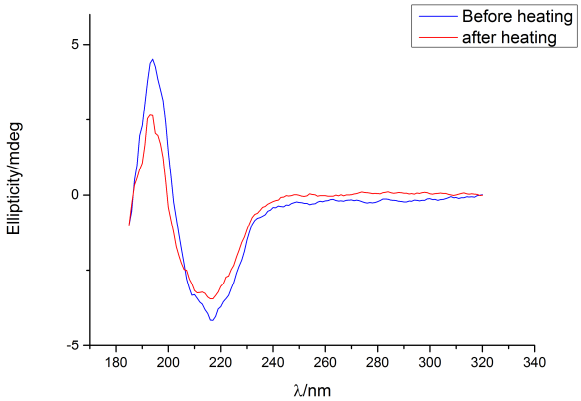

Fig. 3: Spectrum of the MIIA-Domain before heating and after heating. The general form of the spectrum stays the same.

ACKNOWLEDGEMENTS. We are grateful to Jenny Philipp for valuable biochemical and technical support.

[1] Schirrmeister, J. *et al.* (2013) *FEMS Microbiol. Lett.* **343**, 177–182.
[2] Whitmore, L. *et al.* (2004) *Nucleic Acids Res.* **32**, W668–673. (http:// dichroweb.cryst.bbk.ac.uk/html/home.shtml)

Fragment molecular orbital method for studying lanthanide interactions with proteins

S. Tsushima, Y. Komeiji,[1] Y. Mochizuki[2]

[1]National Institute of Advanced Industrial Science and Technology (AIST), Tsukuba, Japan; [2]Rikkyo University, Tokyo, Japan

The binding affinity of the calcium-binding protein calmodulin towards Eu^{3+} was studied as a model for lanthanide protein interactions in the large family of "EF-hand" calcium-binding proteins.

Modeling actinide interactions with large biomolecules by *ab initio* quantum chemical calculations requires huge computational resources. In order to overcome this restriction, we applied the fragment molecular orbital (FMO) method. In FMO, the molecular system is partitioned into small fragments. Each fragment and fragment pair is subjected to self-consistent field calculations under environmental electrostatic potentials and the electronic structure of the whole system is reconstituted.[1] This procedure drastically reduces the computational cost of Hartree Fock calculations and can be readily parallelized. FMO has been extended to MP2 to include electron correlation and was successfully applied to hydrated DNA.[2] We are currently upgrading the FMO program *Abinit-MP* to implement *f* orbitals.[3] The interaction of Eu^{3+} with calmodulin (CaM) was studied as an example.

CALCULATIONS. Using the crystal structure of Ca^{2+}-bound CaM, all four Ca^{2+} ions were replaced by Eu^{3+}, the protonation state of Eu-CaM was adjusted, and 12 Na^{+} counterions were added for neutralization. The structure was immersed in a TIP3P water bath with a minimum thickness of 8 Å around CaM and submitted to 50 ns molecular dynamics (MD) calculation using *AMBER* software. Structures at 1 ns time steps were collected. H_2O was stripped off to 4 Å coverage (Fig. 1). The 50 structures were used in FMO calculations (*Abinit-MP,* MP2 level) and their statistical averages of the inter-fragment interaction energies (IFIEs) calculated.

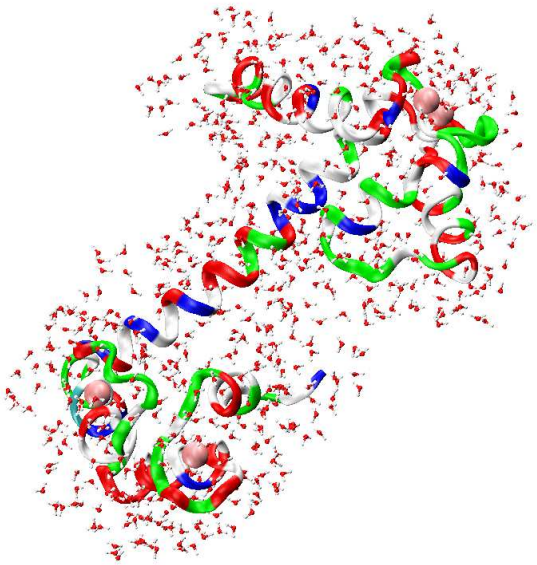

Fig. 1: MD snapshot of Eu-bound calmodulin at 50 ns simulation time from which all waters except for 4 Å layer have been stripped off (Calmodulin in ribbon, Eu in pink balls, H_2O in red-white balls). This structure was submitted to FMO calculations at the MP2 level.

RESULTS. The average coordination number (CN) of Eu^{3+} in Eu-CaM was between 8.9 and 9.1. This is consistent with known CNs of Eu^{3+} between eight and nine. Basically, Eu^{3+} binds to the same residues as Ca but with a slight increase of bidentate coordination. Additionally, increased water coordination was observed. During MD simulation, there was an average of 1.7 to 2.9 coordinating waters to Eu in Eu-CaM. This is consistent with excited state lifetime measurements using H_2O and D_2O, where an average of two coordinating waters was found in Eu-CaM.[4] When we compare the four metal-binding sites in Eu-CaM, the IFIE between Eu^{3+} and the corresponding binding site are overall similar among three of the four binding sites, namely EF Hand 1, 2, and 4. The total IFIEs are -409.9 ± 12.5, -407.5 ± 15.2, and -418.5 ± 14.1 kcal mol^{-1}, respectively. On the other hand, the IFIE for Hand 3 is -354.0 ± 14.0 kcal mol^{-1}. Clearly the EF Hand 3 is the weakest binding site whereas the others bind with almost identical affinity. The reason for this is clear; EF Hand 3 carries only three negatively charged residues, whereas the other motifs have four of them. Consequently, Eu binding in EF Hand 3 exhibits relatively larger fluctuations compared to other binding sites (Fig. 2) which causes structural disorder to Eu-CaM.

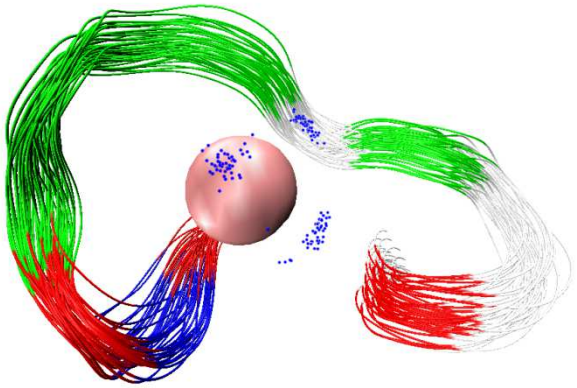

Fig. 2: Superposition 50 MD snapshot of EF Hand 3 of Eu-bound calmodulin at each 1 ns for 50 ns simulation time (Calmodulin in ribbon, Eu in pink ball, H_2O in blue dots).

ACKNOWLEDGEMENTS. We thank Dr. Sergey Samsonov at Technische Universität Dresden for his assistance during *AMBER* calculations. This project was partially funded by the Ministry of Education, Culture, Sports, Science and Technology (MEXT) of Japan.

[1] Kitaura, K. *et al.* (1999) *Chem. Phys. Lett.* **313**, 701–706.
[2] Fukuzawa, K. *et al.* (2015) *Comput. Theor. Chem.* **1054**, 29–37.
[3] Tanaka, S. *et al.* (2014) *Phys. Chem. Chem. Phys.* **16**, 10310–10344.
[4] Mulqueen, P. *et al.* (1985) *Biochem.* **24**, 6639–6645.

Comparison of U and Np uptake on biogenic and abiotic ferrihydrite by XAFS

E. Krawczyk-Bärsch, K. Schmeide, K. O. Kvashnina, A. Rossberg, A. C. Scheinost

XAS spectra of U and Np sorption biogenic ferrihydrite samples were compared to abiotic samples. The k^3-weighted χ-spectrum and its Fourier-transform of the studied biogenic ferrihydrite sample bears close resemblance to the bidentate edge-sharing innersphere sorption ^{1}E complex, which is the main sorption species on abiotic ferrihydrite. Based on the shell fit analysis, the distances of the coordination shells U–O_{eq}, U–O_{ax}, and U–Fe are similar to those determined for abiotic ferrihydrite samples.

EXPERIMENTAL. The strain of the stalk-forming, autotrophic and iron-oxidizing bacterium *Gallionella ferruginea* used in this study was isolated from a drinking-water well by MICANS (Sweden) and cultivated in our laboratory. A mineral salt solution (MSS) was prepared as described in detail.[1] The MSS medium was autoclaved, chilled to 5 °C and infused with sterile filtered CO_2 to pH 4.6–4.8. After the CO_2-infusion, tubes used as culture vessels, were filled with 10 mL MSS. Ferrous sulfide was prepared as already described and inserted to the bottom of the tube.[2] The tubes were immediately inoculated with *G. ferruginea* culture. Ferric iron was precipitating quickly and formed biogenic ferrihydrite, which was removed from the tubes. Under anaerobic conditions the biogenic ferrihydrite samples were mixed with 50 mL sterile tap water, where $UO_2(ClO_4)_2$ or NpO_2ClO_4 were added until a final U or Np concentration of 0.08 mM was obtained. At the end of the sorption experiments, the samples were ultra-centrifuged for 1 h at 187.000 × g. The formed pellets were prepared for X-ray absorption fine structure spectroscopy (XAFS) at the uranium and neptunium L_{III}–edge, which were carried out at the Rossendorf Beamline (Grenoble). The XAFS spectra were analyzed according to standard procedures.

RESULTS. The XAFS spectrum of the U sorption biogenic ferrihydrite sample is compared to those of selected references, e. g., of the bidentate edge-sharing uranyl sorption ^{1}E complex, described earlier[3] and of the aqueous tris-carbonato complex $UO_2(CO_3)_3^{4-}$. The k^3-weighted χ -spectrum and its Fourier transform of the studied biogenic ferrihydrite sample shows close resemblance to the bidentate edge-sharing inner-sphere sorption ^{1}E complex (s. Fig. 1), which is the most prominent surface species in the absence of carbonate and the main sorption species on abiotic ferrihydrite.[3] As a second species, a smaller portion of the aqueous type-B ternary uranyl-carbonato complex was determined as a result of the addition of a carbon source during the cultivation of the *G. ferruginea* strain. By iterative target test factor analysis (ITFA), using the spectra of the two endmember species, we found that the ^{1}E complex is predominant (95 %), while the ternary uranyl-carbonato complex is present only to 5 %. Based on the shell fit analysis, the distances of the coordination shells U–O_{eq} ~2.34 Å, U–O_{ax} ~1.79 Å, and U–Fe ~3.44 Å are similar to those determined of abiotic ferrihydrite samples.[4] The data of the biogenic Np ferrihydrite sample were compared to Np interaction with a hematite surface and showed similar distances of the coordination shells, also indicating a bidentate edge-sharing coordination.[5, 6] The structural parameters based on shell fit analysis of the EXAFS data

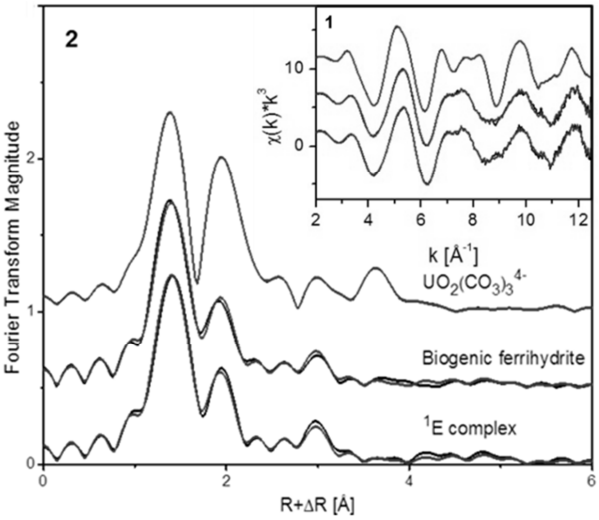

Fig. 1: U L_{III}-edge k^3-weighted XAFS spectra (1, black) and corresponding Fourier transforms (2, black) of U sorption on biogenic ferrihydrite sample, together with the bidentate edge-sharing uranyl sorption complex (^{1}E) and the aqueous tris-carbonato complex ($UO_2(CO_3)_3^{4-}$); shell fits (grey).

showed average distances of the coordination shells Np–O_{eq} ~2.44 Å, Np–O_{ax} ~1.86 Å, and Np – Fe ~3.39 Å.
The complimentary information about the electronic structure and the oxidation state of the U and Np atom at the U L_{III}- and Np L_{III}-edge, respectively, were detected by using X-ray absorption near edge structure (XANES) and the high energy resolution fluorescence detection (HERFD) mode. The position and especially its fine structure are indicative of the hexavalent uranyl and pentavalent neptunyl moiety. The "yl-shoulders" are fully expressed at about 17,175 keV and 17,630 keV, respectively, and are clearly different from the U(IV) and Np(IV) reference spectra. Hence, the spectrum gives no indication for a reduction of U(VI) and Np(V).

ACKNOWLEDGEMENTS. We acknowledge Lotta Hallbeck (MICANS, Sweden) for providing the isolated strain of *G. ferruginea.*

[1] Hallbeck, L. *et al.* (1991) *J. Gen. Microbiol.* **137**, 2657–2661.
[2] Hanert, H. (1968) *Archiv für Mikrobiologie* **60**, 348–376.
[3] Rossberg, A. *et al.* (2009) *Environ. Sci. Technol.* **43**, 1400–1406.
[4] Ulrich, K.-U. *et al.* (2006) *Geochim. et Cosmochim. Acta* **70**, 5469–5487.
[5] Müller, K. *et al.* (2015) *Environ. Sci. Technol.* **49**, 2560–2567.
[6] Amayri, S. *et al.* (2006) *Proc. of Actinide-XAS-2006 Workshop*, NEA-OECD.

Microbial reduction of uranium(VI) by anaerobic microorganisms isolated from a former uranium mine

U. Gerber, E. Krawczyk-Bärsch, T. Arnold, A. C. Scheinost

The former uranium mine Königstein (Germany) is currently in the process of controlled flooding by reason of remediation purposes. However, the flooding water still contains high concentrations of uranium and other heavy metals. For that reason the water has to be cleaned up by a conventional waste water treatment plant. The aim of this study was to investigate the interactions between anaerobic microorganisms and uranium for possible bioremediation approaches, which could be an great alternative for the intensive and expensive waste water treatment. EXAFS (extended X-ray absorption fine structure) and XANES (X-ray absorption near edge structure) measurements were performed and revealed a complete reduction of U(VI) to U(IV) only by adding 10 mM glycerol.

Despite high uranium concentrations up to 13 mg/L and a low pH of 2.9, the flooding water of the former uranium mine Königstein (Saxony, Germany) contains a high microbial diversity as detected by culture-independent methods.[1] Microorganisms are known to interact with metals and radionuclides in different ways.[2] Therefore, they can change the chemical behavior of metals and radionuclides. Anaerobic bacteria which are able to gain energy from the reduction of several metals are known to change the redox state of radionuclides as well. For instance, anaerobic sulfate-reducing bacteria (SRB) are known to reduce U(VI) to U(IV) and, thus, change the migration behavior from the highly soluble U(VI) into the less soluble U(IV).[3] To investigate the possible reduction of U(VI) within the flooding water by anaerobic microorganisms EXAFS and XANES measurements were performed.

EXPERIMENTAL. Flooding water was sampled and directly gas-flushed with N_2. 10 mM glycerol was sterile added as carbon source. The approaches (triplicates) were incubated for six weeks at 30 °C under anaerobic conditions. Samples were taken three times a week for measuring the redox potential (InLab® Redox Micro, Mettler-Toledo). Additionally, every week samples were taken to investigate the redox state of uranium. Therefore, cells were harvested by centrifugation and afterwards analyzed by U-L_{III} edge EXAFS and XANES measurements at the ROBL beamline in Grenoble. By Iterative Target-Factor Analysis (ITFA) the percentage distribution of U(VI) and U(IV) was calculated.[4]

RESULTS. During an incubation time of six weeks, the redox potential decreased from 660 mV to 300 mV. Thermodynamic calculations revealed the presence of reduced uranium at the measured redox potential (data not shown). To confirm the calculated findings EXAFS/XANES measurements were performed. The results show a change in the oxidation state of uranium after five weeks (Fig. 1). ITFA was used to calculate the percentage distribution of U(VI) and U(IV) during the six weeks of incubation (Tab. 1). After six weeks at 30 °C and under anaerobic conditions, the microorganisms were able to reduce U(VI) completely to U(IV) only in the presence of 10 mM glycerol as carbon source.

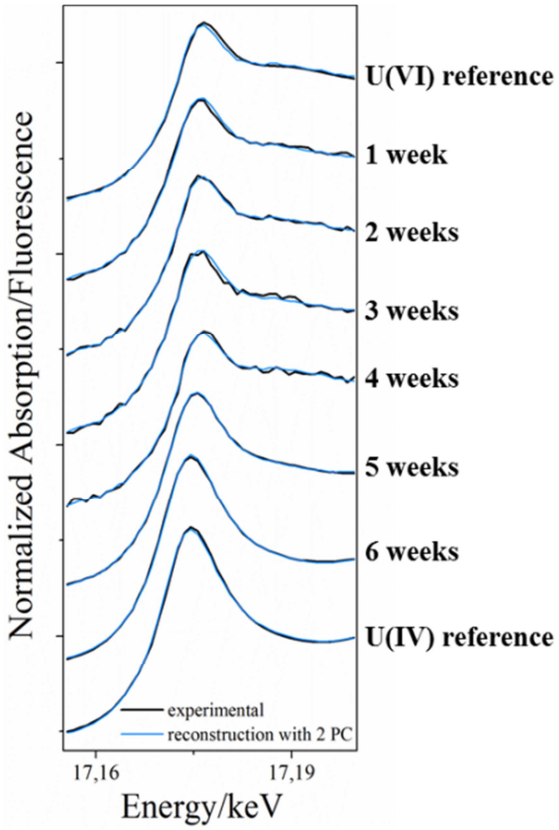

Fig. 1: EXAFS/XANES spectra of the two references and six samples.

Tab. 1: Relative uranium concentrations (in %) after XANES measurements. Calculation with ITFA.

Sample	U(VI) (%)	U(IV) (%)
U(VI) reference	100	0
1 week	100	0
2 weeks	88	12
3 weeks	97	3
4 weeks	100	0
5 weeks	48	52
6 weeks	8	92
U(IV) reference	0	100

OUTLOOK. In conclusion, the results display that anaerobic microorganisms within the flooding water are suitable for on-site bioremediation approaches which could be realized directly in the underground. Further investigations with industrial-scale setups are planned.

ACKNOWLEDGEMENTS. This work was supported by the Bundesministerium für Bildung und Forschung (BMBF), grant no. 02NUK030F (TransAqua). The authors are grateful to Frank Bok for theoretical speciation calculations.

[1] Zirnstein, I. (2015) Ph.D. Thesis, Technische Universität Dresden, Germany.
[2] Lloyd, J. R. M. (2002) *Interactions of microorganisms with radionuclides*. Elsevier Science.
[3] Lovley, D. R. *et al.* (1993) *Marine Geology* **113**, 41–53.
[4] Rossberg, A. *et al.* (2003) *Anal. Bioanal. Chem.* **376**, 631–638.

Comparison of two extreme halophilic *Halobacterium noricense* strains on DNA and protein level

M. Bader, K. Flemming, J. S. Swanson,[1] A. Cherkouk
[1]Los Alamos National Laboratory, Carlsbad, U.S.A.

Two strains of the halophilic archaeon *Halobacterium noricense* isolated from rock salt of different locations were used for interaction studies with uranium. It was found that both strains showed similar, atypical bioassociation kinetics accompanied by cell agglomeration as a stress response. The 16S rRNA gene sequences of both strains had a high similarity (> 99 %). However, differences in the whole protein pattern were apparent.

Halobacterium noricense is a halophilic archaeon commonly found in salt rock. Investigations into its bioassociation behavior with uranium have been conducted with two different strains. *Halobacterium noricense* DSM-15987 was isolated from an Austrian salt mine[1] and *Halobacterium* putatively *noricense* WIPP strain was isolated from the salt basin in New Mexico, U.S.A.,[2] which hosts the Waste Isolation Pilot Plant (WIPP) – a final repository for transuranic waste. Exposure of both strains to uranium over time resulted in similar multistage bioassociation kinetics and an increase in cell agglomeration.[3] Nevertheless, small differences were apparent, especially regarding the size of the agglomerates (Fig. 1). Hence, a comparison of the strains at the DNA and protein level is of interest.

EXPERIMENTAL. Both *H. noricense* strains were cultivated in DSM372 medium in the dark with shaking at 30 °C. Cells were harvested in the mid exponential phase and washed three times with 3 M NaCl, pC_{H+} 6.0 (corrected pH due to high ionic strength).[4]
Bioassociation. A defined amount of cells (5 mg dry biomass) was resuspended in 10 mL of filter-sterilized 3 M NaCl solution with 100 µM uranium adjusted to pC_{H+} 6. After 48 h, cells were washed (3 M NaCl, pC_{H+} 6) and a staining with the LIVE/DEAD® BacLight™ Bacterial Viability Kit L7012, Molecular Probes™, Inc., Eugene, OR, U.S.A. was performed.
Protein level. To compare both strains on a protein level, sodium dodecyl sulfate polyacrylamide electrophoresis (SDS-PAGE), using a 10 % polyacrylamide separation gel, was performed.[5] The gels were loaded with an amount of cells corresponding to 0.1 mg dry biomass and stained with colloidal Coomassie brilliant blue.
DNA level. For comparison on a DNA level, washed cells were lysed in water to exclude the high content of NaCl before an *in situ* polymerase chain reaction (PCR) was performed. Therefore, the Arch 21f and Arch 958r primer were used.[6] The amplified product was purified (QuickStep™2 PCR Purification Kit, Edge Bio, BD) and sequenced from GATC Biotech AG.

RESULTS. The 16S rRNA gene sequences of both *H. noricense* strains have a 99.9 % similarity. Out of 853 bases only one was different. At this position, DSM-strain has an A and the WIPP strain a G. Interestingly, the G in this position is also present in other isolates belonging to the genus of *Halobacterium*. The archaeon isolated from the WIPP shows a 100 % similarity in 835 bases of the 16S rRNA gene sequence of *Halobacterium* sp. YI80-2 isolated from Yunying salt mine in Hubei Province, China.[7]

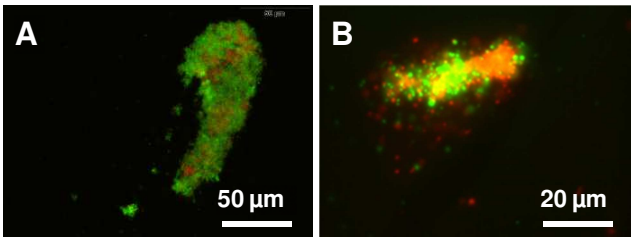

Fig. 1: Fluorescence micrographs of *H. noricense* cells incubated with uranium (100 µM) for 48 h, at pC_{H+} 6. Red fluorescence shows dead cells, green fluorescence living cells. *H. noricense* DSM-15987 (A) and *H. noricense* WIPP (B).

Differences between *H. noricense* DSM-15987 and *H. noricense* isolated from the WIPP are particularly apparent in the whole protein pattern (Fig. 2). Due to the fact that the same amount of biomass was loaded to the gel, a direct comparison is possible. It can be seen that bands are not only different in their intensity (Fig. 2, white arrow) but also different in size. For example, the WIPP-strain shows an additional band at 78 Da (Fig. 2, gray arrow). Other bands are only shifted, like the one at 50 Da, which is shifted to 53 Da for the DSM-strain (Fig. 2, black arrow). No difference in protein pattern of samples exposed to uranium for up to three weeks (data not shown) were visible. Further proteomics analyses are ongoing.

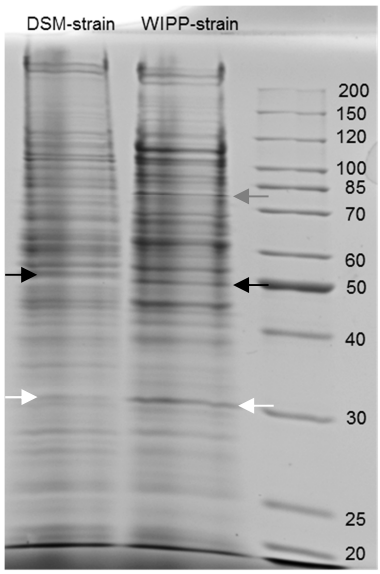

Fig. 2: SDS-PAGE image of the whole protein pattern of both *H. noricense* strains.

In conclusion, despite the fact that both investigated strains show the same atypical bioassociation kinetics,[3] differences on DNA and protein level exist.

ACKNOWLEDGEMENTS. The authors would like to thank M. Dudek and S. Kluge for the preparation of the SDS-PAGE gels.

[1] Gruber, C. *et al.* (2004) *Extremophiles* **8**, 431–439.
[2] Swanson, J. S. *et al.* (2012) *Report LA-UR-12-22824*, p. 1.
[3] Bader, M. *et al.* (2017) *J. Hazard. Mater.* **32**, 225–232.
[4] Borkowski, M. *et al.* (2009) *Report LA-14360*, p. 26–27.
[5] Laemmli, U. K. (1970) *Nature* **227**, 680–700.
[6] DeLong, E. F. (1992) *Proc. Natl. Acad. Sci. USA* **89**, 5685–5689.
[7] Jaakkola, S. T. *et al.* (2014) *PLoS ONE* **9**, e110533.

Isolation and characterization of extreme halophilic archaea

M. Franze, A. Cherkouk

Extreme halophilic archaea from the family *Halobactereacea* represent a dominant part of the microbial community present in saline soils as well as rock salts. By using a culture-dependent approach different Haloarchaea could be isolated and were phylogenetic analysed. Interestingly, isolates closely related to different *Halobacterium* spp. were found in both environments.

Salt rock formations are considered as potential host rock systems for the long-term storage of highly radioactive waste in a deep geological repository. To date, little is known about the habitat salt rock and the way of life of the microorganisms occurring there. Next to bacteria and fungi, extreme halophilic archaea are dominating this habitat. It is of interest to know what kind of extreme halophilic archaea are living there, how active they are under repository relevant conditions, and how these microorganisms can influence the safe storage of the waste. So far, microbial investigations regarding the disposal of radioactive waste in salt rock were only carried out in the WIPP (Waste Isolation Pilot Plant) in Carlsbad, New Mexico, U.S.A.[1] Furthermore, recently an extremely halophilic archaeon termed *Halobacterium noricense* was also isolated from the WIPP site, which is phylogenetic closely related to another *Hbt*. strain DSM-15987 isolated from a salt mine in Austria.[2]

EXPERIMENTAL. The microbial diversity in salt rock from Gorleben as well as saline soil sample from Arava Desert, Israel, was examined with culture-dependent methods. The latter was investigated in order to get experiences in different approaches to isolate halophilic archaea and to develop new methods to get isolates from our salt rock samples from Gorleben. A specific portion of the samples were incubated at room temperature in three different sodium chloride con-centrations (2 M, 3 M and 4 M) of modified R2A resuscitation buffer.[3] After 24 h incubation time, 300 µL of the respectively mixtures were spread on corresponding agar plates containing modified R2A medium and adapted for halophilic microorganisms and were incubated at 37 °C in the dark.[4] Selected colonies were transferred to new plates and afterwards in MR2A liquid medium to get individual isolates. For phylogenetic characterization of the obtained isolates, the 16S rRNA gene was amplified by *insitu* PCR of the genomic DNA from cells lysed in purified water. The gene encoding 16S rRNA was amplified by PCR with the primer 21f and the reverse primer 958r[5] were used for the PCR and the amplifications were performed with 30 cycles, each of which consisted of denaturation for 1 min at 94 °C, annealing for 1 min at 55 °C, and polymerization for 2 min at 72 °C. The purified PCR products were Sanger sequenced by GATC Biotech. The 16S rRNA gene sequences were aligned using ClustalW and the phylogenetic tree was constructed with MEGA 7 using the maximum-likelihood algorithm.[6]

RESULTS. With the chosen approach extreme halophilic archaea could be isolated from both kinds of samples. Differences were obvious in time when first visible colonies appeared and in amount of colonies. From the saline soil sample much more colonies, which differ in shape and color, were visible after two weeks, whereas from salt rock sample only five colonies appeared after two months. After transferring individual colonies to new plates and subsequently cultivation in liquid MR2A medium, the isolates were further characterized by 16S rRNA gene analysis. The gene sequences obtained from respective isolates were compared with the sequences of the NCBI database by means of BLAST algorithm[7] to get the phylogenetic closest relatives (Fig. 1).

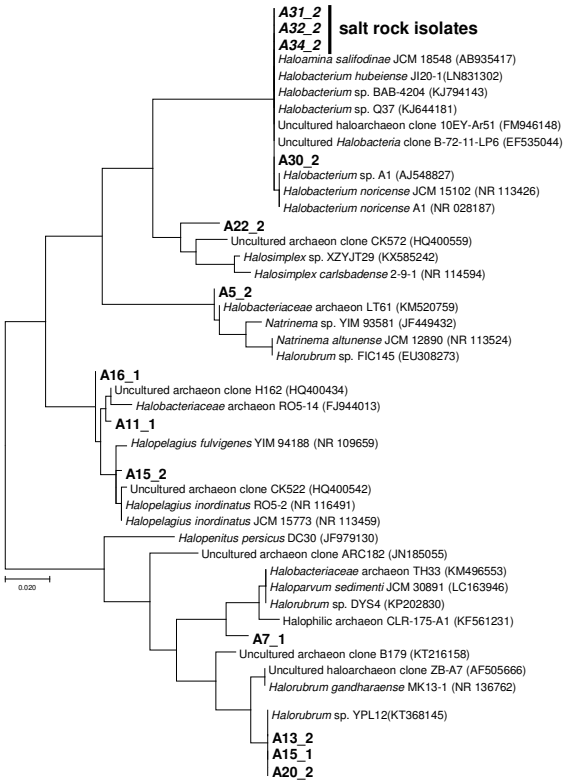

Fig. 1: Phylogenetic dendrogram showing the position of isolated haloarchaeal species from two different time points of isolation (1,2) based on 16S rRNA gene sequences. The sequence data used were obtained from the NCBI database. Bar: 2 % sequence divergence.

The isolates of the saline soil sample can be assigned to different genera *Natrinema, Halorubrum, Halopelagius, Haloamina* and *Halobacterium*. The closest relative of the isolates from the salt rock is with a sequence similarity of more than 99 % *Halobacterium hubeiense* JI20-1, which was isolated from a 123 million years old core from a salt mine in Qianjing, China.[8] One isolate of the soil sample namely A30_2 was also closely related to the same species with 99 % sequence similarity. Furthermore, *H. hubeiense* has a high sequence similarity to *H. noricense*, which was isolated from the WIPP (Fig. 1). Therefore, the obtained isolates could be used for further investigations, e. g. experiments under repository relevant conditions as high temperature and radiation as well as interactions with radionuclides.

[1] Swanson, J. S. *et al.* (2012) *Statusreport Los Alamos National Laboratory LA-UR-12-22824*, p. 1.
[2] Gruber, C. *et al.* (2004) *Extremophiles* **8**, 431–439.
[3] Jankowski, U. (2009) *Report FZD-511*, p. 35.
[4] Robinson, J. L. *et al.* (2005) *J. Bacteriol.* **187**, 923–929.
[5] DeLong, E. F. (1992) *Proc. Natl. Acad. Sci. USA* **89**, 5685–5689.
[6] Kumar, S. *et al.* (2016) *Mol. Biol. Evol.* **33**, 1870–1874.
[7] Altschul, S. F. *et al.* (1990) *J. Mol. Biol.* **215**, 403–410.
[8] Jaakkola, S. T. *et al.* (2016) *Environ. Microbiol.* **18**, 565–579.

Molecular interactions of *Leucoagaricus naucinus* with uranium(VI) and europium(III)

A. Wollenberg, A. Günther,[1] J. Raff

[1]Helmholtz Institute Freiberg for Resource Technology, Freiberg, Germany

With regard to a molecular understanding of the interaction of fungal mycelium with radionuclides and its possible application for precautionary radiation protection and bio-remediation, the binding mechanism of the radionuclide uranium and the metal europium, as surrogate for trivalent actinides, where investigated with different starting conditions by the living fungal cells of *Leucoagaricus naucinus*.

EXPERIMENTAL. *L. naucinus* was cultivated in the complex medium 90 (malt extract 30 g/L and soya peptone 3 g/L). The fungal biomass was harvested by washing with sterile minimal medium ($MgSO_4$ 19,5 mg/L, $FeCl_3$ 2,4 mg/L, K_2HPO_4 0,9 mg/L) and filtration.
For binding experiments the minimal medium with uranium or europium was added to the fungal biomass and was shaken at 100 rpm. The standard conditions of the experiments were at pH 5, with the contact time of 48 h, an initial metal concentration of about 50 mg/L and dry fungal biomass of 312 mg/L. To study the influence of the starting conditions to the binding mechanism, the pH-value and the initial metal concentration were changed.

RESULTS. *L. naucinus* shows a different binding behavior and binding capacity for U(VI) in comparison to Eu(III), depending on pH-value (see Fig. 1). The results proved the binding capacities of both metals are different except at pH 4. At this pH value, the binding capacities of uranium and europium are similar. At pH 5 and 6, much more U(VI) is bound in comparison to Eu(III). The experiments also indicate a different binding behavior of uranium and europium. This is based on the fact that uranium binding is more efficient at higher pH-values, whereas the europium binding seems to be independent of pH what goes along with the different speciation of U(VI) and Eu(III).
Furthermore, the change of the calcium ion concentration was investigated. Figure 2 shows that more Ca^{2+} is released with europium binding in comparison to uranium binding. These results indicate an exchange of Ca^{2+} by Eu^{3+} at Ca binding sites of the fungal biomass. Due to the similar ion radius of Eu^{3+} (0.95 Å) and Ca^{2+} (0.97 Å) the fungal cell could not differentiate between this two cations. This binding mechanism was also assumed by studies of the groups

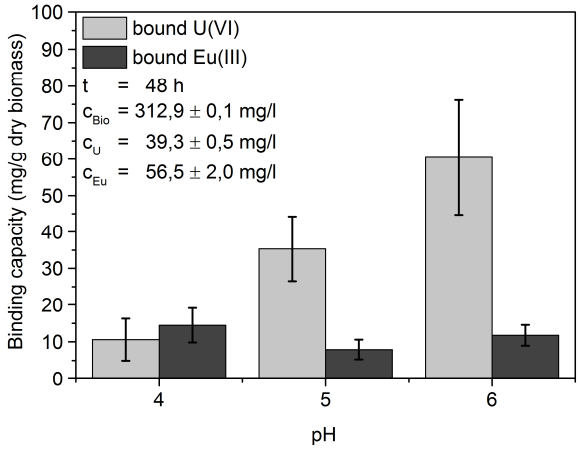

Fig. 1: Binding capacities of *L. naucinus* for uranium and europium influenced by pH 4–6.

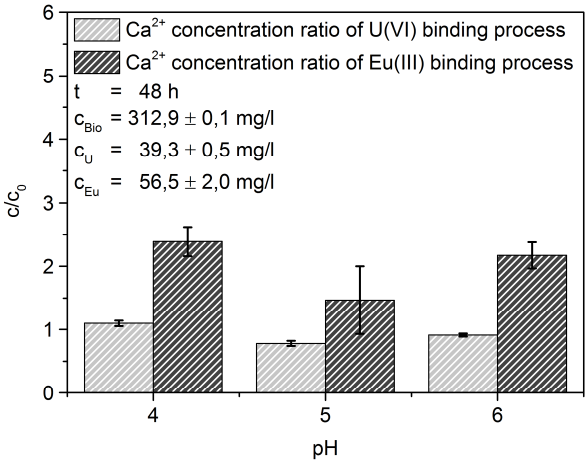

Fig. 2: Ca^{2+} concentration ratio in the solution after the binding experiments with uranium and europium.

of Liao or Diniz.[1, 2]
Additionally, the initial metal concentration was changed for the experiments to investigate the binding mechanism following the Langmuir model, which is given by the linearized equation 1.

$$\frac{1}{q} = \frac{1}{K_L \cdot q_{\max}} \cdot \frac{1}{c_{eq}} + \frac{1}{q_{\max}} \qquad (1)$$

This equation describes the connection between the metal concentration in the fungal mycelium (q) and the metal equilibrium concentration (c_{eq}) to calculate the maximal binding capacities (q_{max}) and the affinity of the metal to the ligand (K_L). The results of this calculation are given in Tab. 1.

Tab. 1: Langmuir isotherm constants for U(VI)- and Eu(III)- binding by *L. naucinus*.

Metal	Langmuir constant (K_L)	Max. binding capacity (q_{max})
Uranium(VI)	0.06	144.93
Europium(III)	0.12	17.51

Table 1 shows that *L. naucinus* bound eight times more U(VI) than Eu(III) with a lower affinity. Consequently, the Langmuir constants confirmed previous results, which indicates an specific ion exchange mechanism for Eu(III) and a less specific binding for U(VI). This unspecific binding results also in a higher amount of bound uranium.

ACKNOWLEDGEMENTS. The project BioVeStRa was funded by BMBF. The authors also thank the FWO analytics team for elemental analyses.

[1] Liao, J. *et al.* (2008) *J. Radioanal. Nucl. Chem.* **227**, 329–336.
[2] Diniz, V. *et al.* (2005) *Water Res.* **39**, 239–247.

Influence of U(VI) on the metabolism of plant cells studied by microcalorimetry and TRLFS

S. Sachs, K. Fahmy, J. Oertel, G. Geipel, F. Bok

Uranium(VI) shows a concentration-dependent influence on the metabolic activity of plant cells. With increasing U(VI) concentration, the predominant U(VI) species in medium R_{red} changes from UO_2HPO_4(s) to $(UO_2)_3(OH)_5^+$, which may affect the bioavailability of U(VI).

Knowledge of the radionuclide transfer in the environment including the food chain is the basis for the reliable risk assessment for humans. The interaction of plants with heavy metals impacts their metabolism. For instance, plants segregate metal chelates into the rhizosphere, store metal chelates in vacuoles or synthesize protective metabolites.[1] We studied the interaction of U(VI) with canola cells (*Brassica napus*) focusing on the concentration-dependent impact of U(VI) on the cell metabolism. Isothermal microcalorimetry was used to monitor the metabolic heat flow. The cell viability was studied using the MTT test.[2] The speciation of U(VI) in the nutrient medium was determined by time-resolved laser-induced fluorescence spectroscopy (TRLFS) and thermodynamic modeling to correlate the impact of U(VI) on the cell activity with its speciation.

EXPERIMENTAL. Starting from a callus cell culture (P-1113, DSMZ), suspension cultures of *Brassica napus* cells were grown in medium R[3] at room temperature on a gyratory shaker. Isothermal microcalorimetry was performed with a TAM III instrument (Waters GmbH)[4] to continuously monitor the metabolic heat flow produced by the cells in the absence or presence of U(VI) at 25 °C for up to 311 h. Wet cells (0.3 g) were transferred into glass ampoules and 2 mL of medium R with a reduced phosphate concentration of 1.25×10^{-5} mol/L (medium R_{red}; pH 5.8) were added. To study the impact of U(VI) on the cell metabolism, U(VI) was added in form of a $UO_2(NO_3)_2$ stock ($[U(VI)]_{final}$: 2×10^{-5}–2×10^{-4} mol/L). After the microcalorimetric experiments, the cell viability was determined by the MTT test.[2] The U(VI) speciation in medium R_{red} was studied by time-resolved laser-induced fluorescence spectroscopy (TRLFS) using a Nd-YAG pumped OPO systems (Newport-Spectra Physics)[5] and calculated by thermodynamic modeling (Geochemist's Workbench).[6]

RESULTS. Figure 1 illustrates the metabolic heat flow of the cells at different U(VI) concentrations. It decreases with increasing U(VI) concentration indicating a decrease of the metabolic cell activity. Based on these data the "metabolic endurance", which represents the product of the metabolic power and the total released heat, was derived (inset Fig. 1). The maximum values obtained at different U(VI) concentrations were normalized to the value determined in the absence of U(VI). These data were compared to the cell viability data measured by MTT test, which is based on the activity of mitochondrial and cytosolic dehydrogenases of living cells (Fig. 2). Both the heat flow data and the cell viability data decrease with increasing U(VI) concentration and agree very well. TRLFS results show that UO_2HPO_4 (s) dominates the U(VI) speciation at 2×10^{-5} mol/L U(VI) in medium R_{red} (pH 5.8), which is confirmed by thermodynamic modeling. With rising U(VI) concentration, the U(VI) speciation changes continuously and is dominated by U(VI) hydroxo

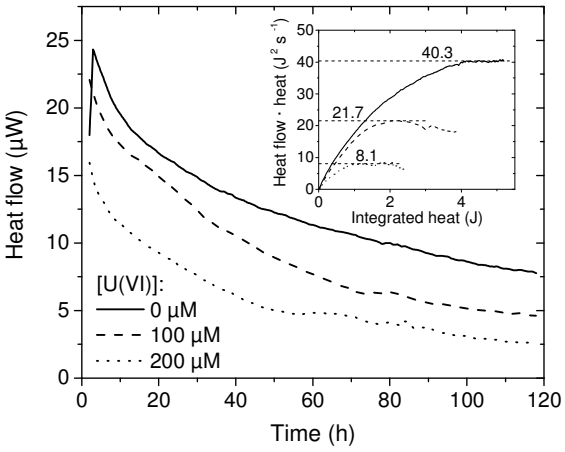

Fig. 1: Heat flow of the cells at different U(VI) concentrations and derivation of the "metabolic endurance" (inset).

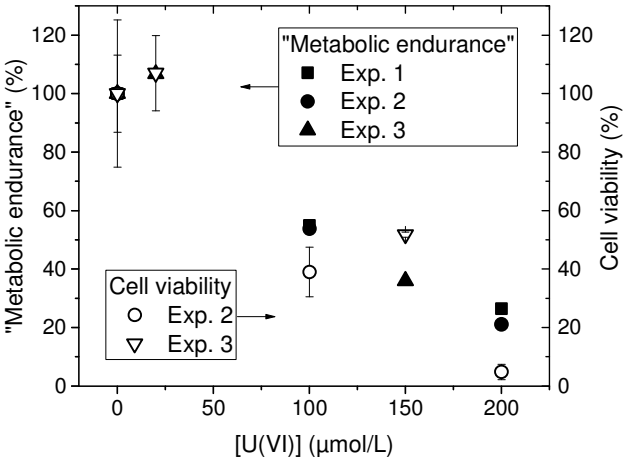

Fig. 2: Comparison of the normalized "metabolic endurance" with the cell viability measured by the MTT test.

complexes. At $[U(VI)] \geq 1\times10^{-4}$ mol/L, the speciation is predominated by the $(UO_2)_3(OH_5)^+$ complex (60–65 % of total U(VI)). In addition to the total amount of U(VI), the decrease of the cell metabolism may be attributed to the change of the U(VI) speciation in solution, which can affect its bioavailability.

Isothermal microcalorimetry is a highly sensitive real-time monitor of the concentration and probably speciation-dependent U(VI) toxicity in *Brassica napus* cells. The metabolic response of the plant cells correlates very well with their mitochondrial activities. This opens further possibilities to study low dose effects of U(VI) using different isotopes in calorimetric experiments.

ACKNOWLEDGEMENTS. The authors thank M. Obeid, J. Seibt, S. Heller, J. Philipp, and S. Gurlit for experimental support.

[1] Weiler, E., Nover, L. (2008) *Allgemeine und molekulare Botanik*, Thieme, Stuttgart.
[2] Mosmann, T. J. (1983) *J. Immunol. Meth.* **65**, 55–63.
[3] www. dsmz. de/fileadmin/downloads/PC/medium/R. pdf.
[4] Obeid, M. H. *et al.* (2016) *Appl. Environm. Microbiol.* **82**, 3563–3571.
[5] Geipel, G. *et al.* (2015) *Biometals* **28**, 529–539.
[6] Bethke, C. M. (2011) *Geochemical and biogeochemical modeling*, 2nd ed., Cambridge University Press, Cambridge.

First insights in the Eu(III) speciation in plant cell suspension cultures

H. Moll, S. Sachs

More than 80 % of the initial Eu(III) amount was associated on *Brassica napus* cells after an incubation time of 24 h. The spectroscopic speciation of the cell-bound Eu(III) is characterized by an increased intensity of the $^7F_2$ transition and prolonged luminescence lifetimes.

A detailed knowledge of the fate of radionuclides in the ecosphere including the food chain requires an improved understanding of the underlying processes. Our aim is to explore the complex interaction processes of trivalent actinides with plant cells on a molecular level. The first approach was to apply europium(III) as an analogue for trivalent actinides. We studied the interaction of Eu(III) with *Brassica napus* cell suspensions by the direct speciation technique time-resolved laser-induced fluorescence spectroscopy (TRLFS). The possible release of plant cell metabolites promoted due to the cell contact with Eu(III) was investigated according to the procedure described earlier.[1]

EXPERIMENTAL. Suspension cultures of *Brassica napus* cells were grown in medium R (DSMZ) as already described.[2] Seven days before contacting the cells with Eu(III), the cells were transferred in medium $R_{red.}$ (phosphate concentration reduced to 1 %). Cells were incubated with 30 µM Eu(III) at pH 5.8 for 24 or 168 h. The Eu(III) loaded cells were washed, diluted, and re-suspended in 0.154 M NaCl prior to the TRLFS measurements. The relative peak intensity ratio ($R_{E/M}$) was defined as: $R_{E/M} = I_2$ ($^5D_0 \rightarrow {}^7F_2$) / I_1 ($^5D_0 \rightarrow {}^7F_1$), where I_1 and I_2 were calculated from the peak areas. Experimental details about the laser system can be found in literature.[3] The cell viability was investigated using the MTT test.[4]

RESULTS. The luminescence properties of 30 µM Eu(III) in medium $R_{red.}$ are dominated by an increased $R_{E/M}$ value of 2.0 (0.5 for Eu(III) in 0.154 M NaCl) and the luminescence decay changes to bi-exponential: $\tau_1 = 112$ fixed and $\tau_2 = 240 \pm 5$ µs ($\tau = 113 \pm 2$ µs for Eu(III)) (cf. Fig. 1). Based on measurements with different medium components, the inorganic salts (12 wt.-%) and FeNaEDTA (0.1 wt.-%) showed the highest impact on the luminescence spectrum measured in medium $R_{red.}$.
After 24 h of incubation time, 80 % of the initial Eu(III) was sorbed on the cells. The MTT test showed that the cells were metabolically active after Eu(III) exposure.

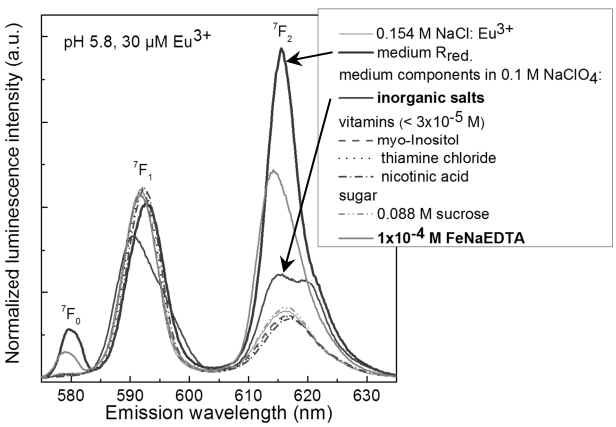

Fig. 1: Luminescence spectra of Eu(III) in medium $R_{red.}$ and different medium components.

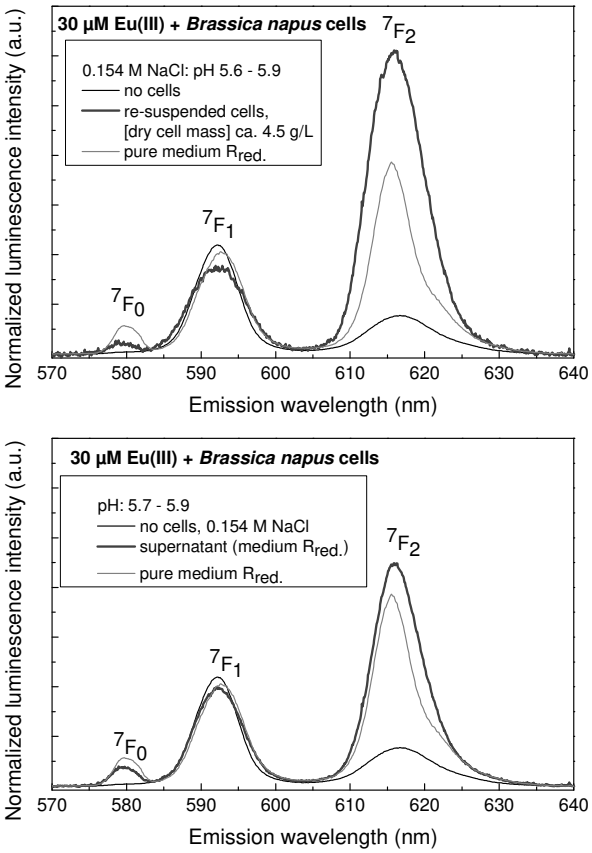

Fig. 2: Luminescence spectra of Eu(III): Eu(III) associated on *Brassica napus* cells (top) and Eu(III) complexed in the corresponding supernatant (bottom).

The Eu(III) associated on plant cells is characterized by an enlarged $R_{E/M}$ value of 3.4 (2.0 in pure medium). This indicates an increase in the interaction strength of Eu(III) towards the plant cells compared with pure medium. Bi-exponential luminescence decay: $\tau_1 = 155 \pm 40$ and $\tau_2 = 515 \pm 50$ µs (e. g. Eu(III)-*B. napus* species) was detected. By comparing these results with Eu(III) speciation experiments with planktonic bacterial cells (e.g. *Sporomusa* sp.),[5] τ_1 and τ_2 might indicate an interaction of Eu(III) with carboxyl and phosphoryl functionalities of the plant cells, respectively. The spectral shape of the Eu(III) containing supernatant is similar to those of the pure medium. However, a higher $R_{E/M}$ value of 2.4 (pure medium: 2.0) and a slightly prolonged lifetime of the second component $\tau_2 = 260 \pm 35$ µs (pure medium: 240 µs, respectively) might indicate the release of complexing metabolites by the cells. Further studies will focus on the determination of the complexing cell metabolites, callus cell growth experiments in the presence of Eu(III) and the determination of Eu(III) in cell compartments after cell fractionation.

ACKNOWLEDGEMENTS. The authors thank J. Seibt for cell cultivation and technical support and S. Gurlit for ICP-MS measurements.

[1] Sachs, S. (2016) *Report HZDR-067*, p. 54.
[2] Geipel, G. *et al.* (2015) *Biometals* **28**, 529–539.
[3] Moll, H. *et al.* (2008) *Biometals* **21**, 219–2289.
[4] Mosmann, T. (1983) *J. Immunol. Meth.* **65**, 55–63.
[5] Moll, H. *et al.* (2014) *Geomicrobiol. J.* **31**, 682–696.

Radiolabeling as a tool to study uptake pathways in plants

S. Schymura, T. Fricke,[1] H. Hildebrand, K. Franke
[1]Vita34 BioPlanta, Leipzig, Germany

The identification of major uptake pathways in plants is an important factor when evaluation the fate of manufactured nanoparticles in the environment and the associated risks. Using different radiolabeling techniques we were able to show a predominantly particulate uptake for CeO_2 nanoparticles (NPs) in contrast to a possible uptake in the form of ionic cerium.

EXPERIMENTAL. For radiolabeling CeO_2 NPs were irradiated with 17.6 MeV protons at the in-house cyclotron to form [^{139}Ce]CeO_2 NPs *via* a (p,2n) nuclear reaction from ^{140}Ce to ^{139}Pr with consequent decay of the ^{139}Pr to ^{139}Ce. In a different approach, CeO_2 NP were radiolabeled to also form [^{139}Ce]CeO_2 by in-diffusion of ionic $^{139}Ce^{3+}$ at a temperature of 300 °C.
For the plant uptake studies, ryegrass and sunflowers were exposed to [^{139}Ce]CeO_2 NPs in a hydroponic setup using tap water with 5 mg/L fulvic acid added for 24–96 h under shaking. After exposure, the plants were harvested and the activity measured.

RESULTS. Using our methods, we were able to isotopically radiolabel CeO_2 NPs with ^{139}Ce at activity concentration of about 1 MBq/mg allowing a detection of the NPs in the ng/L range (Tab. 1). The particle size distribution and zeta-potential was retained for both methods and the radiolabel proved to be stable in an environmentally relevant pH range. However, at lower pH the differently labeled particles showed a distinctly different activity release kinetic, the in-diffusion-labeled NPs releasing a 70 times higher activity than the activated particles indicating a surface labeling in case of the in-diffusion labeled particles.

Tab. 1: Radiolabeling yields and detection limits for the different methods.

Method	Activity concentration	Detection limit*
In-diffusion	0.925 MBq/mg	52 ng/L
Activation	1.242 MBq/mg	41 ng/L

*: Wallac 1480 WIZARD 3" gamma counter.

This allowed us to use the so-labeled particles to track the role of dissolution phenomena in plant uptake of cerium stemming from manufactured CeO_2 NPs. If dissolution plays a major role in uptake or translocation, different activity uptake rates will be observed when comparing experiments with either one of the labeled particles.
However, using ryegrass we did not detect significant differences in uptake into the roots nor translocation into the shoots (Fig. 1 & 2) proving a predominantly particulate transfer pathway. Furthermore, autoradiographic imaging of leafs of an exposed sunflower showed accumulation of the CeO_2 NPs in the leaf veins and edges (Fig. 3) indicating a particulate uptake and consequent translocation along the water stream inside the plant.[1]

ACKNOWLEDGEMENTS. We gratefully acknowledge funding by the BMBF within the NanoNature program (FKZ: 03X0144A).

[1] Schymura, S. *et al.* (2017), in preparation.

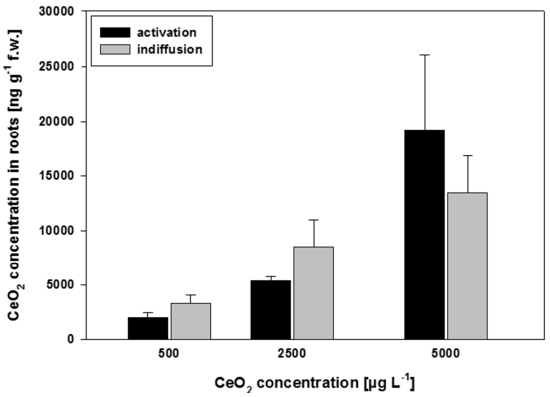

Fig. 1: Uptake of CeO_2 in roots of ryegrass in dependence of exposure concentration and radiolabelling method.

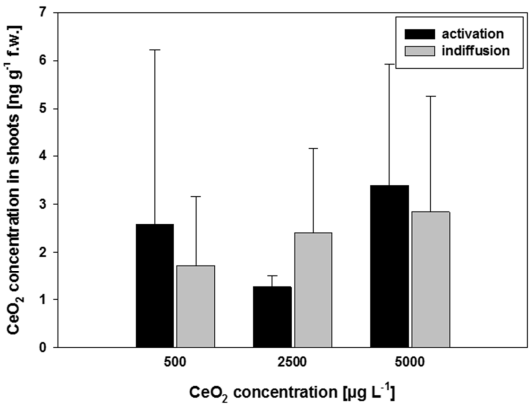

Fig. 2: Translocation of CeO_2 into shoots of ryegrass in dependence of exposure concentration and radiolabelling method.

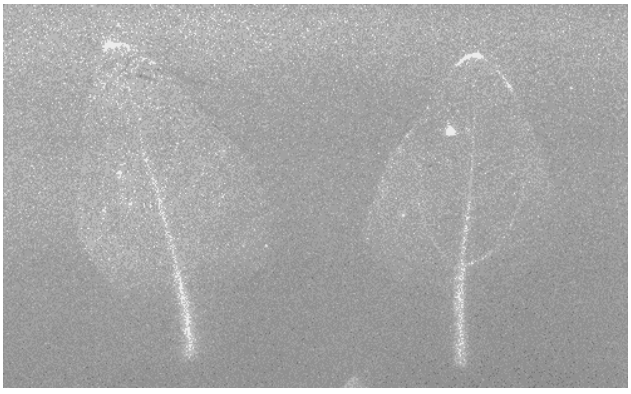

Fig. 3: Autoradiographic imaging of [^{139}Ce]CeO_2 accumulation in sunflower leaf veins and edges.

Bentonite – Geotechnical barrier and source for microbial life

N. Matschiavelli, J. Steglich, S. Kluge, A. Cherkouk

Due to their properties, namely a high swelling capacity and a low hydraulic conductivity, Bentonites fulfil as geotechnical barrier a sealing and buffering function in the nuclear waste repository. Depending on the mineral composition Bentonites contain many suitable electron-donors and -acceptors, enabling potential microbial life. For the potential repository of highly radioactive waste the microbial mediated transformation of Bentonite could influence its properties as a barrier material. Microcosms were set up containing Bentonite and anaerobic synthetic Opalinus-clay-pore water solution under an N_2/CO_2-atmosphere to elucidate the microbial potential within selected Bentonites. Substrates like acetate and lactate were supplemented to stimulate potential microbial activity. First results show that bentonites represent a source for microbial life, demonstrated by the consumption of lactate and the formation of pyruvate. Furthermore, microbial iron-reduction was determined, which plays a crucial role in Betonite-transformation.

EXPERIMENTAL. Microcosm-experiments were set up by applying 20 g Bentonite B36 (processed Bentonite) with 40 mL sterile synthetic Opalinus-clay-pore water solution (212 mM NaCl, 26 mM $CaCl_2$, 14 mM Na_2SO_4, 1.6 mM KCl, 17 mM $MgCl_2$, 0.51 mM $SrCl_2$ and 0.47 mM $NaHCO_3$, degassed for 1.5 h with a N_2/CO_2 gas mixture (80/20) while stirring). Selected microcosms were supplemented with organic substrates (50 mM acetate/lactate, 3 mM methanol, 0.1 mM AQDS). The microcosms were incubated at 30 °C in the dark without shaking and during a period of 98 days samples were analyzed. All procedures were carried out under anaerobic conditions. Sensory measurement of O_2-concentration, redox potential and pH-value were performed within portions of the respective, well-mixed suspensions. For iron-determination the Ferrozine-method based on a modified protocol by Viollier was applied to the cleared supernatant after digestion of the suspension with 0.5 M HCl for 30 min.[1] The centrifuged and filtrated supernatant of the suspension was used for determining sulfate-concentration *via* IC and lactate- and acetate-concentration *via* HPLC. For analyzing the microbial diversity within the respective sample, DNA was extracted using a protocol from Selenska-Pobell.[2] For sequencing, the 16S rDNA was amplified by using oligonucleotides 28f/519r.[3]

RESULTS. In order to analyze microbial effects on Bentonite-transformation, we analyzed different geochemical and biological parameters over a period of 98 days. No significant changes in O_2-concentration, pH-value or sulphate concentration could have been detected (data not shown).
Only substrate-containing microcosms showed significant changes in geochemical and biological parameters. Here, a significant decrease in redox potential from 505 mV to 270 mV was demonstrated (data not shown). Furthermore, HPLC-analysis of the supernatant showed a decrease in lactate- and an increase in acetate-concentration. Surprisingly, an additional metabolite, namely pyruvate, was formed and secreted. Thus, we were able to show that indigenous microbes are able to metabolize the provided carbon sources. Strikingly, a reduction of Fe(III) to Fe(II) has been observed (Fig. 1), demonstrating that in Bentonite contained iron

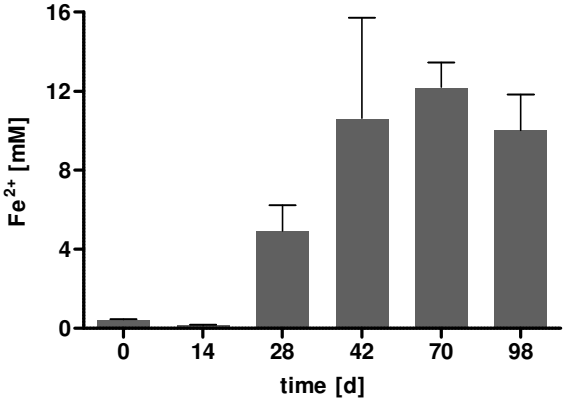

Fig. 1: Microbial influence on Fe^{2+}-concentration within the Bentonite B36. Iron determination was carried out according to a modified Ferrozine-method based on Viollier *et al.*[1] Shown are mean values with standard deviations from at least two independent experiments conducted in duplicates.

serves as a potential electron-acceptor for microbial anaerobic respiration and, thus, showing that microbial metabolism could affect the structure of Bentonite directly, which has to be elucidated in structural analysis.
First analysis of the microbial composition within Bentonite B36 showed that bacteria from the genus of *Bacillus* and *Saccharopolyspora* were and/or became very dominant in microcosms containing substrates. Both genera are known for spore-formation, which enable the respective organisms to outlast during environmental and nutritional stresses. Mature endospores of *Bacillus* and other related genera are resistant to heat, UV and γ-radiation treatments even if the respective exposure lasts years.[4] Colonization starts again when environmental conditions are favorable. It has already been shown that *Bacilli* are able to reduce iron(III).[5]
Our results evidence the occurrence of metabolic active microbes in Bentonites under ideal conditions. Organic acids are metabolized and furthermore converted to other organic acids serving as potential substrates for other microbes. Thus, our results reveal the importance of the selection of the best suitable Bentonite in order to avoid transformation by indigenous microbes. By using a Bentonite containing only low organic carbon and low iron, microbial activity during deposition of highly radioactive waste can be avoided or retarded.

ACKNOWLEDGEMENTS. We thank Falk Lehmann, Jana Seibt and Susanne Sachs for HPLC-analysis and Carola Eckardt for IC-measurements. Furthermore, we thank Stephan Kaufhold (BGR, Hannover, Germany) for providing the Bentonites. This work was supported by the Federal Ministry for Economic Affairs (No. 02E11344B).

[1] Viollier, E. *et al.* (2000) *App. Geochem.* **15**, 785–790.
[2] Selenska-Pobell, S. (1995) *MMEM.* **1.5.1.**, 1–17.
[3] Lopez-Fernandez, M. *et al.* (2015) *Microb. Ecol.* **4**, 922–935.
[4] Checinska, A. *et al.* (2015) *Annu. Rev. Food Sci.* **6**, 351–369.
[5] Hobbie, S. N. *et al.* (2012) *Syst. Appl. Microbiol.* **35**, 226–232

The potential of amino acids in alkaliphilic bioleaching

R. Barthen, L. Karimzadeh, M. Gründig, J. Heim,[1] K. Franke, J. Lippmann-Pipke
[1]Technische Universität Bergakademie Freiberg, Freiberg, Germany

Bioleaching has become a major production process for copper contributing currently to around 15 % of the world wide copper production. However, non-sulfidic and/or complex ores are still not efficiently minable by conventional methods. In this study, we investigated the effect of copper complexing molecules such as amino acids on Cu^{2+} and S^{2-} solubilization from covellite.

Considering the general world-wide trend to mine more complex/lower grade copper ores,[1, 2] the need for advanced, alternative mining technologies is growing. Minerals such as Kupferschiefer or other complex ores face numerous problems in acid bioleaching and mineral processing.[3, 4] Bioleaching at pH ≥ 6 might be a possible alternative for such ores. In this study, we compared the efficiency of acidic (Asp & Glu), neutral (Gln & Asn) and basic (His & Arg) amino acids (AA) to solubilize synthetic covellite (CuS). In addition, we investigated the sulfide oxidation products formed under alkaline conditions during glutamic acid leaching of covellite.

EXPERIMENTAL. Pure solutions of respective amino acids (68 mM) were mixed with 10 mg of synthetic CuS and agitated for seven days. Potassium borate buffer (KBB, 15 mM, pH 9) was used as a reference solution. Copper concentration in the supernatant was determined by ICP-MS (ELEMENT XR, Thermo Scientific). Sulfur species were determined by ion chromatography (Dionex ICS–5000, Thermo Scientific) equipped with a Dionex IonPac AG11-HC column and pre-column (Thermo Scientific) and a conductivity detector. Analyte separation was performed in gradient elution mode with NaOH (1–50 mM). Flow rate was 1 mL/min and column temperature was 30 °C.

RESULTS. The efficiency of AA to solubilize covellite was investigated at two different pH values (Fig. 1). At pH 7, a Cu recovery of 8–17 % was achieved, with aspartate being the most efficient AA. At pH 9, the efficiency increased especially for acidic AA and arginine, whereas neutral AA and histidine showed only a minor increase in CuS solubilization efficiency. This means that under alkaline conditions the structure of the AA side chain plays a more important role, regarding leaching efficiency than under neutral conditions. Consequently, the efficiency is controlled by the type of AA and the pH of the system. In our study glutamic acid leaching at pH 9 showed the most promising results. The dominant sulfide oxidation products were identified as thiosulfate and sulfate (Fig. 2). Other intermediary sulfur species were formed in only minor amounts. Although S^{2-} is not completely oxidized, around 90 % of its oxidation products are water soluble and, thus, are not expected to form a passivating layer on the mineral surface. In conclusion, alkaline glutamic acid solutions seem to be a promising lixivant for copper extraction from covellite.

ACKNOWLEDGEMENT. This work was funded by the German Ministry of Education and Research (BMBF) and the French ANR, ref. no. 033RF001, within the transnational project "EcoMetals". Also, we would like to thank C. Schößler for her support during ICP-MS measurements.

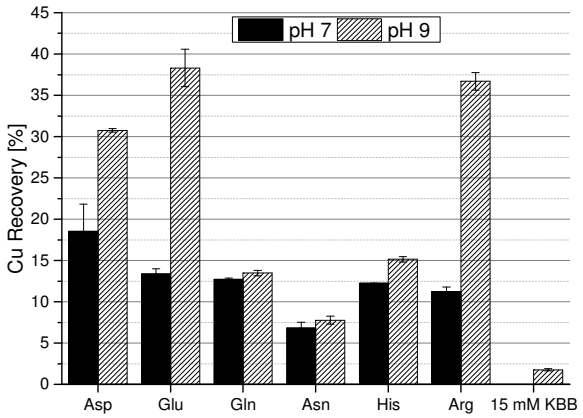

Fig. 1: Cu recovery in CuS leaching experiments at pH 7 and 9 after seven days.

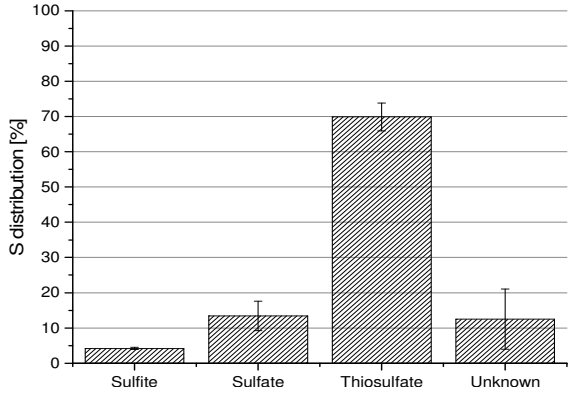

Fig. 2: Percentaged distribution of sulfur species formed after seven days of CuS leaching with glutamic acid at pH 9.

[1] Rawlings, D. E. (2004) *Pure Appl. Chem.* **76**, 847–859.
[2] Brierley, C. L. (2008) *Trans. Nonferrous Met. Soc. China* **18**, 1302–1310.
[3] Kutschke, S. *et al.* (2015) *Miner. Eng.* **75**, 116–125.
[4] Kiel, H. *et al.* (1980) *Z. Allg. Mikrobiol.* **20**, 627–636.

Protein mediated synthesis of fluorescent Au-nanoclusters for metal sensory coatings

M. Vogel, J. Raff

Fluorescent Au-nanocluster were successfully synthesized and used for the selective detection of Cu^{2+}. The synthesized Au-BSA-nanoclusters remain functional also after immobilization and show high thermal stability. Additionally, the transfer of the protein mediated Au-nanocluster synthesis route to S-layer proteins was achieved.

The presented work is part of the project BIONEWS dealing with long-term stable cells for the set-up and regeneration of sensor and actor materials for strategic relevant metals, in particular rare earth elements (REE). For the sensor materials, fluorescent Au-nanoclusters were considered. From literature it is known that fluorescence of Au-nanoclusters (Au-NC) can be stably achieved *via* protein mediated synthesis.[1] Additionally, it is possible to use changes of this fluorescence induced through interaction of Au-NC with target molecules for sensor applications. In a first step, the synthesis of Au-NCs with bovine serum albumin (BSA) was established and the selective response regarding heavy metals was verified. In a second step, the synthesis procedure will be transferred to other proteins which might be selective for REE.

EXPERIMENTAL. Au-BSA nanoclusters (Au-BSA-NC) were synthesized according to the protocol of Xie *et al.*[1] Fluorescence measurements were performed at an excitation wavelength of 470 nm with slit width of 2 nm using a fluorescence spectrometer (PTI QuantaMaster 40). Changes in fluorescence intensities caused by the addition of different metal ions were monitored at an emission maximum of 630 nm.

RESULTS. According to the published protocol,[1] BSA was successfully used for the synthesis of highly fluorescent Au-BSA-NCs. Upon excitation at 470 nm the Au-NC suspension shows a fluorescence emission maximum at 630 nm which can be mainly attributed to Au_{25}-NC (Fig. 1).

The fluorescent Au-BSA-NCs are highly stable and were used for the detection of Cu^{2+} by induced quenching of fluorescence (Fig 1). Depending on the used amount of Au-NCs, Cu^{2+} concentrations in the µM-range could be measured. The selectivity of the Au-BSA-NCs for Cu^{2+} was proven compared to several other heavy metal ions (Fig. 2). Besides Cu^{2+} there was only a slight response towards Ni^{2+} and Co^{2+}. All other tested metals showed no significant fluorescence quenching even if applied in 10-times excess compared to Cu^{2+} (data not shown).

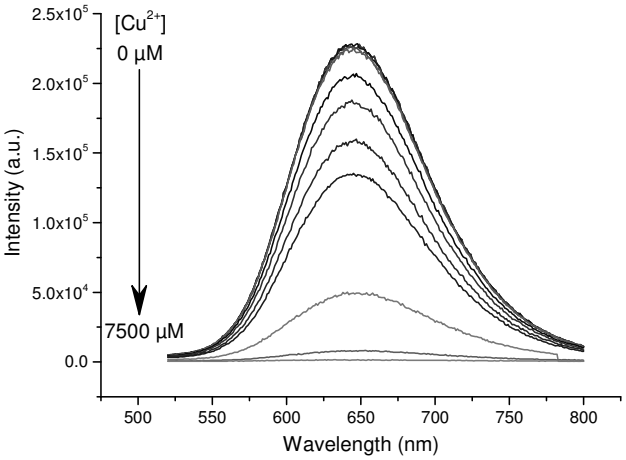

Fig. 1: Fluorescence spectra of Au-BSA-NC without and with addition of Cu^{2+}.

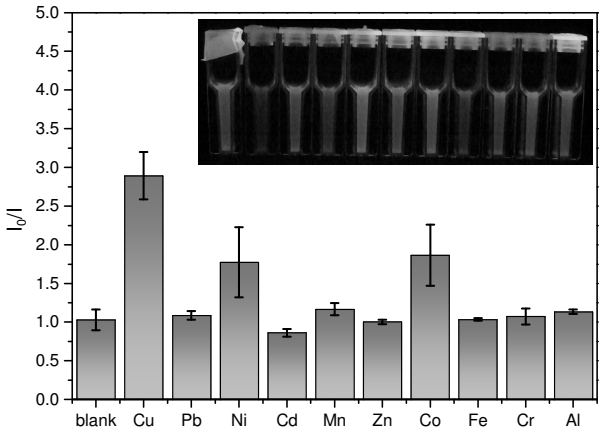

Fig. 2: Selectivity of Au-BSA-NC towards Cu^{2+} compared to other metal ions (250 µM): the graph shows the ratio of fluorescence intensity at emission maximum 630 nm without metal (I_0) and after addition of metal (I). Inset: Corresponding picture of cuvettes with Au-BSA-NC under UV-light 365 nm after addition of metal. ion.

The response of Au-BSA-NCs was also proven in real waters and after immobilization of the NCs in polymer matrices like agarose. Also important for use of the NCs in sensor coatings for technical applications is the thermal stability. Here it was shown, that the functionality is still given after incubation at 70 °C for 24 h.

Within this study, it was possible to establish the protein mediated synthesis of fluorescent Au-NCs for metal sensory coatings. Furthermore, the synthesis method was transferred to Ca-binding S-layer proteins. The S-layer is able to selectively bind REE in replacement for Ca^{2+}. Now, Au-S-layer-NCs can be tested for potential selective response towards lanthanides and also trivalent actinides.

ACKNOWLEDGEMENTS. The project BIONEWS was funded by BMBF (FKZ03WKCL03F) within the "Wachstumskern BioSAM".

[1] Xie, J. *et al.* (2009) *J. Am. Chem. Soc.* **131**, 888–889.

Nuclear Reactor

SAFETY RESEARCH

Coupling of the core simulator DYN3D with the CFD solver Trio_U and its application to a Main Steamline Break scenario

A. Grahn, A. Gommlich, S. Kliem

In the framework of the European project NURESAFE, the reactor dynamics code DYN3D developed at HZDR was coupled with the CFD solver Trio_U from CEA France. This coupling was used to simulate the coolant mixing in the reactor pressure vessel and in the core during a Main Steamline Break (MSLB) accident and to study its effect on the reactor power.

It is well known that the reactivity and the thermal power generation in the core of light water reactors (LWR) are very sensitive to changes in the feedback parameters moderator density and fuel temperature. The latter is tightly connected to the moderator temperature and to the heat transfer between fuel and coolant and, thus, strongly depends on the coolant flow conditions. During an MSLB accident which involves a sudden temperature drop in the affected coolant loop, large temporal and spatial temperature gradients in the coolant are expected to occur in the reactor and, hence, may cause the reactor to become critical and to produce a power excursion. The detailed modelling of the coolant flow using a 3D-capable flow simulation tool, such as Trio_U,[1] provides a more reliable prediction of the power distribution in the reactor core during a scenario of this kind. In the coupling implementation, the part of DYN3D,[2] which solves the one-dimensional equations of momentum, boron and heat convection in a fuel assembly-wise manner, is replaced by the fully three-dimensional capabilities of Trio_U.

IMPLEMENTATION OF THE COUPLING. The data interface between the codes is the volumetric heat source computed and sent to Trio_U by DYN3D. In the opposite direction, boron concentration, coolant velocity, temperature and pressure are sent to DYN3D. The quantities received from Trio_U are needed to correctly calculate the neutronic feedback on nuclear power as well as the heat transfer into the coolant. On the coding level, the coupling makes use of the SALOME platform (www.salome-platform.org) which is open-source and provides programming classes and methods for data storage, interpolation, mesh generation and code parallelization.

RESULTS. A 4-loop pressurized water reactor of Westinghouse design served as the reference reactor for simulating the MSLB accident. The transient starts from the shut-down state at hot zero power and involves overcooling through loop 1. Figure 1 shows the coolant temperature distributions in the inlet, with the overcooled sector shaded dark, and outlet planes of the core. The reactor becomes critical in the

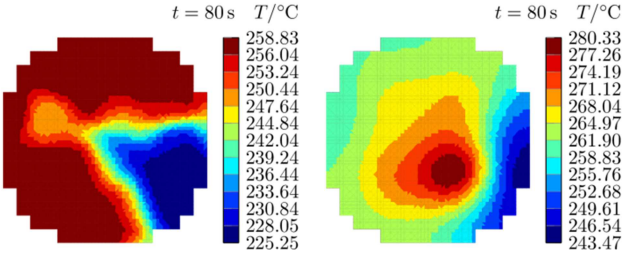

Fig. 1: Coolant temperature distributions at the core inlet (left) and outlet (right) at the end of loop 1 overcooling during MSLB accident.

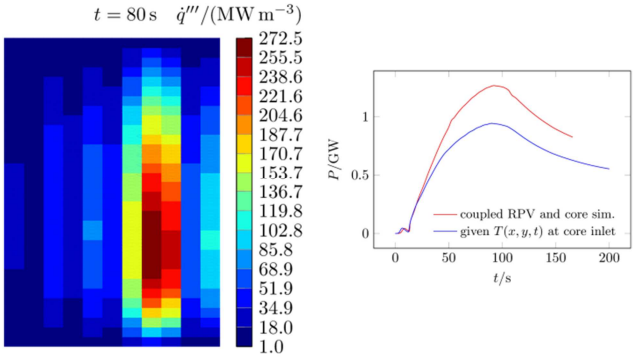

Fig. 2: Power density distribution in the vertical plane with stuck control rod assembly (left) ; comparison coupled simulation with given coolant temperature at the core inlet, t = 92.5 s (right)

overcooled sector and produces heat power, as it can be seen in Fig. 2 (left). On the right of Fig. 2, the reactor power is shown as a function of time. For comparison, the MSLB was simulated using a given coolant temperature distribution leading to the dashed power curve. It can be seen how a detailed modelling of coolant mixing by means of CFD helps to predict reactor behavior in a more reliable way.

ACKNOWLEDGEMENTS. This work was financed by the EU FP 7 project "NURESAFE".

[1] Angeli, P.-E. *et al.* (2015) *Overview of the TrioCFD code: main features, v&v procedures and typical applications to nuclear engineering.* In: Nureth-16.
[2] Rohde, U. *et al.* (2016) *Prog. Nucl. Energy* **89**, 170–190.

Extension of hybrid micro-depletion model for decay heat calculation in the DYN3D code

Y. Bilodid, E. Fridman, D. Kotlyar,[1] E. Shwageraus[2]
[1]Georgia Institute of Technology, Atlanta, U.S.A.; [2]University of Cambridge, United Kingdom

This work extends the hybrid micro-depletion methodology, recently implemented in DYN3D, to the decay heat calculation by accounting explicitly for the heat contribution from the decay of each nuclide in the fuel.

Coupling of neutron kinetics codes with plant thermo-hydraulic codes is widely used for analysis of complicated transient and accident scenarios where both 3-dimensional neutronics and thermal feedbacks from plant components and safety systems play essential role.
DYN3D is a 3D nodal reactor dynamic code developed at the Helmholtz-Zentrum Dresden–Rossendorf mainly for transients, but also for steady-state and fuel cycles analysis in LWR cores with hexagonal or square fuel assemblies.[1] It can be used as part of a coupled system with codes such as ATHLET and RELAP5.[2, 3]
Simulation of residual decay heat is important in a number of accident scenarios such as loss of coolant, main steam line break, etc.
DYN3D calculates node-wise decay heat power by applying methodology described in German normative document DIN Norm 25463.[4, 5] The fission products of four fissile isotopes ^{235}U, ^{238}U, ^{239}Pu and ^{241}Pu are divided into 24 groups each having a characteristic decay constant. Decay heat power is calculated individually for each node taking into account local power history. The model is suitable for decay heat calculation for UOX fuel in light water reactors with a maximum initial enrichment of 4.1 %.
This work presents an explicit method of decay heat calculation recently implemented in DYN3D. This method relies on "first principles" – it utilizes detailed information about nuclide content and does not require approximations or assumptions about fuel content evolution with depletion. Thus, the proposed method is general and not limited to particular fuel types.

EXPLICIT DECAY HEAT MODEL. The hybrid microscopic depletion method was recently developed and implemented in DYN3D.[6] The isotopic depletion solver is based on fast and accurate CRAM method and is able to calculate a nuclide content of each node taking into account local operational history which is used to improve the accuracy of homogenized cross sections.[7] DYN3D tracks about 1200 nuclides and utilizes complete decay and depletion chains (i.e. no shortcuts and asymptotic assumptions). The fact that DYN3D tracks full set of nuclides during all depletion and decay steps allows explicit calculations of important fuel characteristics such as decay heat power in each node:

$$P^n(t) = \sum_i N_i^n(t)\lambda_i q_i \,, \qquad (1)$$

where $P^n(t)$ is the decay heat power in node n at time t, $N_i^n(t)$ is the nuclide i concentration in node n, λ_i and q_i are the decay constant and energy release per decay of the nuclide i, respectively. The sum in Eq. (1) is over the entire set of nuclides in the node.
Currently, the depletion solver considers five types of neutron reactions: (n,γ), (n,fission), (n,2n), (n,3n), and (n,α). Homogenized few-group *microscopic* cross sections (XS) for the considered reactions are generated by a lattice transport code along with homogenized few-group *macroscopic* XS and included in the few-group cross section library utilized by DYN3D. The decay constants, fission yield data, and energy release per decay of each nuclide are included in an internal DYN3D library of physical constants.

VALIDATION. A verification of the new decay heat power calculation capability has been performed using a simple test model. The considered test case is a BWR UOX fuel pin with reflective boundary conditions. The depletion and decay calculations were performed with DYN3D employing homogenized macro- and microscopic XS generated by Serpent 2 Monte Carlo code.[8] The obtained XS library was used to simulate different depletion and outage scenarios. DYN3D results were benchmarked against the reference Serpent Monte Carlo solution.

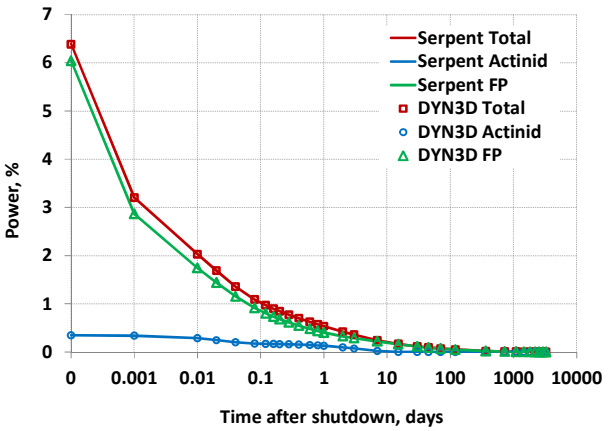

Fig. 1: Decay heat power after shutdown in test case.

The results of the decay heat power calculations depicted in Fig. 1 show excellent agreement between DYN3D and Serpent. For the entire simulated time period, from minutes to 10 years, DYN3D is able to reproduce the reference decay heat power and its components within 0.5 % deviations.

[1] Rohde, U. *et al.* (2016) *Prog. Nucl. Energy* **89**, 170–190.
[2] Grundmann, U. *et al.* (1995) *Proc. M&C 1995.*
[3] Kozmenkov, Y. *et al.* (2001) *Proc. JTKG 2001.*
[4] DIN Norm 25463, 1990.
[5] Grundmann, U. *et al.* (2005) *Report FZR-434.*
[6] Bilodid, Y. *et al.* (2016) *Ann. Nucl. Energy* **92**, 397–406.
[7] Pusa, M. *et al.* (2010). *Nucl. Sci. Eng.* **164**, 140–150.
[8] Leppänen, J. *et al.* (2013) *Ann. Nucl. Energy* **82**, 142–150.

Modeling of Phenix End-of-Life control rod withdrawal benchmark with DYN3D SFR version

E. Nikitin, E. Fridman

The reactor dynamics code DYN3D is currently under extension for Sodium cooled Fast Reactor applications. The control rod withdrawal benchmark from the Phenix End-of-Life experiments was selected for verification and validation purposes. This report presents some selected results to demonstrate the feasibility of using DYN3D for steady-state Sodium cooled Fast Reactor analyses.

The Phenix End-of-Life (EOL) control rod (CR) withdrawal benchmark[1] was selected for verification and validation (V&V) purposes of Sodium cooled Fast Reactor (SFR) version of nodal diffusion code DYN3D.[2]

BENCHMARK DESCRIPTION. The benchmark comprises several code-to-code comparisons and a few experimental measurements on the Phenix EOL core. The latter is divided into two parts: the off-power tests and on-power tests. During the off-power (~50 kW) tests, the CR S-curves were measured for the CRs #1 and #4 with the balancing method. At the on-power tests, four different critical steady-states were achieved by shifting the CRs #1 and #4 (see Fig. 1). In the center part of the core, thermocouples have been positioned above each sub-assembly to measure the outlet sodium temperature distributions. During the experiments the total mass flowrate remained constant; therefore the radial power distribution can be calculated and can be compared with the calculations. Further details on the experiments are available in literature.[1] It should be noted that the core description provided by benchmark specification has some deficiencies, which means that only averaged distributions of materials, temperatures, burnup and sodium flow rates are available.

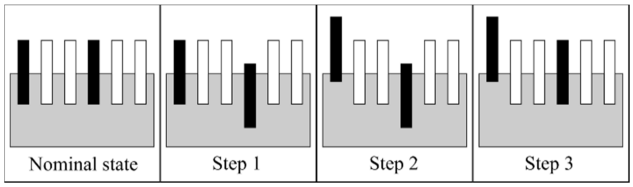

Fig. 1: Schematic overview on different CR positions.

CALCULATION METHODOLOGY. The full core nodal diffusion solutions of the benchmark were calculated with DYN3D. The homogenized few-group cross sections (XS) required by DYN3D were generated using the Monte Carlo (MC) code Serpent.[3] For further improvement of the nodal diffusion solution, Superhomogenization factors were used on CRs, first row of blankets and inside reflectors. Additionally, Serpent was also used to calculate the full core MC reference solutions for code-to-code comparisons. A more detailed description on the XS methodology and SPH method for realistic SFR cores can be found in literature.[4, 5]

RESULTS ON THE CR S-CURVES. The CR S-curves were calculated with both DYN3D and Serpent codes. The balancing method was reproduced with an iterative criticality search routine by using the movement of the compensation rod. A very good agreement was achieved between DYN3D and Serpent solutions. Compared to the experiment, DYN3D achieved a good agreement and overpredicted the CR worth by 119 and 70 pcm for CRs #1 and #4, respectively.

RESULTS ON THE ON-POWER TESTS. All steps of the CR-shift test were calculated with DYN3D. The obtained reactivity values are higher by ~800 pcm, which is still in a very good agreement with Serpent reference and the results of the benchmark participants. In the radial power prediction high discrepancies can be observed (e.g. in Fig. 2) between DYN3D and the experiment. This is the same difference that can be observed by other participants who used the same averaged core description (e.g. CEA ave. results in Fig. 2). The discrepancies can be explained by the lack of modeling details, since CEA, using their same code and a detailed core model, could reproduce the measured power in a better agreement (see Fig. 2 CEA det.).

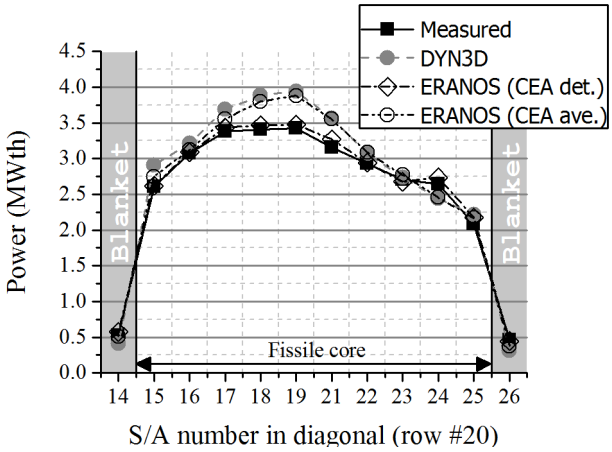

Fig. 2: Radial power distribution along the core diagonal at Step 2.

CONCLUSIONS. The SFR version of DYN3D was used to calculate the Phenix EOL CR withdrawal benchmark. The results were in a very good agreement compared to the MC reference solution in general. A good agreement was observed at the calculation of CR S-curves compared to the measurements. The CR-shift test calculations were in good agreement with other benchmark participants, but high discrepancies were observed compared to the experiment due to the averaged core modeling.

[1] International Atomic Energy Agency (2014) *Benchmark Analyses on the Control Rod Withdrawal Tests Performed during the PHÉNIX End-of-Life Experiments*, IAEA-TECDOC-1742. Vienna, Austria.
[2] Rohde, U. *et al.* (2016) *Prog. Nucl. Energy* **89**, 170–190.
[3] Leppänen, J. *et al.* (2015) *Ann. Nucl. Energy* **82**, 142–150.
[4] Nikitin, E. *et al.* (2015) *Ann. Nucl. Energy* **75**, 492–497.
[5] Nikitin, E. *et al.* (2015) *Ann. Nucl. Energy* **85** 544–551.

Application of the Severe Accident Code ATHLET-CD. Coolant injection to primary circuit of a PWR by mobile pump system in case of SBLOCA severe accident scenario

M. Jobst, P. Wilhelm, S. Kliem, Y. Kozmenkov

The improvement of the safety of nuclear power plants is a continuously on-going process. The analysis of transients and accidents is an important research topic, which significantly contributes to safety enhancements of existing power plants. In case of an accident with multiple failures of safety systems, core uncovery and heat-up can occur. In order to prevent the accident to turn into a severe one or to mitigate the consequences of severe accidents, different accident management measures can be applied. By means of numerical analyses performed with the compute code ATHLET-CD,[1] the effectiveness of coolant injection with a mobile pump system into the primary circuit of a PWR was studied. According to the analyses, such a system can stop the melt progression if it is activated prior to 10 % of total core is molten.

Within the framework of the joint research project „Weiterentwicklung und Anwendung von Severe Accident Codes – Bewertung und Optimierung von Störfallmaßnahmen“ (WASA-BOSS) of the Federal Ministry of Education and Research, HZDR focused on analyses of hypothetical severe accidents for a generic pressurized water reactors of German type KONVOI, assessment and optimization of accident management measures (AMM). Two basic accident scenarios were investigated: station blackout (total loss of AC power supply) and small-break loss-of-coolant accidents (SBLOCA). Results of a SBLOCA are presented here.

NUMERICAL ANALYSES. The ATHLET-CD model developed for a generic KONVOI was used to investigate an accident scenario with a 50 cm^2 leak located in the cold leg of the connected to the pressurizer loop.[2, 3] The accident progression strongly depends on the available emergency core cooling systems (ECCS) and on secondary side systems/procedures like cool-down procedure.[3]
A scenario without secondary cool-down and failure of the sump injection after depletion of the flooding pools leads to a core degradation scenario. With no further water injection from any of the active and passive safety systems – hot leg hydro-accumulators (HAs) are depleted and cold leg HAs are disconnected from the primary circuit – the core outlet temperature $T_{core,out}$ exceeds 400 °C approximately 3 h after beginning of the accident. The reconnection of cold leg HAs and delayed usage of their coolant inventory was also studied,[4] but here this measure is assumed to be unavailable. Secondary side pressure is higher than on primary side with the consequence of reversed heat flux. Therefore, the decay heat is only removed by steam discharge through the leak and consequently the reactor pressure vessel (RPV) level decreases. Melting of absorber material occurs at 3 h 20 min, followed by melting of fuel, release of fission products and relocation to the lower head (LH) until 3 h 45 min. Failure of RPV by creep rupture is predicted at 7 h 30 min (Fig. 1). As additional AMM, the injection by mobile equipment to the primary circuit was investigated. A connection of the pump to the ECCS injection lines is assumed and a realistic pump characteristic of a mobile fire pump is implemented (nominal pump head 16.5 bar, max. mass flow rate 39 kg/s). A parameter study with variation of the pump activation was performed, covering the range from early activation at

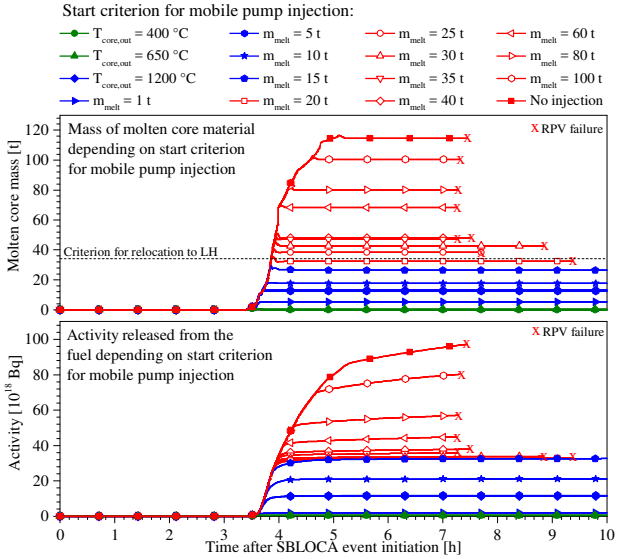

Fig. 1: 50 cm^2-SBLOCA scenario with injection by mobile pump to primary circuit. Mass of molten core material and released activity until failure of RPV.

$T_{core,out}$ = 400 °C to late activation with already partly molten core (caused e.g. by additional delay in preparation of the mobile system). The code simulations showed that for all scenarios with pump injection the further progression of fuel melting could be stopped, and the earlier the pump was activated the lower was the amount of released fission products (FPs, Fig. 1). However, the relocation to the lower plenum and subsequent RPV failure can only be avoided if the mobile pump is activated at a maximum of 15 tons melt mass (approx. 10 % of the core at 3 h 45 min into the transient). The application of the mobile pump system as the only AMM is not sufficient to prevent the release of FPs, despite it is started early in the transient at $T_{core,out}$ = 400 °C (release of 4.4×10^{17} Bq into reactor cooling system is predicted). Additional simulations showed that the application of primary side depressurization performed at $T_{core,out}$ = 400 °C in combination with the mobile pump can prevent the release of FPs.[4]

ACKNOWLEDGEMENTS. The authors would like to express their gratitude to the ATHLET-CD code developers' team at GRS for their continuous support. This work was performed within the WASA-BOSS project funded by the German Federal Ministry of Education and Research under project number 02NUK028B. The authors of this publication are responsible for its content.

[1] Austregesilo, H. *et al.* (2013) *ATHLET-CD Mod 3.0 Cycle A User's Manual,* Gesellschaft für Anlagen- und Reaktorsicherheit (GRS) mbH.
[2] Tusheva, P. *et al.* (2015) *atw.* **60**, 442–447.
[3] Jobst, M. *et al.* (2016) WASA-BOSS Milestone report M35.
[4] Wilhelm, P. *et al.* (2016) WASA-BOSS Milestone report M-B2.

Source term and activation calculations for the new TR-FLEX cyclotron for medical applications at HZDR

S. E. Müller, J. Konheiser, A. Ferrari,[1] A. Magin,[2] B. Naumann[3]

[1]HZDR, Institute of Radiation Physics, Dresden, Germany; [2]Karlsruhe Institute of Technology, Karlsruhe, Germany; [3]HZDR, Department of Radiation Protection & Safety, Dresden, Germany

The neutron source terms for a proton beam hitting an ^{18}O-enriched water target were calculated with the radiation transport programs MCNP6[1] and FLUKA[2] and were compared to source terms for exclusive ^{18}O(p,n)^{18}F production. To validate the radiation fields obtained in the simulations, an experimental program has been started using activation samples originally used in reactor dosimetry.

A TR-FLEX cyclotron is currently being commissioned at the Center of Radiopharmaceutical Cancer Research in the HZDR. The extended energy range of up to 28 MeV of protons for the ^{18}O(p,n)^{18}F reaction required a recalculation of the neutron source terms needed in the shielding calculations, since the vendor supplied data was based on a 24 MeV-proton beam. The radiation transport programs MCNP6 and FLUKA were used to calculate the neutron fluence emerging from the ^{18}O-enriched water target during operations.[3] Both Monte Carlo programs agree within 20 % on the neutron yield per incident proton for 24 and 28 MeV proton beams. However, the manufacturer supplied data for total neutron yield at 24 MeV is about a factor of 5 lower than the results of the Monte Carlo simulations. Figure 1 shows the different neutron spectra for a proton current of 300 µA and energy of 24 MeV. While at about 12 MeV the results of the three evaluations agree, at lower energies the values of the manufacturer source are up to one order of magnitude smaller respect to the MCNP6 and FLUKA values. It is assumed that these differences result from the omission of additional reaction channels with neutrons in the final state in the manufacturer's evaluation of the neutron source term, which only takes into account the ^{18}O(p,n)^{18}F reaction. The Monte Carlo codes MCNP6 and FLUKA take all additional channels into account, and should therefore provide a more complete description of the neutron source term.

ACTIVATION STUDIES. To validate the Monte Carlo results, irradiation experiments were carried out at the existing cyclotron currently used for the production of radiopharmaceuticals at HZDR, which provides proton beams of 18 MeV. Small metal foils were placed above the water target during one of the daily production runs of ^{18}F. After irradiation, the samples were analyzed by γ-spectroscopy at VKTA e.V., Dresden, Germany. To compare this to the Monte Carlo simulations, the target geometry was modeled in a detailed way with MCNP6 and FLUKA, and simulation campaigns were run to estimate the sample activation. Table 1 shows the first results for the sample activity present at the end of irradiation for several neutron-induced reactions. The calculated results agree reasonably well with the experimental measurements. These first results confirm the assumption that the calculation of the neutron source term using only the yield for the ^{18}O(p,n)^{18}F reaction results in an incorrect neutron output.

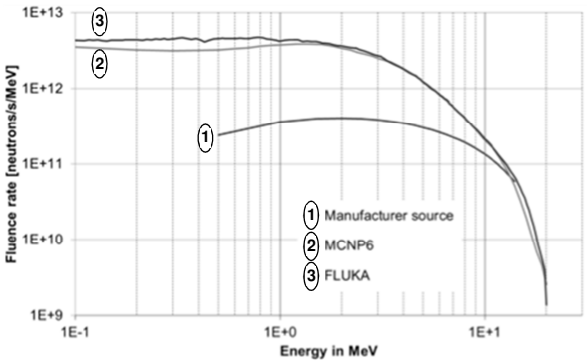

Fig. 1: Differential spectra of neutron fluence rate per MeV at 24 MeV proton energy and 300 µA.

Tab. 1: First results for measured and calculated activities of different reactions at the end of irradiation with 18 MeV proton beam, proton current of 30 µA and an irradiation time of 50 min.

Reaction	Activities (Bq)			Calc./Exp. ratio	
	Exp. (%)	MCNP6	FLUKA (%)	MCNP6	FLUKA
^{58}Ni(n,p)^{58}Co	280 ± 6	294	320 ± 2	1.05	1.14
^{186}W(n,g)^{187}W	180 ± 7	195	288 ± 15	1.08	1.60
^{124}Sn(n,g)^{125}Sn	0.67 ± 34	0.61	0.6 ± 42	0.91	0.90
^{64}Zn(n,g)^{65}Zn	1.6 ± 9	2.59	2.9 ± 5	1.62	1.81
^{68}Zn(n,g)^{69m}Zn	31 ± 6	32.95	22.7 ± 40	1.06	0.73

[1] Goorley, T. *et al.* (2012) *Nucl. Technol.* **180**, 298–315.
[2] Ferrari, A. *et al.* (2005) *CERN-2005-10, INFN/TC_05/11*, SLAC-R-773.
[3] Konheiser, J. *et al.* (2016) *J. Radiol. Prot.* **36**, 819–831.

Measurement of the cross-sectional void distribution in the receiver pipe of parabolic trough collectors

A. Hoffmann

The local instantaneous void fraction in the cross-section at the DIrect Solar Steam (DISS) test facility at the Plataforma Solar de Almería (PSA), Spain, was investigated by means of a wire-mesh sensor. The experiments were conducted at qualities of $\dot{x} < 0.5$, mass flow rates of $\dot{m} = 0.7–1.11$ kg s^{-1} and pressures of $P_{out} = 30–80$ bar.

Since 1998, the DISS test facility at the PSA has been used to study the direct steam generation in parabolic trough collectors. The recently renewed DISS test facility,[1] can be operated up to live steam conditions of 500 °C and 110 bar at the outlet.[2] The overall operation in once-trough mode can be controlled well under transient conditions.[1] However, knowledge gaps exist about the prevailing flow pattern within the receiver pipes that are important for heat transfer analysis and stress analysis. The present study measured the prevailing flow pattern by an invasive measurement device for the first time.

METHOD. The flow patterns were investigated by a wire-mesh sensor (WMS) that was custom-engineered at the Helmholtz-Zentrum Dresden–Rossendorf to meet the specific conditions at the DISS test facility. The WMS measures the different conductivities of the water and steam phase to provide information about the local instantaneous void fraction. The WMS was welded to the connection pipe immediately at the end of collector 1A (Fig. 1). Upstream of the wire-mesh sensor, the horizontal receiver pipe with a total length of 96 m (≈1600 diameters) ensured that the flow was fully developed at the position of the WMS. The measurements were carried out under constant boundary conditions of inlet mass flow rate, outlet pressure, inlet temperature of the fluid and solar irradiation.

RESULTS. The data obtained indicate the occurrence of stratified-wavy flow, wavy flow, slug flow or large-amplitude waves (roll waves). Slug flow and roll waves were observed up to pressures of 45 bar. Figure 2 shows a typically measured averaged instantaneous liquid fraction during slug flow/roll waves. Stratified and wavy flows were measured at all considered pressure levels. Basically, the flow pattern map tends to agree with the experiments. At pressures of about 60 bar and 80 bar, the flow pattern map seems to underestimate the size of the slug/ stratified-wavy flow region (Fig. 3). The cases assigned as "lateral" indicate that the concentrated solar irradiation has entered by the side of the receiver pipe instead of the bottom.

ACKNOWLEDGEMENTS. The author is grateful to all colleagues at the HZDR, DLR and CIEMAT who have been involved in the research. The financial support of the HZDR and DLR is greatly acknowledged.

[1] Feldhoff, J. F. (2015) PhD thesis, RWTH Aachen, Germany.
[2] Feldhoff, J. F. *et al.* (2014) *Energy Procedia* **49**, 1766–1776.
[3] Wojtan, L. *et al.* (2005) *Int. J. Heat Mass Transf.* **48**, 2955–2969.

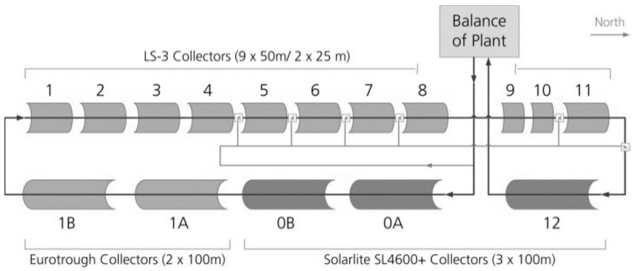

Fig. 1: Renewed DISS test facility at the PSA, Spain.[2]

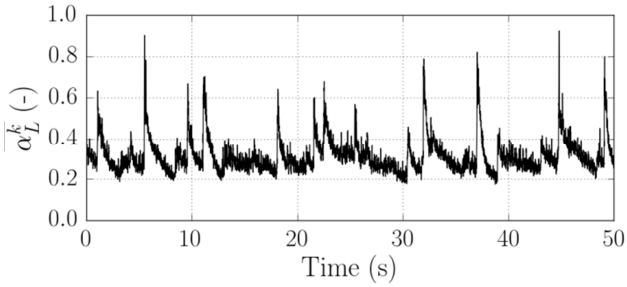

Fig. 2: Instantaneous cross-sectional averaged liquid fraction during slug flow/ roll wave conditions at P_{out} = 30 bar.

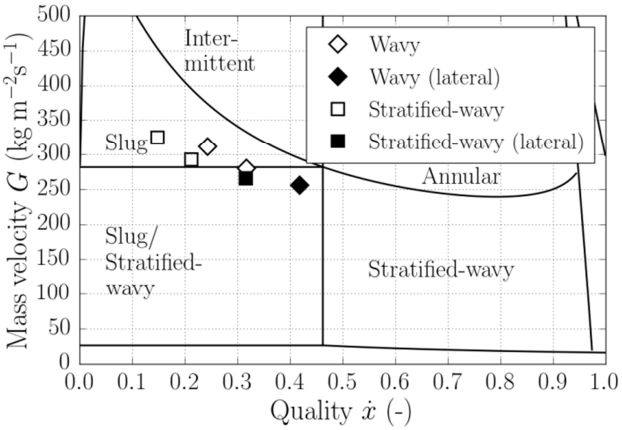

Fig. 3: Comparison of experimentally observed flow patterns with the flow pattern map of [3] at P_{out} = 80 bar.

- ARTICLES (PEER-REVIEWED)
- ORAL PRESENTATIONS
- PATENT
- THESES

ARTICLES (PEER-REVIEWED)

Acher, E.; Cherkaski, Y. H.; Dumas, T.; Tamain, C.; Guillaumont, D.; Boubals, N.; Javierre, G.; Hennig, C.; Solari, P. L.; Charbonnel, M.-C.
Structures of plutonium(IV) and uranium(VI) with *N*,*N*-dialkyl amides from crystallography, X-ray absorption spectra, and theoretical calculations.
Inorganic Chemistry 55, 5558–5569 (2016).

Adlassnig, W.; Weiss, Y. S.; Sassmann, S.; Steinhauser, G.; Hofhansl, F.; Baumann, N.; Lichtscheidl, I. K.; Lang, I.
The copper spoil heap Knappenberg, Austria, as a model for metal habitats – Vegetation, substrate and contamination
Science of the Total Environment 563–564, 1037–1049 (2016).

Arab-Chapelet, B.; Martin, P.; Costenoble, S.; Delahaye, T.; Scheinost, A. C.; Grandjean, S.; Abraham, F.
Multiscale structural characterizations of mixed U(IV)-An(III) oxalates (An(III) = Pu or Am) combining XAS and XRD measurements
Dalton Transactions 45, 6909–6919 (2016).

Baldova, D.; Fridman, E.; Shwageraus, E.
High Conversion Th–U233 fuel for current generation of PWRs: Part III – Fuel availability and utilization considerations
Annals of Nuclear Energy 87, 517–526 (2016).

Barkleit, A.; Heller, A.; Ikeda-Ohno, A.; Bernhard, G.
Interaction of europium and curium with alpha-amylase
Dalton Transactions 45, 8724–8733 (2016).

Belskaya, O. B.; Stepanova, L. N.; Gulyaeva, T. I.; Erenburg, S. B.; Trubina, S. V.; Kvashnina, K.; Nizovskii, A. I.; Kalinkin, A. V.; Zaikovskii, V. I.; Bukhtiyarov, V. I.; Likholobov, V. A.
Influence of Zinc on the Formation and Properties of Catalysts Pt/Mg(Zn)AlO$_x$ Synthesized from Layered Hydroxides
Journal of Catalysis 341 (2016).

Bès, R.; Rivenet, M.; Solari, P. L.; Kvashnina, K. O.; Scheinost, A. C.; Martin, P. M.
On the use of HERFD-XANES at the U L_3 and M_4-edges to determine the uranium valence state on $[Ni(H_2O)_4]_3[U(OH,H_2O)(UO_2)_8O_{12}(OH)_3]$
Inorganic Chemistry 55, 4260–4270 (2016).

Bilodid, Y.; Kotlyar, D.; Shwageraus, E.; Fridman, E.; Kliem, S.
Hybrid microscopic depletion model in nodal code DYN3D
Annals of Nuclear Energy 92, 397–406 (2016).

Biswas, S.; Steudtner, R.; Schmidt, M.; McKenna, C.; Vintró, L. L.; Twamley, B.; Baker, R. J.
An investigation of the interactions of Eu^{3+} and Am^{3+} with uranyl minerals: implications for the storage of spent nuclear fuel
Dalton Transactions 45, 6383–6393 (2016).

Butorin, S.; Kvashnina, K. O.; Smith, A.; Popa, K.; Martin, P.
Crystal-field and covalency effects in uranates: X-ray spectroscopic study
Chemistry–A European Journal 22, 9693–9698 (2016).

Butorin, S. M.; Kvashnina, K. O.; Vegelius, J. R.; Meyer, D.; Shuh, D. K.
High-resolution X-ray absorption spectroscopy as a probe of crystal-field and covalency effects in actinide compounds
Proceedings of the National Academy of Sciences of the United States of America 113, 8093–8097 (2016).

Butorin, S.; Modin, A.; Vegelius, J.; Kvashnina, K. O.; Shuh, D.
Probing chemical bonding in uranium dioxide by means of high-resolution X-ray absorption spectroscopy
Journal of Physical Chemistry C 120, 29397–29404 (2016).

Caisso, M.; Roussel, P.; Den Auwer, C.; Picart, S.; Hennig, C.; Scheinost, A. C.; Delahaye, T.; Ayral, A.
Evidence of trivalent Am substitution into U_3O_8
Inorganic Chemistry 55, 10438–10444 (2016).

Cherkouk, A.; Law, G. T. W.; Rizoulis, A.; Law, K.; Renshaw, J. C.; Morris, K.; Livens, F. R.; Lloyd, J. R.
Influence of riboflavin on the reduction of radionuclides by Shewanella oneidenis MR-1
Dalton Transactions 45, 5030–5037 (2016).

Chollet, M.; Martin, P.; Degueldre, C.; Poonoosamy, J.; Belin, R. C.; Hennig, C.
Neptunium characterization in uranium dioxide fuel: Combining a XAFS and a thermodynamic approach
Journal of Alloys and Compounds 662, 448–454 (2016).

Comarmond, M. J.; Steudtner, R.; Stockmann, M.; Heim, K.; Müller, K.; Brendler, V.; Payne, T. E.; Foerstendorf, H.
The Sorption Processes of U(VI) onto SiO_2 in the Presence of Phosphate: from Binary Surface Species to Precipitation
Environmental Science & Technology 50, 11610–11618 (2016).

Degler, D.; Pereira De Carvalho, H. W.; Kvashnina, K.; Grunwaldt, J. D.; Barsan, U. W. N.
Structure and chemistry of surface-doped Pt:SnO_2 gas sensing materials
RSC Advances 6, 28149–28155 (2016).

Drobot, B.; Bauer, A.; Steudtner, R.; Tsushima, S.; Bok, F.; Patzschke, M.; Raff, J.; Brendler, V.
Speciation Studies of Metals in Trace Concentrations: The Mononuclear Uranyl(VI) Hydroxo Complexes
Analytical Chemistry 88, 3548–3555 (2016).

Dumas, T.; Guillaumont, D.; Fillaux, C.; Scheinost, A.; Moisy, P.; Petit, S.; Shuh, D. K.; Tyliszczak, T.; Den Auwer, C.
The nature of chemical bonding in actinide and lanthanide ferrocyanides determined by X-ray absorption spectroscopy and density functional theory
Physical Chemistry, Chemical Physics 18, 2887–2895 (2016).

Gerber, U.; Zirnstein, I.; Krawczyk-Bärsch, E.; Lünsdorf, H.; Arnold, T.; Merroun, M. L.
Combined use of flow cytometry and microscopy to study the interactions between the gram-negative betaproteobacterium *Acidovorax facilis* and uranium(VI)
Journal of Hazardous Materials 317, 127–134 (2016).

Gregson, M.; Lu, E.; Tuna, F.; McInnes, E. J. L.; Hennig, C.; Scheinost, A. C.; McMaster, J.; Lewis, W.; Blake, A. J.; Kerridge, A.; Liddle, S. T.
Emergence of comparable covalency in isostructural cerium(IV)- and uranium(IV)-carbon multiple bonds
Chemical Science 7, 3286–3295 (2016).

Gumeniuk, R.; Schnelle, W.; Ahmida, M.; Abd-Elmeguid, M.; Kvashnina, K. O.; Tsirlin, A.; Leithe-Jasper, A.; Geibel, C.
Valence fluctuations of europium in the boride $Eu_4Pd_{29+x}B_8$
Journal of Physics: Condensed Matter 28, 115601 (2016).

Gumeniuk, R.; Schnelle, W.; Kvashnina, K. O.; Leithe-Jasper, A.
Kondo effect and thermoelectric transport in $CePd_3Be_x$
Journal of Physics: Condensed Matter 28, 165603 (2016).

Hellebrandt, S.; Lee, S. S.; Knope, K. E.; Lussier, A. J.; Stubbs, J. E.; Eng, P. J.; Soderholm, L.; Fenter, P.; Schmidt, M.
A comparison of adsorption, reduction, and polymerization of the plutonyl(VI) and uranyl(VI) ions from solution onto the muscovite basal plane
Langmuir 32, 10473–10482 (2016).

Hellebrandt, S. E.; Hofmann, S.; Jordan, N.; Barkleit, A.; Schmidt, M.
Incorporation of Eu(III) into Calcite under Recrystallization conditions
Scientific Reports 6, 33137 (2016).

Hoffmann, A.; Hirsch, T.; Pitz-Paal, R.
Numerical investigation of severe slugging under conditions of a parabolic trough power plant with direct steam generation
Solar Energy 133, 567–585 (2016).

Hofmann, S.; Voitchovsky, K.; Spijker, P.; Schmidt, M.; Stumpf, T.
Visualising the molecular alteration of the calcite (104) – water interface by sodium nitrate
Scientific Reports 6, 21576 (2016).

Holt, L.; Rohde, U.; Kliem, S.; Baier, S.; Seidl, M.; Macían-Juan, R.
Investigation of Feedback on Neutron Kinetics and Thermal Hydraulics from Detailed Online Fuel Behavior Modelling during a Boron Dilution Transient in a PWR with the Two-way Coupled Code System DYN3D-TRANSURANUS
Nuclear Engineering and Design 297, 32–43 (2016).

Huittinen, N.; Arinicheva, Y.; Schmidt, M.; Neumeier, S.; Stumpf, T.
Using Eu^{3+} as an atomic probe to investigate the local environment in $LaPO_4$–$GdPO_4$ monazite end-members
Journal of Colloid and Interface Science 483, 139–145 (2016).

Iglesias, L.; Walther, C.; Medina, F.; Holzer, A.; Neumann, A.; Lozano-Rodriguez, M. J.; Alvarez, M. G.; Torapava, N.
A comprehensive study on iodine uptake by selected LDH phases *via* coprecipitation, anionic exchange and reconstruction
Journal of Radioanalytical and Nuclear Chemistry 307, 111–121 (2016).

Ikeda-Ohno, A.; Shahin, L. M.; Howard, D.; Collins, R. N.; Payne, T. E.; Johansen, M. P.
Fate of Plutonium at a Former Nuclear Testing Site in Australia
Environmental Science & Technology 50, 9098–9104 (2016).

Jain, R.; Dominic, D.; Jordan, N.; Rene, E. R.; Weiss, S.; van Hullebusch, E. D.; Hübner, R.; Lens, P. N. L.
Higher Cd adsorption on biogenic elemental selenium nanoparticles
Environmental Chemistry Letters 14, 381–386 (2016).

Jain, R.; Dominic, D.; Jordan, N.; Rene, E. R.; Weiss, S.; van Hullebusch, E. D.; Hübner, R.; Lens, P. N. L.
Preferential adsorption of Cu in a multi-metal mixture onto biogenic elemental selenium nanoparticles
Chemical Engineering Journal 284, 917–925 (2016).

Jeazet, H. B. T.; Gloe, K.; Doert, T.; Mizera, J.; Kataeva, O. N.; Tsushima, S.; Bernhard, G.; Weigand, J. J.; Lindoy, L. F.; Gloe, K.
Uranyl(VI) binding by bis(2-hydroxyaryl) diimine and bis(2-hydroxyaryl)diamine ligand derivatives. Synthetic, X-ray, DFT and solvent extraction studies
Polyhedron 103, 198–205 (2016).

Johansen, M. P.; Child, D. P.; Caffrey, E. A.; Davis, E.; Harrison, J. J.; Hotchkis, M. A. C.; Payne, T. E.; Ikeda-Ohno, A.; Thiruvoth, S.; Twining, J. R.; Beresford, N. A.
Accumulation of plutonium in mammalian wildlife tissues following dispersal by accidental-release tests
Journal of Environmental Radioactivity 151, 387–394 (2016).

Johnstone, E. V.; Hofmann, S.; Cherkouk, A.; Schmidt, M.
Study of the Interaction of Eu^{3+} with Microbiologically Induced Calcium Carbonate Precipitates using TRLFS
Environmental Science & Technology 50, 12411–12420 (2016).

Kämpfe, T.; Haußmann, A.; Eng, L. M.; Reichenbach, P.; Thiessen, A.; Woike, T.; Steudtner, R.
Time-resolved photoluminescence spectroscopy of Nb^{4+} and O–polarons in $LiNbO_3$ single crystals
Physical Review B 93, 174116 (2016).

Kelly, N.; Gloe, K.; Doert, T.; Hennersdorf, F.; Heine, A.; März, J.; Schwarzenbolz, U.; Weigand, J. J.; Gloe, K.
Self-assembly of [2+2] Co(II) metallomacrocycles and Ni(II) metallogels with novel bis(pyridylimine) ligands
Journal of Organometallic Chemistry 821, 182–191 (2016).

Konheiser, J.; Naumann, B.; Ferrari, A.; Brachem, C.; Müller, S.
Source Terms, Shielding Calculations and Soil Activation for a Medical Cyclotron
Journal of Radiological Protection 36, 819–831 (2016).

Konheiser, J.; Seidl, M.; Brachem, C.; Mueller, S.
Study of the uncertainties due to position change of the PWR aeroball measurement system (AMS)
Journal of Nuclear Science and Technology 53, 1715–1722 (2016).

Kulenkampff, J.; Gründig, M.; Lippman-Pipke, J.; Zakhnini, A.
Quantitative experimental monitoring of molecular diffusion in clay with positron emission tomography
Solid Earth 7, 1207–1215 (2016).

Kulenkampff, J.; Gründig, M.; Zakhnini, A.; Lippmann-Pipke, J.
Geoscientific process monitoring with positron emission tomography (GeoPET)
Solid Earth 7, 1217–1231 (2016).

Kvashnina, K. O.; Scheinost, A. C.
A Johann-type X-ray emission spectrometer at the Rossendorf beamline
Journal of Synchrotron Radiation 23, 836–841 (2016).

Lee, S. S.; Schmidt, M.; Fister, T. T.; Nagy, K. L.; Sturchio, N. C.; Fenter, P.
Structural Characterization of Aluminum (Oxy)hydroxide Films at the Muscovite (001)–Water Interface
Langmuir 32, 477–486 (2016).

Leppanen, J.; Pusa, M.; Fridman, E.
Overview of methodology for spatial homogenization in the Serpent 2 Monte Carlo code
Annals of Nuclear Energy 96, 126–136 (2016).

Lim, J. S.; Lee, J. H.; Ikeda-Ohno, A.; Ohkochi, T.; Kim, K. S.; Seidel, J.; Yang, C. H.
Electric-field-induced insulator to Coulomb glass transition *via* oxygen vacancy migration in Ca-doped $BiFeO_3$
Physical Review B 94, 035123 (2016).

Liu, J.; Wang, J.; Chen, Y.; Shen, C. C.; Jiang, X.; Xi, X.; Chen, D.; Lippold, H.; Wang, C.
Thallium dispersal and contamination in surface sediments from South China and its source identification
Environmental Pollution 213, 878–887 (2016).

Liu, J.; Wang, J.; Chen, Y.; Xie, X.; Qi, J.; Lippold, H.; Luo, D.; Wang, C.; Su, L.; He, L.; Wu, Q.
Thallium transformation and partitioning during Pb-Zn smelting and environmental implications
Environmental Pollution 212, 77–89 (2016).

Marques Fernandes, M.; Scheinost, A. C.; Baeyens, B.
Sorption of trivalent lanthanides and actinides onto montmorillonite: Macroscopic, thermodynamic and structural evidence for ternary hydroxo and carbonato surface complexes on multiple sorption sites
Water Research 99, 74–82 (2016).

Mesbah, A.; Clavier, N.; Lozano-Rodriguez, J.; Szenknect, S.; Dacheux, N.
Incorporation of thorium in the zircon structure type through the $Th_{1-x}Er_x(SiO_4)_{1-x}(PO_4)_x$ thorite-xenotime solid solution
Inorganic Chemistry 55, 11273–11282 (2016).

Moeyaert, P.; Dumas, T.; Guillaumont, D.; Kvashnina, K.; Sorel, C.; Miguirditchian, M.; Dufrêche, P. M. J. F.
Modeling and speciation of uranium (VI) and technetium (VII) co-extraction with DEHiBA
Inorganic Chemistry 55, 6511–6519 (2016).

Obeid, M. H.; Oertel, J.; Solioz, M.; Fahmy, K.
Mechanism of attenuation of uranyl toxicity by glutathione in Lactococcus lactis
Applied and Environmental Microbiology 82, 3563–3571 (2016).

Oertel, J.; Keller, A.; Prinz, J.; Schreiber, B.; Hübner, R.; Kerbusch, J.; Bald, I.; Fahmy, K.
Anisotropic metal growth on phospholipid nanodiscs *via* lipid bilayer expansion
Scientific Reports 6, 26718 (2016).

Poetsch, M.; Lippold, H.
Effects of ionic strength and fulvic acid on adsorption of Tb(III) and Eu(III) onto clay
Journal of Contaminant Hydrology 192, 146–151 (2016).

Pollmann, K.; Kutschke, S.; Matys, M.; Kostudis, S.; Hopfe, S.; Raff, J.
Novel Biotechnological Approaches for the Recovery of Metals from Primary and Secondary Resources
Minerals 6, 54 (2016).

Pombo-García, K.; Weiss, S.; Zarschler, K.; Ang, C. S.; Hübner, R.; Pufe, J.; Meister, S.; Seidel, J.; Pietzsch, J.; Spiccia, L.; Stephan, H.; Graham, B.
Zwitterionic polymer-coated ultrasmall superparamagnetic iron oxide nanoparticles with low protein interaction and high biocompatibility
ChemNanoMat 2, 959–971 (2016).

Popa, K.; Prieur, D.; Manara, D.; Naji, M.; Vigier, J. F.; Martin, P.; Blanco, O. D.; Scheinost, A. C.; Prüssmann, T.; Vitova, T.; Raison, P. E.; Somers, J.; Konings, R. J. M.
Further insights into the chemistry of the Bi–U–O system
Dalton Transactions 45, 7847–7855 (2016).

Prieur, D.; Lebreton, F.; Caisso, M.; Martin, P.; Scheinost, A. C.; Somers, J.; Delahaye, T.; Manara, D.
Melting behavior of americium-doped uranium dioxide
The Journal of Chemical Thermodynamics 97, 244–252 (2016).

Richter, C.; Müller, K.; Drobot, B.; Steudtner, R.; Großmann, K.; Stockmann, M.; Brendler, V.
Macroscopic and spectroscopic characterization of uranium(VI) sorption onto orthoclase and muscovite and the influence of competing Ca^{2+}
Geochimica et Cosmochimica Acta 189, 143–157 (2016).

Rohde, U.; Kliem, S.; Grundmann, U.; Baier, S.; Bilodid, Y.; Duerigen, S.; Fridman, E.; Gommlich, A.; Holt, L.; Grahn, A.; Kozmenkov, Y.; Mittag, S.
The reactor dynamics code DYN3D – models, validation and applications
Progress in Nuclear Energy 89, 170–190 (2016).

Ruiz-Gómez, G.; Hawkins, J. C.; Philipp, J.; Künze, G.; Wodtke, R.; Löser, R.; Fahmy, K.; Teresa Pisabarro, M.
Rational Structure-Based Rescaffolding Approach to de Novo Design of Interleukin 10 (IL-10) Receptor-1 Mimetics
PlosOne 11, e0154046 (2016).

Sandoval, A.; Eichler, S.; Madathil, S.; Reeves, P. J.; Fahmy, K.; Boeckmann, R. A.
The molecular switching mechanism at the conserved D(E)RY motif in class-A GPCRs
Biophysical Journal 111, 79–89 (2016).

Scheinost, A. C.; Steudtner, R.; Hübner, R.; Weiss, S.; Bok, F.
Neptunium^{V} retention by siderite under anoxic conditions: Precipitation of NpO_2–like nanoparticles and of Np^{IV} pentacarbonate
Environmental Science & Technology 50, 10413–10420 (2016).

Smith, A. L.; Martin, P.; Prieur, D.; Scheinost, A. C.; Raison, P. E.; Cheetham, A. K.; Konings, R. J. M.
Structural properties and charge distribution of the sodium uranium, neptunium and plutonium ternary oxides: a combined X-ray diffraction and XANES study
Inorganic Chemistry 55, 1569–1579 (2016).

Suhr, M.; Lederer, F. L.; Guenther, T. J.; Raff, J.; Pollmann, K.
Characterization of three different unusual S-layer proteins from *Viridibacillus arvi* JG-B58 that exhibits two super-imposed S-layer proteins
PlosOne 11, e0156785 (2016).

Suhr, M.; Raff, J.; Pollmann, K.
Au-Interaction of Slp1 polymers and monolayer from *Lysinibacillus sphaericus* JG-B53 - QCM-D, ICP-MS and AFM as tools for biomolecule-metal studies
Journal of Visualized Experiments 107 (2016).

Tagirov, B. R.; Trigub, A. L.; Kvashnina, K. O.; Shiryaev, A. A.; Chareev, D. A.; Nickolsky, M. S.; Abramova, V. D.; Kovalchuk, E. V.
Covellite CuS as a matrix for "invisible" gold: X-ray spectroscopic study of the chemical state of Cu and Au in synthetic minerals
Geochimica et Cosmochimica Acta 191, 58–69 (2016).

Tamain, C.; Dumas, T.; Guillaumont, D.; Hennig, C.; Guilbaud, P.
First evidence of a water soluble Pu(IV)-$[Pu_6(OH)_4O_4]^{12+}$-hexanuclear cluster
European Journal of Inorganic Chemistry 22, 3536–3540 (2016).

Vauchy, R.; Belin, R. C.; Robisson, A. C.; Lebreton, F.; Scheinost, A. C.; Aufore, L.; Martin, P. M.
Actinide oxidation state and O/M ratio in hypostoichiometric uranium-plutonium-americium $U_{0.750}Pu_{0.246}Am_{0.004}O_{2-x}$ mixed oxides
Inorganic Chemistry 55, 2123–2132 (2016).

Virtanen, S.; Bok, F.; Ikeda-Ohno, A.; Rossberg, A.; Lützenkirchen, J.; Rabung, T.; Lehto, J.; Huittinen, N.
The specific sorption of Np(V) on the corundum (α-Al_2O_3) surface in the presence of trivalent lanthanides Eu(III) and Gd(III): a batch sorption and XAS study
Journal of Colloid and Interface Science 483, 334–342 (2016).

Willms, T.; Kryk, H.; Oertel, J.; Lu, X.; Hampel, U.
Reactivity of t-butyl hydroperoxide and t-butyl peroxide toward reactor materials measured by a microcalorimetric method at 30 °C
Journal of Thermal Analysis and Calorimetry 126, 1–15 (2016).

Winde, F.; Erasmus, E.; Geipel, G.
Uranium contaminated drinking water linked to leukaemia – revisiting a case study from South Africa taking alternative exposure pathways into account
Science of the Total Environment 574, 400–421 (2016).

Yalcintas, E.; Scheinost, A. C.; Gaona, X.; Altmaier, M.
Systematic XAS study on the reduction and uptake of Tc by magnetite and mackinawite
Dalton Transactions 45, 17874–17885 (2016).

Zänker, H.; Weiss, S.; Hennig, C.; Brendler, V.; Ikeda-Ohno, A.
Oxyhydroxy silicate colloids: A new type of waterborne actinide(IV) colloids
ChemistryOpen 5, 174–182 (2016)

ORAL PRESENTATIONS

Adam, C.; Rohde, V.; Müllich, U.; Kaden, P.; Geist, A.; Panak, P. J.
Comparative NMR Study of nPrBTP and iPrBTP Complexes
ATALANTE 2016 – Nuclear Chemistry for Sustainable Fuel Cycles, June 05–10, 2016, Montpellier, France (2016).

Altmaier, M.; Brandt, F.; Brendler, V.; Chiorescu, I.; Colàs, E.; Curtius, H.; Endrizzi, F.; Franzen, C.; Gaona, X.; Grivé, M.; Hagemann, S.; Koke, C.; Kulik, D. A.; Krüger, S.; Lee, J. Y.; Maiwald, M.; Miron, G. D.; Panak, P. J.; Skerencak-Frech, A.; Steudtner, R.; Thoenen, T.; Tsushima, S.
ThermAc - a collaborative project investigating aquatic chemistry and thermodynamics of actinides at elevated temperature conditions
Plutonium Futures 2016, September 18–22, 2016, Baden–Baden, Germany (2016).

Arnold, T.; Sachs, S.
Activities of the Institute of Resource Ecology in the field of radioecology
SUBATECH Seminar, March 10, 2016, Nantes, France (2016).

Bader, M.; Müller, K.; Foerstendorf, H.; Drobot, B.; Schmidt, M.; Musat, N.; Swanson, J. S.; Reed, D. T.; Stumpf, T.; Cherkouk, A.
Multistage bioassociation of uranium to a halophilic archaeon under highly saline conditions
Halophiles (11th International Meeting), May 22–26, 2016, San Juan, Puerto Rico (2016).

Bader, M.; Müller, K.; Foerstendorf, H.; Schmidt, M.; Musat, N.; Stumpf, T.; Cherkouk, A.
Bioassociation of uranium on halophilic archaea analyzed with microscopic and spectroscopic methods
Open ProVIS Meetings, June 16, 2016, Leipzig, Germany (2016).

Bader, M.; Müller, K.; Foerstendorf, H.; Swanson, J. S.; Cherkouk, A.
Multistage uranium bioassociation kinetics of two Halobacterium noricense strains under highly saline conditions
BioMetals X (10th International Biometals Symposium), July 10–15, 2016, Dresden, Germany (2016).

Baldova, D.; Fridman, E.; Shwageraus, E.
High Conversion Th-U233 fuel for current generation of PWRs: fuel cycle considerations
PHYSOR 2016, May 01–05, 2016, Sun Valley, ID, U.S.A. (2016).

Barkleit, A.; Heller, A.; Bernhard, G.
Complex formation of europium and curium with the digestive enzyme alpha-amylase
International Conference on Radioanalytical and Nuclear Chemistry (RANC–2016), April 10–15, 2016, Budapest, Hungary (2016).

Barthen, R.; Karimzadeh, L.; Gründig, M.; Schymura, S.; Kulenkampff, J.; Mansel, A.; Lippold, H.; Grenzer, J.; Lippmann-Pipke, J.
Overview of the results from HZDR/IRE in the EcoMetals Project
EcoMetals General Meeting 6, December 07–09, 2016, Hannover, Germany (2016).

Bauer, A.; Schmeide, K.
Untersuchungen zum Komplexierungsverhalten modifizierter Calix[4]arene gegenüber Uran(VI) und Thorium(IV)
Projekttreffen des BMBF Verbundprojektes "SE–FLECX", November 15, 2016, Dresden, Germany (2016).

Baumann, N.
Lectures concerning uranium pollution, time-resolved laser-induced fluorescence spectroscopy (TRLFS), and radiometric dating
Course in Radioecology, Department of Applied Radiation and Isotopes, Faculty of Science, Kasetsart University, February 22–26, 2016, Chatuchak, Bangkok, Thailand (2016).

Bilodid, Y.; Fridman, E.; Kotlyar, D.; Shwageraus, E.
Extension of hybrid micro-depletion model for decay heat calculation in DYN3D code
26th Symposium of AER on VVER Reactor Physics and Reactor Safety, October 10–14, 2016, Helsinki, Finland (2016).

Bilodid, Y.; Kotlyar, D.; Shwageraus, E.; Fridman, E.; Kliem, S.
Microscopic depletion with the correction of microscopic cross sections in nodal diffusion code DYN3D
PHYSOR 2016, May 01–05, 2016, Sun Valley, ID, U.S.A. (2016).

Bok, F.; Moog, H. C.
Oxygen solubility modelling in water and brines
17th International Symposium on Solubility Phenomena and Related Equilibrium Processes (ISSP17), July 24–29, 2016, Geneva, Switzerland (2016).

Bok, F.; Richter, C.; Stockmann, M.; Brendler, V.
Mechanistic sorption models: Species, Thermodynamic, Application
American Chemical Society Spring Meeting, March 13–17, 2016, San Diego, U.S.A. (2016).

Brinkmann, H.; Moll, H.; Arnold, T.
Speciation studies of Rn/Ln with selected degradation products of organic LILW – New spectroscopic insights into the uranyl-acetate system
MIND Project Annual Meeting 2016, May 02–04, 2016, Granada, Spain (2016).

Brinkmann, H.; Moll, H.; Arnold, T.; Stumpf, T.
New spectroscopic insights into the uranyl-acetate system by TRLFS and UV-vis
BioMetals X (10th International Biometals Symposium), July 10–15, 2016, Dresden, Germany (2016).

Fahmy, K.; Fischermeier, L.; Sayed, A.; Pospišil, P.; Solioz, M.; Hof, M.
Water mobility at the active site of an ion transporter
Institut für Medizinische Physik und Biophysik, University Leipzig, February 02, 2016, Leipzig, Germany (2016).

Fahmy, K.; Fischermeier, L.; Sayed, A.; Pospišil, P.; Solioz, M.; Hof, M.
Membrane lateral pressure regulates water mobility at the active site of a copper-transporting ATPase
Seminar in Chemical Biology and Signal Transduction, Rockefeller University, March 08, 2016, New York, U.S.A. (2016).

Fahmy, K.; Obeid, M.; Solioz, M.
Mechanism of attenuation of uranyl toxicity by glutathione in Lactococcus lactis
BioMetals X (10th International Biometals Symposium), July 10–15, 2016, Dresden, Germany (2016).

Fahmy, K.; Obeid, M.; Solioz, M.; Knoeppel, J.; Göttfert, M.; Steppert, M.
Metals in in biomolecules and organisms studied by spectroscopy and calorimetry
Seminar Radioökologie und Strahlenschutz, IRS, December 08, 2016, Hannover, Germany (2016).

Fahmy, K.; Oertel, J.; Gabernet-Garriga, G.
Potential of DNA origami for investigating membrane protein structure and function
German DNA Nanotech Meeting, University Paderborn, October 13, 2016, Paderborn, Germany (2016).

Fahmy, K.; Oertel, J.; Gabernet-Garriga, G.
Water mobility at the active site of an ion transporter
Seminar in Technical and Macromolecular Chemistry, Universitzy Paderborn, May 03, Paderborn, Germany (2016).

Fahmy, K.; Sandoval, A.; Madathil, S.; Böckmann, R.
Proton-induced conformational switching in GPCRs is tailored to the membrane interface
Satellite Meeting Deutschen Gesellschaft für Biophysik, University Erlangen, September 25–29, 2016, Erlangen, Germany (2016).

Fahmy, K.; Sandoval, A.; Madathil, S.; Böckmann, R.
Proton-induced conformational switching in GPCRs is tailored to the membrane interface
Workshop on Lipid protein Interaction, Brücke Most-Stiftung, September 30–October 03, 2016, Dresden, Germany (2016).

Foerstendorf, H.; Comarmond, M. J.; Heim, K.; Steudtner, R.; Stockmann, M.; Payne, T. E.
The ternary sorption system U(VI)/ phosphate/SiO_2: a consistent surface speciation derived from a multimethodological approach
Goldschmidt 2016, June 26–July 01, 2016, Yokohama, Japan (2016).

Foerstendorf, H.; Müller, K.; Tsushima, S.; Steudtner, R.; Kumke, M. U.; Lefèvre, G.; Rothe, J.; Mason, H.; Yang, P.
A Multiple-Technique Round-Robin Test in Actinide Spectroscopy
3rd International Workshop on Advanced Techniques in Actinide Spectroscopy (ATAS 2016), November 07–10, 2016, Richland, U.S.A. (2016).

Franzen, C.; Haubitz, T.; Drobot, B.; Firkala, T.; Brendler, V.; Steudtner, R.
U(VI)–SO_4^{2-} complexation at elevated temperature – a combination of spectroscopy and thermodynamic modeling
Goldschmidt 2016, June 26–July 01, 2016, Yokohama, Japan (2016).

Gerber, U.; Krawczyk-Bärsch, E.; Scheinost, A. C.; Arnold, T.
Reduction of uranium(VI) by isolated, anaerobic microorganisms from the flooding water of the former uranium mine Königstein (Saxony/Germany)
BioMetals X (10th International Biometals Symposium), July 10–15, 2016, Dresden, Germany (2016).

Gerber, U.; Krawczyk-Bärsch, E.; Scheinost, A. C.; Arnold, T.
U(VI) reduction by anaerobic microorganisms isolated from the flooding water of the former uranium mine Königstein (Saxony/Germany)
Goldschmidt 2016, June 26–July 01, 2016, Yokohama, Japan (2016).

Gerber, U.; Röder, G.; Krawczyk-Bärsch, E.; Arnold, T.; Scheinost, A. C.
U(VI) reduction by anaerobic microorganisms isolated from the flooding water of the former uranium mine Königstein (Saxony)
5. Workshop–TransAqua, April 06–07, 2016, Dresden, Germany (2016).

Hellebrandt, S.; Knope, K. E.; Lee, S. S.; Lussier, A. J.; Stubbs, J. E.; Eng, P. J.; Soderholm, L.; Fenter, P.; Schmidt, M.
Cooperative effects of adsorption, reduction, and polymerization observed for hexavalent actinides on the muscovite basal plane
NRC 9–Ninth International Conference on Nuclear and Radiochemistry, August 29–September 02, 2016, Helsinki, Finnland (2016).

Hellebrandt, S.; Knope, K. E.; Lee, S. S.; Lussier, A. J.; Stubbs, J. E.; Eng, P. J.; Soderholm, L.; Fenter, P.; Schmidt, M.
Differential sorption behavior of U(VI) and Pu(VI) dependent on their redox chemistry
Plutonium Futures – The Science 2016, September 18-22, 2016, Baden-Baden, Germany (2016).

Hellebrandt, S.; Knope, K. E.; Lee, S. S.; Lussier, A. J.; Stubbs, J. E.; Eng, P. J.; Soderholm, L.; Fenter, P.; Schmidt, M.
Redox dependent interfacial reactivity of hexavalent radionuclides
2nd Conference on Key Topics in Deep Geological Disposal, September 26–28, 2016, Cologne, Germany (2016).

Hellebrandt, S.; Knope, K. E.; Lee, S. S.; Stubbs, J. E.; Eng, P. J.; Soderholm, L.; Fenter, P.; Schmidt, M.
Redox dependent interfacial reactivity of hexavalent radionuclides
Goldschmidt 2016, June 26–July 01, 2016, Yokohama, Japan (2016).

Hellebrandt, S. E.; Hofmann, S.; Jordan, N.; Barkleit, A.; Schmidt, M.
Incorporation of Eu(III) into Calcite under different Recrystallization conditions
Goldschmidt 2016, June 26–July 01, 2016, Yokohama, Japan (2016).

Hellebrandt, S. E.; Hofmann, S.; Jordan, N.; Schmidt, M.
The Role of Calcite in Nuclear Waste Disposal Sites
2nd Conference on Key Topics in Deep Geological Disposal, September 26–28, 2016, Cologne, Germany (2016).

Hoffmann, A.; Hirsch, T.; Schleicher, E.; Pitz-Paal, R.
Analysis of intermittent flow patterns of water-steam flow in solar thermal power plants with direct steam generation
ICMF–2016 – 9th International Conference on Multiphase Flow, May 22–27, 2016, Florence, Italy (2016).

Höhne, T.; Kliem, S.
IAEA CRP benchmark of ROCOM BORON DILUTION and PTS test cases for the use of CFD in reactor design
Computational Fluid Dynamics for Nuclear Reactor Safety Applications – CFD4NRS–6, September 13–15, 2016, Cambrigde, U.S.A. (2016).

Ikeda-Ohno, A.
Application of solvent extraction to environmental science - Identification of radioactive contaminants in surface water
Interdisciplinary German–Japanese Symposium iJaDe2016 – 2nd German–Japanese Microsymposium "Solvent Extraction: From Fundamentals to Applications", May 10, 2016, Dresden, Germany (2016).

Ikeda-Ohno, A.
Aqueous chemistry of tetravalent cerium (Ce(IV)): Characterisation of polymer and cluster complexes formed *via* hydrolysis
Internal Scientific Seminar at Joint Research Centre – Institute for Transuranium Elements, February 02, 2016, JRC–ITU, Karlsruhe, Germany (2016).

Ikeda-Ohno, A.
Polymer and cluster chemistry of tetravalent cerium (Ce(IV)) in aqueous solutions
UMR Internal Colloquium, July 25, 2016, UMR, Université de Lille, France (2016).

Johansen, M. P.; Caffrey, E.; Child, D. P.; Collins, R.; Hotchkis, M. A. C.; Howell, N. A.; Payne, T. E.; Mokhber-Shahin, L.; Ikeda-Ohno, A.
Particles as concentrated sources related to uptake and radiological dose in mammals
2nd International Conference on Radioecological concentration processes (50 years later), November 09, 2016, Sevilla, Spain (2016).

Johansen, M. P.; Child, D. P.; Collins, R. N.; Hotchkis, M. A. C.; Howell, N. A.; Payne, T. E.; Mokhber-Shahin, L.; Ikeda-Ohno, A.
Analysis of the characteristics of hot particles related to environmental fate and interaction with living organisms
The South Pacific Environmental Radioactivity Association (SPERA) Conference 2016, September 07, 2016, Sanur, Indonesia (2016).

Jordan, N.; Barkleit, A.; Steudtner, R.; Bok, F.; Heller, A.; Brendler, V.
Development of quality-assured Thermodynamic Database for Rare Earth Elements
Goldschmidt 2016, June 26–July 01, 2016, Yokohama, Japan (2016).

Kliem, S.
AER Working Group D on VVER Safety Analysis – Report of the 2016 Meeting
26th Symposium of AER on VVER Reactor Physics and Reactor Safety, October 10–14, 2016, Helsinki, Finland (2016).

Kliem, S.; Hampel, U.; Hurtado, A.; Kästner, W.; Kratzsch, A.; Sahre, P.; Jansen, S.
Forschung und Lehre innerhalb des Kompetenzzentrums Ost für Kerntechnik auf den Gebieten Endlagerung, Reaktorsicherheit und Strahlenschutz
48. Kraftwerkstechnisches Kolloquium, October 18–19, 2016, Dresden, Germany (2016).

Kögler, T.; Beyer, R.; Junghans, A. R.; Müller, S.
Fast neutron-induced fission at the time-of-flight facility nELBE
ND2016 – International Conference on Nuclear Data for Science and Technology, September 11–16, 2016, Bruges, Belgium (2016).

Konheiser, J.; Müller, S. E.
Studies of activation monitors at the HZDR medical cyclotron: Simulation and Experiment
16th AAA Workshop, December 05, 2016, Garching, Germany (2016).

Krawczyk-Bärsch, E.; Schmeide, K.; Rossberg, A.; Scheinost, A. C.
U and Np uptake on biogenic and abiotic ferrihydrite – a comparison by EXAFS spectroscopy
Goldschmidt 2016, June 26–July 01, 2016, Yokohama, Japan (2016).

Kulenkampff, J.; Gründig, M.; Zakhnini, A.; Lippmann-Pipke, J.
Quantitative observation of tracer transport with high-resolution PET
European Geosciences Union General Assembly 2016 (EGU 2016), April 17–22, 2016, Vienna, Austria (2016).

Lehmann, S.; Bok, F.; Ikeda-Ohno, A.; Muñoz, A. G.
Redox Stability of Uranium in High Ionic Strength Media: An Electrochemical and Spectroscopic Study
PRIME 2016 – Pacific Rim Meeting on Electrochemical and Solid-State Science, October 02–07, 2016, Honolulu, Hawaii, U.S.A.

Lehmann, S.; Steudtner, R.; Brendler, V.
Speciation of tetravalent uranium with inorganic ligands in aqueous solution investigated by UV/vis and time-resolved laser-fluorescence measurements
NRC 9 – Ninth International Conference on Nuclear and Radiochemistry, August 29–September 02, 2016, Helsinki, Finnland (2016).

Lippmann-Pipke, J.; Eichelbaum, S.; Kulenkampff, J.
Spatiotemporal image analysis of water flow in porous media for numerical transport modelling
80. Jahrestagung der DPG und DPG–Frühjahrstagung, March 06–11, 2016, Regensburg, Germany (2016).

Lippmann-Pipke, J.; Karimzadeh, L.; Blanc, P.; Eichelbaum, S.; Schymura, S.; Rogóż, T.; Frühwirt, K.; Kulenkampff, J.
Reactive transport modelling based on velocity fields obtained on drill core scale
IMWA 2016 – Annual Conference of the International Mine Water Association, July 14, 2016, Leipzig, Germany (2016).

Martin, N.; März, J.; Henry, N.; Volkringer, C.; Ikeda-Ohno, A.; Hennig, C.; Loiseau, T.
Coordination polymers of tetravalent neptunium with aromatic polycarboxylate ligands
Plutonium Futures 2016, September 18–22, 2016, Baden–Baden, Germany (2016).

März, J.
Coordination chemistry of tetravalent actinides
8th International Workshop on „Coordination Chemistry of Metals with Medical Relevance and Supramolecular Building Blocks“, May 26–27, 2016, Berlin, Germany (2016).

März, J.; Schöne, S.; Radoske, T.; Kaden, P.
FENABIUM: Research at HZDR
FENABIUM Kick–off Meeting, November 14, 2016, Dresden, Germany (2016).

Mansel, A.
Flüssig-Flüssig-Extraktion von Seltenen Erden mit Hilfe von Calix[4]arenen
Projekttreffen des BMBF Verbundprojektes „SE-FLECX“, May 19, 2016, Freiberg, Germany (2016).

Mansel, A.
Flüssig-Flüssig-Extraktion von Seltenen Erden und Zirkonium mit Hilfe von Calix[4]arenen
Projekttreffen des BMBF Verbundprojektes „SE-FLECX“, November 15, 2016, Dresden, Germany (2016).

Matschiavelli, N.; Steglich, J.; Arnold, T.; Cherkouk, A.
Microbial Influence on Bentonite-Transformation
MIND Project Annual Meeting, May 03–04, 2016, Granada, Spain (2016).

Matschiavelli, N.; Steglich, J.; Kluge, S.; Arnold, T.; Cherkouk, A.
Microbial Influence on Bentonite Transformation
UMB–Projekttreffen, June 02, 2016, Braunschweig, Germany (2016).

Müller, K.
In-situ spectroscopic identification of actinide(V/VI) sorption complexes at the mineral oxide water interface
Kyoto University, November 29, 2016, Kyoto, Japan (2016).

Müller, S. E.
Activation studies at the HZDR medical cyclotron: Simulation and Experiment
FLUKA collaboration meeting, October 17–18, 2016, CERN (Geneva), Switzerland (2016).

Müller, S. E.; Fassò, A.; Ferrari, A.; Ferrari, A.; Mokhov, N. V.; Nelson, W. R.; Roesler, S.; Sanami, T.; Striganov, S. I.; Versaci, R.
Update of the code intercomparison and benchmark for muon fluence and absorbed dose induced by a 18 GeV electron beam after massive iron shielding
SATIF13 – 13th Meeting of the task– force on Shielding aspects of Accelerators, Targets and Irradiation Facilities, October 10–12, 2016, Dresden, Germany (2016).

Nikitin, E.; Fridman, E.
Axial fuel rod expansion model in nodal code DYN3D for SFR application
PHYSOR 2016, May 01–05, 2016, Sun Valley, ID, U.S.A. (2016).

Patzschke, M.
Analysing Actinide Bonds in Position Space
ChemBond 2016 – Chemical Bonding in Position Space, November 27–December 01, 2016, Dresden, Germany (2016).

Patzschke, M.
Computational chemistry for actinide compounds: examine the U-U bond inside fullerenes
Eingeladener Vortrag Universität Hannover, April 13, 2016, Hannover, Germany (2016).

Patzschke, M.
How can Theoretical Chemistry contribute to coordination chemistry?
8th International Workshop on “Coordination Chemistry of Metals with Medical Relevance and Supramolecular Building Blocks“, May 26, 2016, Berlin, Germany (2016).

Patzschke, M.
How To Analyze The Electronic Density - An Introduction To Some Useful Tools
CSC Spring School 2016, March 11, 2016, Helsinki, Finnland (2016).

Patzschke, M.
Probing the chemical bond: The case of caged U_2
GöCH Vortrag Linz, February 29, 2016, Linz, Austria (2016).

Patzschke, M.
Quantum Chemistry Workshop - Using Orca & Gabedit
CSC Spring School 2016, March 09, 2016, Helsinki, Finland (2016).

Patzschke, M.
Uranyl Spectroscopy - Do We Know Everything?
IX MMQC Mariapfarr Workshop on Theoretical Chemistry, February 26, 2016, Mariapfarr, Austria (2016).

Patzschke, M.
Visualising Your Results - An Introduction to VMD
CSC Spring School 2016, March 10, 2016, Helsinki, Finland (2016).

Philipp, T.; Schmeide, K.
Uranium(VI) retention by Ca-bentonite under (hyper)alkaline conditions
3. Workshop des BMWi–Verbundvorhabens “Geochemische Radionuklidrückhaltung an Zementalterationsphasen (GRaZ)“, October 25–26, 2016, Heidelberg, Germany (2016).

Philipp, T.; Wolter, J. M.
Erste Untersuchungen zur Uranrückhaltung an C-S-H-Phasen und Ca-Bentonit
2. Workshop des BMWi–Verbundvorhabens "Geochemische Radionuklidrückhaltung an Zementalterationsphasen (GRaZ)", March 22–23, 2016, Munich, Germany (2016).

Pollmann, K.; Raff, J.; Hopfe, S.; Kostudis, S.; Matys, S.; Bertheau, R.; Lehmann, F.; Suhr, M.; Vogel, M.; Flemming, K.; Schönberger, N.; Kutschke, S.
New "green" biotechnical concepts for the recovery of metals from primary and secondary resources
Green & Sustainable Chemistry, April 04–06, 2016, Berlin, Germany (2016).

Raff, J.; Vogel, M.; Drobot, B.; Schmoock, C.; Moll, H.; Barkleit, A.; Börnick, H.; Worch, E.; Stumpf, T.
Bacterial S-layer proteins and their interaction with radionuclides
Frontiers in Environmental Radioactivity, January 06–07, 2016, London, U. K. (2016).

Raff, J.; Vogel, M.; Günther, A.; Wollenberg, A.; Stumpf, T.
Microbial biomineralization of uranium and its application
Goldschmidt 2016, June 26–July 01, 2016, Yokohama, Japan (2016).

Raff, J.; Vogel, M.; Schmoock, C.; Günther, A.; Moll, H.; Drobot, B.; Lederer, F.; Li, B.; Foerstendorf, H.; Börnick, H.; Pollmann, K.; Worch, E.; Stumpf, T.
Molecular interaction of radio-metals with microorganisms
Institutsseminar des Instituts für Nukleare Entsorgung, Karlsruher Institut für Technologie, November 08, 2016, Eggenstein–Leopoldshafen, Germany (2016).

Sallat, M.; Raff, J.
Proteine als neue Bausteine für funktionalisierte Textilverbunde
24. Neues Dresdner Vakuumtechnisches Kolloquium, September 29–30, 2016, Dresden, Germany (2016).

Scheinost, A. C.
Application of X-ray absorption spectroscopy to actinide research
11th School on the Physics and Chemistry of the Actinides, March 13–16, 2016, Grenoble, France (2016).

Schmeide, K.; Scheinost, A.C.
Different oxidation states of Tc in solid state compounds and surface complexes – an XAS study.
8th International Workshop on „Coordination Chemistry of Metals with Medical Relevance and Supramolecular Building Blocks". May 26–27, 2016, Berlin, Germany (2016).

Schymura, S.; Fricke, T.; Hildebrand, H.; Franke, K.
Environmental transformation of CeO_2 Nanoparticles – Elucidating the role of dissolution by smart radiolabeling
Nanosafe 2016, November 07–10, 2016, Grenoble, France (2016).

Schymura, S.; Fricke, T.; Hildebrand, H.; Franke, K.
Radiolabelling of nanoparticles for the use in environmental fate studies in waste water treatment and beyond
CYCLEUR 2016, June 23–24, 2016, Bern, Switzerland (2016).

Schymura, S.; Kulenkampff, J.; Franke, K.; Lippmann-Pipke, J.
Hindrance in MWCNT nanofluid flow through porous media observed by PET
Interpore – First German National Chapter Meeting, December 05–06, 2016, Leipzig, Germany (2016).

Smith, A. L.; Raison, P. E.; Y. Colle, J.; Colineau, E.; Griveau, J. C.; Hen, A.; Beneš, O.; Guéneau, C.; Martin, P.; Prieur, D.; Martel, L.; Magnani, N.; Caciuffo, R.; Sanchez, J. P.; Charpentier, T.; Scheinost, A. C.; Hennig, C.; Kvashnina, K.; Suard, E.; Wallez, G.; Cheetham, A. K.; Konings, R. J. M.
The peculiar chemistry of the nuclear fuel-sodium coolant interaction
NuMat2016: The Nuclear Materials Conference, November 07–10, 2016, Montpellier, France (2016).

Steudtner, R.; Drobot, B.; Haubitz, T.; Lehmann, S.; Vogel, M.
Luminescence spectroscopy of uranium
Institutskolloquium, July 27, 2016, Karlsruhe, Germany (2016).

Steudtner, R.; Drobot, B.; Haubitz, T.; Schernikau, M.; Lehmann, S.; Bader, M.; Vogel, M.
Luminescence spectroscopy of An/Ln in environmental systems
3rd International Workshop on Advanced Techniques in Actinide Spectroscopy (ATAS 2016), November 07–10, 2016, Richland, U.S.A. (2016).

Stockmann, M.; Becker, D.; Flügge, J.; Schikora, J.; Noseck, U.; Brendler, V.
Smart K_d-concept for realistic description of sorption processes
DAEF 2016 – 2nd Conference on Key Topics in Deep Geological Disposal – Challenges of a Site Selection Process: Society – Procedures – Safety, September 26–28, 2016, Cologne, Germany (2016).

Stockmann, M.; Brendler, V.; Flügge, J.; Noseck, U.
Multidimensional "smart K_d-matrices" for realistic description of sorption processes
Water–Rock Interaction, October 16–21, 2016, Évora, Portugal (2016).

Stumpf, T.
Understanding actinide reactivity at the water-mineral interface
Frontiers in Environmental Radioactivity 2016, January 06–07, 2016, London, U.K. (2016).

Stumpf, T.
Understanding actinide reactivity at the water-mineral interface
Les Journées Nationales de Radiochimie et de Chimie Nucléaire (JNR) 2016, September 08–09, 2016, Nice, France (2016).

Swanson, J.; Cherkouk, A.; Bader, M.; Reed, D.
The microbiology of subsurface, salt-based nuclear waste repositories: Toward a realistic prediction of the microbial effects on repository performance
Halophiles 2016, May 22–27, 2016, San Juan, Puerto Rico (2016).

Tsushima, S.; Ishikawa, T.; Tanaka, S.; Mori, H.; Saeki, M.; Nakano, T.; Komeiji, Y.; Mochizuki, Y.
Fragment molecular orbital (FMO) method for studying actinide interaction with DNAs and proteins
3rd International Workshop on Advanced Techniques in Actinide Spectroscopy (ATAS 2016), November 07–10, 2016, Richland, U.S.A. (2016).

Virtanen, S.; Eibl, M.; Meriläinen, S.; Rossberg, A.; Lehto, J.; Rabung, T.; Huittinen, N.
Sorption competition of trivalent metals on corundum (α-Al_2O_3) studied on the macro- and microscopic scale
NRC 9 – Ninth International Conference on Nuclear and Radiochemistry, August 29–September 02, 2016, Helsinki, Finnland (2016).

Vogel, M.; Drobot, B.; Günther, T.; Lehmann, F.; Weinert, U.; Pollmann, K.; Raff, J.
Insights into the use of specific metal binding of self-assembling S-layer proteins
Materials Science and Engineering – MSE 2016 Congress, September 27–29, 2016, Darmstadt, Germany (2016).

Wilke, C.; Barkleit, A.; Ikeda-Ohno, A.; Stumpf, T.
Spectroscopic studies on the interaction of europium(III) and curium(III) with components of the human mucosa
BioMetals X (10th International Biometals Symposium), July 10–15, 2016, Dresden, Germany (2016).

Wilke, C.; Barkleit, A.; Stumpf, T.
Spectroscopic screening for the speciation of europium and curium in the gastrointestinal tract
RANC–International Conference on Radioanalytical and Nuclear Chemistry, April 10–15, 2016, Budapest, Hungary (2016).

Wilke, C.; Raff, J.; Barkleit, A.; Ikeda-Ohno, A.; Stumpf, T.
Interaction of Eu(III) and Cm(III) with mucin – a key component of the human mucosa
Goldschmidt 2016, June 26–July 01, 2016, Yokohama, Japan (2016).

Wolter, J. M.
Leaching of uranium(VI) doped CSH phases in high saline water
3. Workshop des BMWi–Verbundvorhabens "Geochemische Radionuklidrückhaltung an Zementalterationsphasen (GRaZ)", October 25–26, 2016, Heidelberg, Germany (2016).

Wolter, J.-M.; Schmeide, K.; Stumpf, T.
Stability of uranium(VI) doped CSH phases in high saline water
Kompetenzzentrum Ost für Kerntechnik (KOMPOST), 11. Seminar für Doktoranden und Nachwuchswissenschaftler im HZDR, 08.12.2016, Dresden, Germany (2016).

Zesewitz, K.; Schmidt, M.
Spatially-resolved sorption studies of Eu(III) on granite surface with time-resolved laser fluorescence microscopy (TRLFM)
3rd International Workshop on Advanced Techniques in Actinide Spectroscopy (ATAS 2016), November 07–10, 2016, Richland, U.S.A. (2016).

In addition, more than 30 posters were presented at international conferences and workshops.

PATENT

Fahmy, K.; Tsushima, S.; Attia, E.
P1408 - Photochemische Entfernung von Uran(VI)-Verbindungen aus mit Uran(VI)-verschmutzten Flüssigkeiten
DE102014225951 – Grant Feb. 04, 2016.

THESES

DOCTORAL THESES

(Technische Universität Dresden, 2016)

Drobot, B.
Entwicklung und Validierung mathematischer Methoden zur Auswertung spektroskopischer Daten der Uranyl(VI)–Hydrolyse

Heine, K.
Bindung von U(VI) an Milchproteinen und Modellpeptide

Obeid, M.
Assessment of Low–Dose Radiotoxicity in Microorganisms and Higher Organisms

Richter, C.
Sorption of environmentally relevant radionuclides (U(VI), Np(V)) and lanthanides (Nd(III)) on feldspar and mica

Ulbricht, I.
Bildung von Kolloiden des tetravalenten Urans unter Einfluss von Silikat in neutralen und schwachalkalischen wässrigen Systemen

MASTER THESES

(Technische Universität Dresden, 2016, except where noted)

Balakrishnan, A.
Spectroscopic investigation of cysteines in CopA from *Legionella pneumophila*

Eibl, M.
Sorptions- und Inkorporationsuntersuchungen von Actiniden an Korund und Zirkonium(IV)-oxid

Lehrich, J.
Untersuchungen zur Wechselwirkung von Uran und Neptunium mit *Gallionella ferruginea*-dominierenden Biofilmen und deren Fe-Präzipitaten
Technische Universität Bergakademie Freiberg, Freiberg, Germany (2016).

Lösch, H.
Site-selektive Fluoreszenz-Spektroskopie Untersuchungen an $LnPO_4$-Keramiken für endlagerrelevante Zwecke
University of Applied Sciences, Dresden, Germany (2016).

Neumann, J.
Charakterisierung der Sorption dreiwertiger Actiniden (Am, Cm) und ihrer Seltenerdhomologe (Eu, Y) an Feldspäte mittels TRLFS und CTR/RAXR

Röder, G.
Die Isolierung acidophiler Mikroorganismen aus dem Flutungswasser der ehemaligen Uranmine der Wismut in Königstein und deren mögliches Potential lösliches Uran zu immobilisieren
Technische Universität Bergakademie Freiberg, Freiberg, Germany (2016).

Radoske, T.
Komplexe vierwertiger Actinide – Iminligand Salen und Derivate

Schöne, S.
Vierwertige Actinidkomplexe chiraler Benzamidinate – Synthese und Charakterisierung

Steglich, J.
Untersuchungen zum mikrobiellen Einfluss auf das Barrierematerial Bentonit
International Institute Zittau – Technische Universität Dresden

Subramanian, M.
Assembly of lipid nanoiscs on DNA origami platform

Wollenberg, A.
Untersuchung der molekularen Wechselwirkungen von Uran(VI) und Europium(III) mit mycelbildenden Pilzen

BACHELOR THESES

Haubitz, T.
Einfluss von Sulfat auf die Uran(VI)-Speziation im aquatischen System
Brandenburgische Technische Universität Cottbus - Senftenberg, Germany (2016).

Wendisch, M.
Identifizierung von Europium-Spezies in Grundwässern des Deckgebirges Gorleben mit Hilfe spektroskopischer Verfahren und thermodynamischer Modellierung
Hochschule Zittau-Görlitz, Germany (2016).

- BioMetals 2016
- Thul Summer School
- Thermac Workshop
- Seminars
- Workshop, Sessions
- Awards
- Teaching Activities

BioMetals X
10TH International Biometals Symposium 2016

Art'otel dresden, Dresden, Germany, July 10–15, 2016

In July 2016, the IRE organized the 10th International Biometals Symposium, "BioMetals 2016" in Dresden. The International Conference on Biometals is a member in a series of conferences organized since 1997, the first one taking place in Calgary, Canada.
At this meeting, 115 international colleagues from over 22 countries on five continents participated. The conference venue was located at the art'otel in the inner city of Dresden. Thirteen invited lectures, about 60 contributed short talks, and over 35 posters were presented at the conference. The interdisciplinary theme of the conference was the exploration of metals in biology, medicine and the environment. BioMetals 2016 offered several sub-themes: Coordination Chemistry and Environmental Issues, Acquisition, Signaling and Diseases, Metal Transport, Zinc and Iron, Metals and Regulation, Redox of Metals, Sensors, Plants and Eukaryotes, Toxicity, Defense. A special focus at the conference in Dresden was set to "Radionuclides". Furthermore, a "Young Scientists Session" was included for the first time.
Due to a large number of sponsors it was possible to mark several presentations with awards. For oral presentations, two "Jorge and Lydia Crosa Awards" were bestowed. In addition, two awards for oral presentations of young scientists were sponsored by "Carl Zeiss Microscopy Inc.". Last but not least four posters were awarded.
A special thank we send to the International Scientific Committee from the international Biometals Society, Pierre Cornelis, Günther Winkelmann, Larry Barton, Manuel Lemos, Wolfgang Maret, Christopher Rensing, Frank Thévenod and Hans Vogel, for their advice in designing the scientific program. Also the administrative assistance of Andrea Witschel and Heike Dürichen from Intercom should be named for her dedication and skill in synchronizing all aspects of this conference.

(by: G. Geipel)

List of keynote and invited speakers:

Berthomieu, Catherine
CEA Caderach, France
Engineering of recombinant EF-hand peptides for the selective binding of radionuclides

Baker, Alan
University of Melbourne, Australia
Metallophytes:a biodiversity and phytotechnological resource for soil clean-up, phyto-/agromining and mine site restoration

Krämer, Ute
University of Bochum, Germany
Metal hyperaccumulation in plants: Novel insights from genome-wide and targeted molecular approaches

Kumke, Michael
Universität Potsdam, Germany
Lanthanides and optical sensing

Maret, Wolfgang
King's College London, U.K.
Cellular Zinc homeostasis in Diabetes Type 2

Raymond, Ken
University of California, U.S.A.
Coordination Chemistry of Microbial Iron Transport

Rensing, Christopher
University of Kopenhagen, Denmark
Copper and Zinc – Poisioning in Protozoan Grazing

Robinson, Nigel
University of Durham, U.K.
Further characterisation of the Ni(II)-sensor InrS and the effect of adjusting $K_{Ni(II)}$

Salt, David
University of Aberdeen, U.K.
The root endodermis acts as a gateway for solute transport to the shoot

Verbruggen, Natalie
Université libre de Bruxelles, Belgium
CAX1 co-segregates with Cd tolerance in the metal hyper-accumulator *Arabidopsis halleri* and CAX1 is involved in Ca-dependent limitation of oxidative stress

Wittung-Stafshede, Pernilla
Chalmers University Gothenburg. Sweden
Protein Interactions that Facilitate Copper Ion Transport in the Human Cytoplasm

ThUL School in Actinide Chemistry 2016

HZDR, Dresden, Germany, September 19–23, 2016

Quantum chemical approaches in actinide sciences are often the basis of thorough interpretation of scientific data. However, the ab-initio calculation of application-relevant compounds in silico is limited by the number of electrons present in these systems. A vast number of different approaches to simplify the description of such systems have been developed recently. The "ThUL school in Actinide Chemistry" fosters the interaction between experimental and computational actinide chemistry and physics by bringing together experimentalists and theoretical chemists. An integral part of this school is the education of young scientists, such as Ph. D. students or early stage postdoctoral scientists.

Theoretical chemistry is a comparatively new research area in chemistry. In the last century enormous progress has been made in understanding the electronic structures of molecules. Almost every publication nowadays has a theory section. This means, that all chemists have to understand the basics of quantum chemistry.
The *f*-elements, and especially the actinides are very challenging to treat computationally. The reason for this is threefold:

1) Each actinide atom adds a lot of electrons to the system. As computational methods get much more time consuming when the amount of electrons in the system is increased, special care has to be taken to make the computations as efficient as possible.
2) Actinides, especially the later ones in low oxidation states contain many unpaired electrons, making many of the actinide-containing species multi-reference cases, where simple computational methods do not work.
3) For heavy elements including actinides, the expectation value of the speed of the innermost electrons approaches the speed of light. This means, normal quantum-chemical methods as used for light elements will not work, as spin-orbit effects get more important.

To improve the understanding between experimentalists and theoreticians working in the field of actinide chemistry and physics, the purpose of this school was to explain the basic concepts of computational actinide chemistry to the participants. At the same time the introduction of some of the basic spectroscopic techniques allowed the participants to exchange their ideas more freely.
Following the tradition of previous successful schools in Lille (2006), in Cadarache (2007) and a yearly instalment from 2012 to 2015 in Karlsruhe, this years' ThUL school in Actinide Chemistry was held from September 19–23, 2016, in Dresden for the first time. Renowned speakers from all over Europe from the fields of theory and experiment introduced the audience of mainly PhD students and Postdocs to quantum theory in actinide science. A joint poster session with colleagues from The University of Manchester, hand-on training sessions with a number of quantum chemical codes in the afternoons and extensive discussions in the evenings made 2016's ThUL school a huge success!

(by: M. Patzschke and P. Kaden)

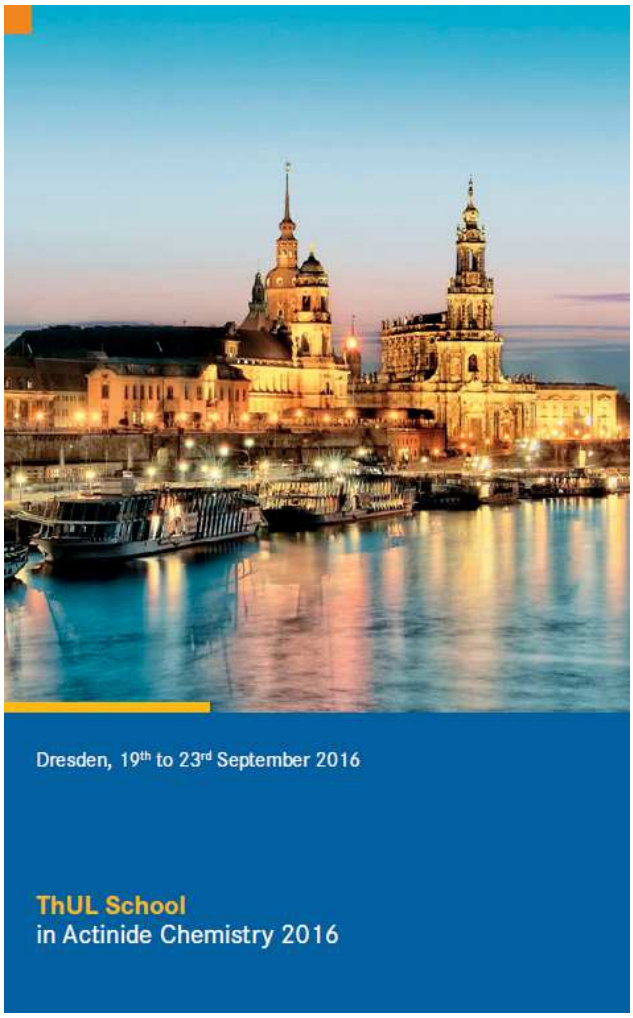

List of lectures:

Bahmann, Hilke
Technische Universität Berlin, Berlin, Germany
Development of DFT functionals, local hybrids

Baranov, Alexey
Max Planck Institut for Chemical Physics of Solids, Dresden, Germany
Chemical bonding in solids relativistic electron localisabilty

Huittinen, Nina
TRLFS in actinide sorption and incorporation investigations

Ikeda-Ohno, Atsushi
X-ray absorption spectroscopy for actinide chemistry – Basics, experiments and application

Kerridge, Andrew
University of Lancaster, Lancaster, U.K.
Multi-reference calculations for f-elements, treatment of near-degenerate electronic states, spectroscopical data from calculations

Natrajan, Louise
University of Manchester, Machester, U.K.
Luminescence and fluorescence spectroscopy, two-photon excitation

Patzschke, Michael
Introduction to Relativistic Effects in Quantum Chemistry I–III

Introduction to ADF

Orca & Gabedit

Polly, Robert
Karlsruhe Institute of Technology, Institute for Nuclear Waste Disposal, Karlsruhe, Germany
Computational surface-molecule interaction

Straka, Michal
Academy of Sciences of the Czech Republic, Prague, Czechia
Relativistic effects in heavy elements, computational spectroscopy

Trumm, Michael
Karlsruhe Institute of Technology, Institute for Nuclear Waste Disposal, Karlsruhe, Germany
Molecular dynamics for actinides, computational spectroscopy

Vallet, Valérie
University of Lille, Lille , France
Electronic structure of heavy elements, spectroscopy, molecular dynamics for actinides

❍ MIDTERM THERMAC PROJECT WORKSHOP

HZDR, Dresden, Germany, December 01–02, 2016

Repositories for highly active heat producing waste will feature elevated temperatures over a significant period after closure. If early canister failure occurs, radionuclides therefore may contact aquatic systems at higher temperatures. For such conditions, the chemical understanding and available thermodynamic database for actinides, long-lived fission products and relevant matrix elements in aquatic systems has to be improved. To this end, a systematic use of estimation methods for thermodynamic data and model parameters will be compared to comprehensive experimental results. This allows for the validation of the estimations and quantum-chemistry based information. In addition, fundamental studies for improved process understanding of actinide chemistry at elevated temperatures are performed. Final goal is the assessment of estimation methods to set up a workable thermodynamic database for elevated temperatures with high applicability to topics relevant for nuclear waste disposal. Furthermore, it will be clarified, to which extent systems will remain critical with regard to available thermodynamic data, and which relevant processes at elevated temperatures are still not sufficiently understood.
The collaborative project "Aquatic Actinide Chemistry and Thermodynamics at Elevated Temperatures" addresses these questions. It bundles the expertise of eight research institutions from Germany, Spain and Switzerland, started in March 2015, and is funded by the German Federal Ministry of Education and Research under the grants 02NUK039A, B, C, D, E.
Participants came from 10 European countries, the US and the Republic of Korea. They represented 25 research institutions, a small enterprise and four waste management organizations. Their contributions led to 15 talks and a mini poster session.

(by: V. Brendler)

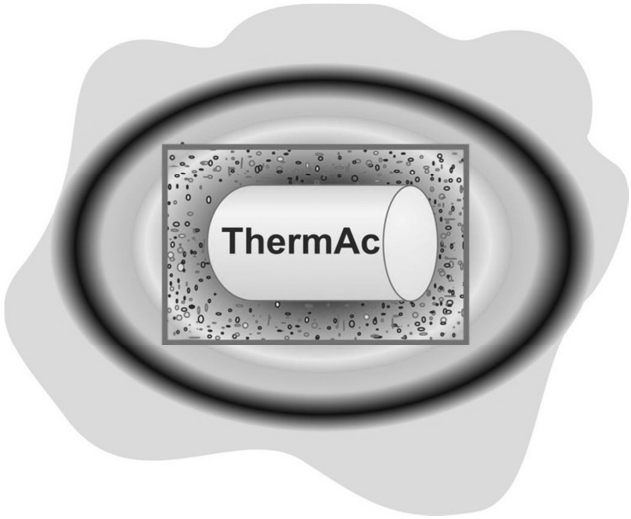

List of invited speakers:

Made, Benoit
Agence nationale pour la gestion des déchets radioactifs - ANDRA, Paris, France
Effect of the increase in temperature in the assessment of actinides behavior in the near field of storage : Approach in "ThermoChimie" database

Plyasunov, Andrey
Russian Academy of Science, Institute of Experimental Mineralogy, Chernogolovka Russia
Simple methods of short (up to 200 °C) temperature extrapolation of equilibrium constants in aqueous media

Powell, Brian
Clemson University, Anderson, SC, U.S.A.
Quantifying Eu, Np, U, and Pu sorption to hematite at elevated temperatures: variable temperature batch sorption and calorimetry studies

Voigt, Wolfgang
Technische Bergakademie Freiberg, Germany
Continuous description or model switch – activity coefficient models in broad concentration – temperature ranges

SEMINARS (TALKS OF VISITORS)

Gal, Assaf
Max Planck Institute of Colloids and Interfaces, Potsdam, Germany
Biomineralization pathways in coccolithophores - tiny algae that shape the earth
January 11, 2016

Tournassat, Christophe
BRGM, Orléans, France
Radionuclide transport in nano-porous clays with consideration of electrostatic effects
January 13, 2016

Bruggeman, Christophe
SCK•CEN, Belgium
Overview of the different nuclear waste disposal related R&D activities conducted at the Belgian Nuclear Research Centre, SCK•CEN
January 25, 2016

Lusa, Merja
University of Helsinki, Helsinki, Finland
Microbial studies related to the final disposal of spent nuclear fuel in Finland
February 08, 2016

Kremleva, Alena
Technische Universität München, Munich, Germany
Quantum chemical modeling of actinide adsorption on solvated clay mineral surfaces. Improved species, structures, and energies from low temperature annealing
March 15, 2016

Steppert, Michael
Leibniz Universität Hannover, Hanover, Germany
The nano-ESI and DESI source Orbitrap mass spectrometer: fundamentals and possible applications
May 18, 2016

Jivkov, Andrey
University of Manchester, Manchester, U.K.
Discovering materials performance with evolving graphs
May 23, 2016

Vitova, Tonya
KIT Institut für Anorganische Chemie, Karlsruhe, Germany
Structural investigations of actinides with high energy resolution X-ray absorption spectroscopy
June 15, 2016

Fenske, Dieter
KIT Institut für Anorganische Chemie, Karlsruhe, Germany
Neue nanoskalige Münzmetallcluster
June 18, 2016

Gomez, Armando
ININ Mexico
Fast reactor and reactor analysis activities at ININ
August 26, 2016

Holliday, Kiel S.
Lawrence Livermore National Laboratory, Livermore, CA, U.S.A.
Composition and Redox Conditions in Historic Nuclear Fallout
September 16, 2016

Mathur, Sanjay
Universität Köln, Cologne, Germany
Chemically Processed Inorganic Nanostructures for Energy and Health Applications
November 9, 2016

Marques Fernandes, Maria do Sameiro
Paul Scherrer Institut, Villigen, Switzerland
Adsorption of (radio-)contaminants on clays: over-view of the activities at PSI
December 16, 2016

WORKSHOPS & SESSIONS

Bilateral meeting

Institut für Radioökologie und Strahlenschutz
Leibniz Universität Hannover, Germany

Institute of Resource Ecology (IRE)
HZDR, Dresden, Germany

HZDR, Dresden, Germany, June 23–24, 2016.

Barkleit, A.
Speciation of trivalent actinides and lanthanides in body fluids

Bosco, H.
SIMS and SNMS for applications in ultra-trace analysis

Ebert, E.
Speciation of U (and Ra): Verification of a database by modeling techniques and comparative experiments

Fahmy, K.
Metal protein interactions: from molecules to organisms

Gerber, U.
Biological reduction of uranium(VI) by anaerobic microorganisms isolated from the former uranium mine Königstein

Jordan, N.
Development of a Quality-Assured Thermodynamic Database for Rare Earth Elements

Pönitz, E.
Calculation of Dose Rates at the Surface of Storage Containers for High-Level Radioactive Waste

Schmeide, K.
Different oxidation states of Tc in solid state compounds and surface complexes – An XAS study and some backgrounds

Steinhauser, G.
Radionuclide analysis after the Fukushima nuclear accident

Tawussi, F.
Influence of the speciation of radionuclides on their plant uptake

Wunnenberg, A.
Investigations on the uptake of ^{243}Am in (plant) cells

Zesewitz, K.
Spatially-resolved speciation of Eu(III) on granite with TRLFS

Goldschmidt 2016 – Session coorganized by IRE

Yokohama, Japan, June 26–July 1, 2016.

Benedetti, M. F.; Foerstendorf, H.; Jordan, N.; Reiller, P.; Sasaki, T.; Takumi, S.; Zavarin, M.
Session 10j:
Environmental Processes Governing the Dissemination of Radionuclides from Energy Production

Bilateral meeting

University of Manchester
Manchester, U.K.

Institute of Resource Ecology (IRE)
HZDR, Dresden, Germany

HZDR, Dresden, Germany, September 19–20, 2016.

Brendler, V.
Combining spectroscopy and thermodynamics: A pathway to robust geochemical models

Cherkouk, A.
Microbial processes in potential nuclear waste repositories

Fahmy, K.
Metal-protein interactions: From molecules to organisms

Huittinen, N.
Eu^{3+} and Cm^{3+} incorporation in monazite ceramics for conditioning of radioactive wastes

Ikeda-Ohno, A.
Basic research on f-elements at HZDR-IRE

Kaltsoyannis, N.
Research in the Kaltsoyannis group

Kuippers, G.
The impact of isosaccharinic biodegradation on the mobility of radionuclides and heavy metals

Lloyd, J.
Geomicrobiology of the nuclear fuel cycle

Mills, D.
Thorium redox chemistry and a new way to measure actinide covalency by pulsed EPR spectroscopy

Morris, K.
The impact of microbial processes on radionuclide speciation and fate

Natrajan, L.
A spectroscopic foray into the redox chemistry of the early actinides

Patzschke, M.
Computational f-element chemistry at HZDR

Shaw, S.
Mineral formation and radionuclide sequestration: Applications in effluent treatment and geodisposal systems

AWARDS

Poster Awards

Bauer, A.
Complexation studies of modified calix[4]arenes with uranium in non-aqueous solution
NRC9 – The Ninth International Conference on Nuclear and Radiochemistry, August 29–September 02, 2016, Helsinki, Finland (2016).

Raff, J.
Ecological and industrial aspects of the interaction of radionuclides with bacterial S-layer proteins
Annual Conference of the Association for General and Applied Microbiology (VAAM), March 13–16, 2016, Jena, Germany (2016).

TEACHING ACTIVITIES

(Winter term: WT; Summer term: ST)

Lectures

Brendler, V./Huittinen, N.
Dresden University of Applied Sciences, ST 2016
Radiochemistry

Fahmy, K.
Technische Universität Dresden, WT 2015/16
Biophysical methods

ST 2016
Biological thermodynamics

Franzen, C.
Technische Universität Dresden, ST 2016
Environmental chemistry

Lippold, H.
Universität Leipzig, ST 2016
Radioanalytik

Entstehung und Eigenschaften ionisierender Strahlung

Raff, J.
Dresden University of Applied Sciences, WT 2015/16, WT 2016/2017
Mikrobiologie

Technische Universität Dresden, WT 2016/2017
Mikrobielle Laugung

Universität Granada, WT 2016/17
An example for nature´s genius: Surface layer (S-layer) proteins

Universität Granada, ST 2016
Bacterial surface layers (S-layers): interface to the environment and platform for the development of new materials

Schmidt, M.
Technische Universität Dresden, WT 2016/17
Chemistry of *f*-elements

Stumpf, T.
Technische Universität Dresden, ST 2016
Radiochemistry

Courses

- The laboratory course "Radiochemistry" was provided from September 04–09 and from September 12–16, 2016, as a part of a module of the chemistry master degree program at the Technische Universität Dresden.

Advisers:

Bader, M.	Dr. Kaden, P.
Barthen, R.	Lehmann, S.
Bauer, A.	Dr. Patzschke, M.
Brinkmann, H.	Philipp, T.
Fischer, S.	Dr. Schmidt, M.
Franze, M.	Schrader, S.
Gerber, U.	Weiss, S.
Hellebrandt, S.	Wilke, C.
Dr. Huittinen, N.	Wolter, J.
Dr. Jordan, N.	Zesewitz, K.

- The IRE provided the experiment "Alpha spectrometric isotope dilution analysis of uranium" of the laboratory course "Instrumental Analysis" held by the Institute for Analytical Chemistry, Technische Universität Dresden.

Advisers:

WT 2015/16	*WT 2016/17*
Bader, M.	Philipp, T.
Bauer, A.	Wollenberg, A.
Brinkmann, H.	Wolter, J.
Franze, M.	Weiss, S.
Weiss, S.	Zesewitz, K.

- Biophysics course of the Dresden-International-Graduate School.

Advisers:

WT 2015/16 & WT 2016/17
Prof. Dr. Fahmy, K.
Dr. Oertel, J.
Philipp, J.

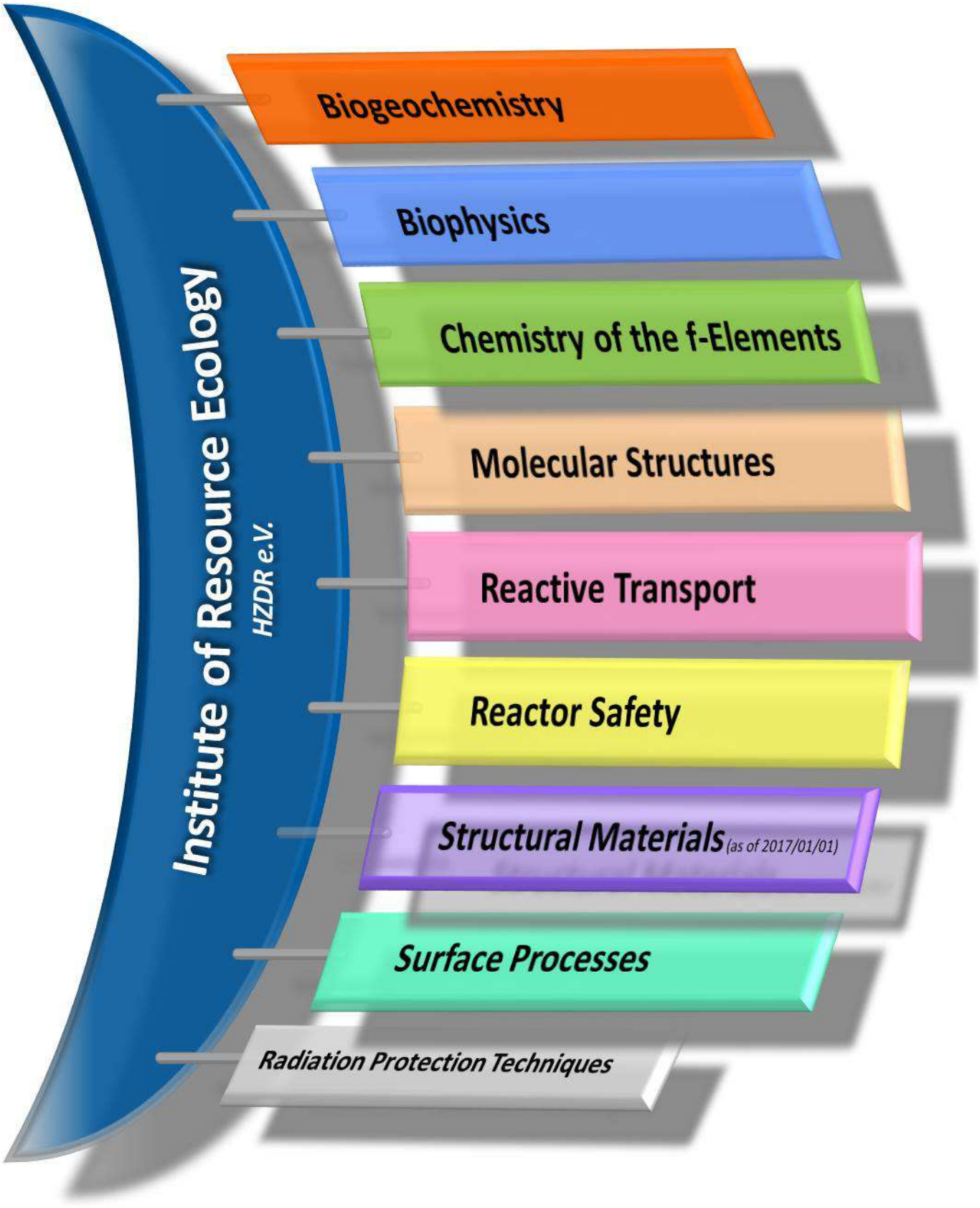
Institute of Resource Ecology
HZDR e.V.
Biogeochemistry
Biophysics
Chemistry of the f-Elements
Molecular Structures
Reactive Transport
Reactor Safety
Structural Materials (as of 2017/01/01)
Surface Processes
Radiation Protection Techniques

Prof. Dr. Thorsten Stumpf
(HEAD OF INSTITUTE)

ADMINISTRATION:
Office Dresden: Gorzitze, Jana; Kovacs, Jenny; Kurde, Kerstin; Lauke, Regina
Office ESRF: Glückert, Marion
Office Leipzig: Gerstner, Katrin
Sysads: Berndt, Ronny (IT), Dr. Steudtner, Robin (Laser Systems)

PROJECT COORDINATION:
Office Dresden: Dr. Arnold, Thuro

RADIATION PROTECTION:
Heim, Heidemarie; Falkenberg, Dirk; Henke, Steffen; Nebe, Katrin; Rumpel, Annette

*: PhD student; as of 2016/12/31

BIOGEOCHEMISTRY
Dr. Geipel, Gerhard

Brinkmann, Hannes*
Dudek, Monika
Flemming, Katrin
Gerber, Ulrike*
Dr. Günther, Alix
Heller, Sylvia
Dr. Krawczyk-Bärsch, Evelyn
Dr. Moll, Henry
Müller, Manuela
Dr. Raff, Johannes
Dr. Sachs, Susanne
Seibt, Jana
Dr. Vogel, Manja
Wollenberg, Anne*

HZDR Young Investigator Group
Dr. Cherkouk, Andrea
Bader, Miriam*
Franze, Madlen*
Kluge, Sindy
Dr. Matschiavelli, Nicole

BIOPHYSICS
Prof. Dr. Fahmy, Karim

Iric, Katarina* (HZDR/TUD)
Dr. Oertel, Jana
Philipp, Jenny
Dr. Tsushima, Satoru

CHEMISTRY OF THE F-ELEMENTS
Dr. Ikeda-Ohno, Atsushi

Dr. Barkleit, Astrid
Dr. Kaden, Peter
Dr. März, Juliane
Dr. Patzschke, Michael
Radoske, Thomas*
Schöne, Sebastian*
Wilke, Claudia*

MOLECULAR STRUCTURES
Dr. habil. Scheinost, Andreas C.

Dr. Baumann, Nils
Exner, Jörg
Dr. Hennig, Christoph
Dr. Kvashnina, Kristina O.
Dr. Lozano Rodriguez, Janeth
Dr. Rossberg, André

REACTIVE TRANSPORT
Dr. Lippmann-Pipke, Johanna

Barthen, Robert*
Becker, Michael*
Dr. Franke, Karsten
Gründig, Marion
Gruhne, Stefan
Dr. Hildebrand, Heike
Dr. Karimzadeh, Lotfallah
Dr. Kulenkampff, Johannes
Dr. Lippold, Holger
Lösel, Dagmar
Dr. Mansel, Alexander
Poetsch, Maria*
Schößler, Claudia
Dr. Schymura, Stefan

REACTOR SAFETY
Dr. Kliem, Sören / Dr. Wilhelm, Polina

Dr. Baier, Silvio
Dr. Bilodid, Yurii
Dr. Fridman, Emil
Gommlich, André
Dr. Grahn, Alexander
Hoffmann, Alexander*
Jobst, Matthias
Konheiser, Jörg
Kozmenkov, Yaroslav
Dr. Müller, Stefan
Nikitin, Evgeny*
Dr. Rachamin, Reuven
Dr. Schäfer, Frank
Sporn, Michael

SURFACE PROCESSES
Dr. Brendler, Vinzenz / Dr. Müller, Katharina

Bauer, Anne*
Dr. Bok, Frank
Eckardt, Carola
Eibl, Manuel*
Fischer, Sarah*
Dr. Foerstendorf, Harald
Dr. Franzen, Carola
Dr. Großmann, Kay
Gürtler, Sylvia
Gurlit, Sabrina
Heim, Karsten
Dr. Huittinen, Nina
Dr. Jordan, Norbert
Lehmann, Susanne*
Müller, Christa
Neubert, Heidrun
Pfützner, Birke
Philipp, Thimo*
Dr. Richter, Anke
Ritter, Aline
Dr. Schmeide, Katja
Shams Aladin Azzam, Salim
Dr. Stockmann, Madlen
Weiss, Stephan
Wolter, Jan-Martin*

HGF Young Investigator Group
Dr. Schmidt, Moritz
Hellebrandt, Sophia*
Hellebrandt, Stefan*
Dr. Qiu, Canrong
Dr. Xiao, Bin
Zesewitz, Konrad*

GUEST SCIENTISTS

Baglio, Jennifer	*North Carolina State University, Raleigh, USA*
Bilodid, Ievgen	*Scientific-technical Centre for Nuclear and Radiation Safety of the Ukraine, Kiew, Ukraine*
Brulfert, Florian	*Université Paris Sud, Institut de Physique Nucléaire, Orsay, France*
Fresneda, Miguel Angel Ruiz	*Departamento de Microbiología, Facultad de Ciencias, Universidad de Granada, Granada, Spain*
Fricke, Thomas	*Vita 34 AG, Leipzig, Germany*
Gallois, Nicolas	*CEA Caderache, St Paul lez Durance, France*
Goguen, Jared	*McMaster University, Hamilton, Canada*
Jivkov, Andrey	*The University of Manchester, Manchester, U. K.*
Kuippers, Gina	*The University of Manchester, Manchester, U. K.*
Magin, Alice	*Karlsruhe Institute of Technology, Karlsruhe, Germany*
Martyanov, Dmitry	*Joint Institute for Power and Nuclear Research Sosny (Belarus) Minsk, Belarus*
Merk, Bruno	*National Nuclear Laboratory and Royal Academy of Engineering, University of Liverpool, Liverpool, U.K.*
Munoz, Andres	*Gesellschaft für Anlagen- und Reaktorsicherheit (GRS) gGmbH, Braunschweig, Germany*
Ovdiienko, Iurii	*Scientific-technical Centre for Nuclear and Radiation Safety of the Ukraine, Kiew, Ukraine*
Rudziankou, Ivanton	*Joint Institute for Power and Nuclear Research Sosny (Belarus) Minsk, Belarus*
Speransky, Philip	*Department für Nukleare Sicherheit und Strahlenschutz des Ministeriums für Notfallsituationen Minsk, Belarus*
Usheva, Krystsina	*Research Institute für Nuclear Problems of Belarusian State University, Minsk, Belarus*
Wu, Hsingtzu	*Japan Atomic Energy Agency, Japan*
Wu, Shijun	*Guangzhou Institute of Geochemistry, Chinese Academy of Sciences, Guangzhou, China*
Virtanen, Sinikka	*Laboratory of radiochemistry, University of Helsinki, Helsinki, Finland*
Zedek, Lukas	*Institute of Mechatronics and Computer Engineering, Technical University of Liberec, Liberec, Czechia*

MASTER/DIPLOMA/BACHELOR

Balakrinshnan, Ashwin	Lösch, Henry	Ritter, Eva	Subramanian, Madhumalar
Haubitz, Toni	Neumann, Julia	Schernikau, Martin	Wendisch, Marc
Knöppel, Julius	Nucke, Lisa	Steglich, Jennifer	

GRADUATE ASSISTANTS, STUDENT ASSISTANTS, TRAINEES

Blumberg, Markus	Junghans, Hannes	Schäfer, Sebastian	Zechel, Susanne
Carstensen, Lale	Leue, Claudia	Sgarzi, Massimo	Zimmermann, Thomas
Fankhänel, Tobias	Reder, Christian	Wolke, Florian	Zimmermann, Veit

ACKNOWLEDGEMENTS

The Institute of Resource Ecology is one of the eight institutes of the Helmholtz-Zentrum Dresden – Rossendorf e.V. (HZDR). As registered, non-profit institution, the HZDR is supported by the authorities of the Federal Government and the Free State of Saxony. In addition to the basic funding, the financial support of the projects listed below by the given organizations and companies is greatfully acknowledged.

FUNDING ORGANIZATION / COMPANY	**PROJECT TITLE**	**CONTRACT NO. (if applicable)**
Commission of the European Communities (EU)	BioMOre – An Alternative Mining Concept - Raw Materials Commitment	*H2020-642456*
	Cebama – Cement-based materials, properties, evolution, barrier functions	*H2020-662147*
	CONCERT – European Joint Programme for the Integration of Radiation Protection Research	*H2020-662287*
	FREYA – Fast Reactor Experiments for hYbrid Applications	*FP7-2696665*
	IVMR – In-Vessel Melt Retention Severe Accident Management Strategy for Existing and Future NPPs	*H2020-662157*
	MIND – Microbiology in Nuclear Waste Disposal	*H2020-661880*
	NetFlot	*KIC RM 15062*
Bundesministerium für Wirtschaft und Energie (BMWi) & Bundesministerium für Bildung und Forschung (BMBF)	BioNEWS – Wachstumskern BioSAM – Verbundprojekt 03 BioNEWS; TP 3.7: Langzeitstabile Zellen zum Aufbau und zur Regenerierung von Sensor- und Aktorsystemen für den Nachweis und die Bindung strategisch relevanter Metalle (insbesondere Seltene Erden)	*03WKCL03F*
	BioVeStRa Untersuchungen des Potentials biologischer Verfahren zur Strahlenschutzvorsorge bei Radionuklidbelastungen	*02S9276A*
	Conditioning – Grundlegende Untersuchungen zur Immobilisierung langlebiger Radionuklide mittels Einbau in endlagerrelevante Keramiken	*02NUK021B* *02NUK021C*
	ECOMETALS – Innovative umweltschonende Prozesse für die Gewinnung strategischer und seltener Metalle aus primären und sekundären Ressourcen; TP HZDR: Rohstoffcharakterisierung, mikrobiologische Mobilisierung von Metallen	*033RF001A*
	EDUKEM – Entwicklung und Durchführung experimenteller Methoden zur verbesserten Modellierbarkeit uranhaltiger salinarer Lösungen	*02E11334B*
	FENABIUM – Struktur-Wirkungsbeziehungen zwischen f-Elementen und organischen Ligandsystemen mit Naturstoff-basierten Bindungsfunktionen in Hinblick auf eine mögliche Mobilisierung in der Umwelt	*02NUK046B*
	GRaZ – Verbundprojekt Geochemische Radionuklidrückhaltung an Zementalterationsphasen	*02E11415B*
	NanoSuppe	*03X0144A*
	NuWaMa – Ausbau einer Deutsch-Tschechischen Koopration auf dem Gebiet der Nuklearen Endlagerforschung	*01DS16008*
	r4 – SE-FLECX – Selektive Flüssig-Flüssig-Extraktion von Lanthaniden & Actiniden durch präorganisierte Calixarene	*033R132A*
	r4 – SEM^2 – Seltene-Erden-Metallurgie – fortgeschrittene Me-thoden für die optimierte Gewinnung und Aufbereitung am Beispiel von Ionenadsorptionstonen	*033R127D*
	ThermAc – Verbundprojekt Aufklärung von Thermodynamik und Speziation von Actiniden bei höheren Temperaturen in Kombination von Schätzmethoden, spektroskopischen und quantenmechanischen Methoden, Teilprojekt B	*02NUK039B*

FUNDING ORGANIZATION / COMPANY	PROJECT TITLE	CONTRACT NO. (if applicable)
	TransAqua – Verbundprojekt Transfer von Radionukliden in aquatischen Ökosystemen Teil A: Untersuchungen zu den Wechselwirkungen zwischen unter Tage lebenden Mikroorganismen mit Uran Teil B: Spektroskopische Bestimmung der Bindungsform (Speziation) trivalenter Actinide/Lanthanide in Biofluiden des menschlichen Gastrointestinaltraktes und im Blut	*02NUK030F*
	UMB – Verbundprojekt Umwandlungsmechanismen in Bentonitbarrieren, Teilprojekt B	*02E11344B*
	WASA-BOSS – Verbundprojekt: Weiterentwicklung und Anwendung von Severe Accident Codes - Bewertung und Optimierung von Störfallmaßnahmen	*02NUK028B*
	WEIMAR – Weiterentwicklung des Smart K_d-Konzepts für Langzeitsicherheitsanalysen	*02 E 11072B*
	WTZ Russland – Transientenanalysen für schnelle Reaktoren	*1501462*
Gesellschaft für Anlagen- und Reaktorsicherheit gGmbH (GRS)	Diffusionsexperimente	
	DYN3D Codetraining	
	THEREDA III	
Helmholtz-Gemeinschaft Deutscher Forschungszentren e.V. (HGF)	HGF-Nachwuchsgruppe Dr. Schmidt	*VH-NG-942*
	Flüchtlingsinitiative	*SO-FI-0004*
AREVA	Experimente PKL3	
PreussenElektra GmbH (bis 01.07.2016 : E.ON Kernkraft GmbH)	Datensatzerstellung für DWR-Anlagen	
	Potenzialstudie Nuklidabsorbierende Pilze	*6021141113*
	Lokale Leistungsänderung	
	MCNP Schieflast	
	MCNP Leistungsverteilung	
	Nachkühlkettenberechnung	
SCK CEN	Mont Terri BN-Experimente 2016	*62 2114 22 35*
TÜV NORD	Prüfung geologischer Fragen	*M.ASS.06.015.01.F70*
TÜV SÜD	Datenbibliotheken für WWER-1000-Reaktoren	*3611R01504*
UJV Rez, a.s.	DYN3D für UJV Wartung 2015/2016	
	DYN3D für UJV Wartung 2016/2017	

INDEX OF AUTHORS

HZDR

HELMHOLTZ
ZENTRUM DRESDEN
ROSSENDORF

Institute of Resource Ecology
P.O. Box 51 01 19 · 01314 Dresden/Germany
Phone +49 351 260-3210
Fax +49 351 260-3553
Email contact.resourceecology@hzdr.de
http://www.hzdr.de

Member of the Helmholtz Association